Design and 3D printing of compliant mechanisms
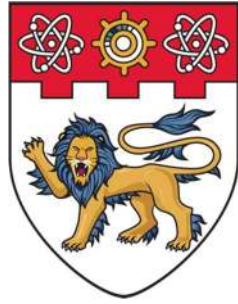
Pham, Minh Tuan

2019

DESIGN AND 3D PRINTING OF COMPLIANT MECHANISMS

PHAM MINH TUAN

SCHOOL OF MECHANICAL & AEROSPACE ENGINEERING

A thesis submitted to Nanyang Technological University in fulfillment of the

requirement for the degree of Doctor of Philosophy

January 2019

Statement of Originality

I hereby certify that the work embodied in this thesis is the result of original research, is free of plagiarised materials, and has not been submitted for a higher degree to any other University or Institution.

23 January 2019
        Date

                                           Pham Minh Tuan

Supervisor Declaration Statement

I have reviewed the content and presentation style of this thesis and declare it is free of plagiarism and of sufficient grammatical clarity to be examined. To the best of my knowledge, the research and writing are those of the candidate except as acknowledged in the Author Attribution Statement. I confirm that the investigations were conducted in accord with the ethics policies and integrity standards of Nanyang Technological University and that the research data are presented honestly and without prejudice.

23 January 2019

Date

Yeo Song Huat

Authorship Attribution Statement

This thesis contains material from 2 papers published in the following peer-reviewed journals where I was the first author.

Chapter 3 is published as M. T. Pham, T. J. Teo, and S. H. Yeo, "Synthesis of multiple degrees-of-freedom spatial-motion compliant parallel mechanisms with desired stiffness and dynamics characteristics," *Precision Engineering*, vol. 47, pp. 131-139, 2017. DOI: http://dx.doi.org/10.1016/j.precisioneng.2016.07.014

The contributions of the co-authors are as follows:

- Prof Yeo suggested the initial project direction.
- I prepared the manuscript drafts. The manuscript was revised by Dr. Teo and Prof Yeo.
- I co-designed the study with Dr. Teo and performed all the laboratory work at the School of Mechanical and Aerospace Engineering and the Singapore Institute of Manufacturing Technology. I also analyzed the data.

Chapter 4 is published as M. T. Pham, T. J. Teo, S. H. Yeo, P. Wang, and M. L. S. Nai, "A 3D-printed Ti-6Al-4V 3-DOF compliant parallel mechanism for high precision manipulation," *IEEE/ASME Transactions on Mechatronics*, vol. 22, no. 5, pp. 2359-2368, 2017. DOI: 10.1109/TMECH.2017.2726692

The contributions of the co-authors are as follows:

- Prof Yeo suggested the initial project direction.

- I prepared the manuscript drafts. The manuscript was revised by Dr. Teo and Prof Yeo.
- The 3D printed prototype was built by Dr. Wang and Dr. Nai at the Singapore Institute of Manufacturing Technology.
- I co-designed the study with Dr. Teo and performed all the laboratory work at the School of Mechanical and Aerospace Engineering and the Singapore Institute of Manufacturing Technology. I also analyzed the data.
- Dr. Wang verified the experimental data on the mechanical properties of thin beams fabricated by Electron Beam Melting method.

23 January 2019

Date

Pham Minh Tuan

Abstract

Compliant mechanism has been a popular solution for developing precise motion systems. This is because the working principle of compliant mechanism is based on elastic deformation of flexure elements, which is capable of providing highly repeatable motions that conventional bearing-based counterparts fail to deliver. In positioning applications, compliant parallel mechanism (CPM) is preferred because its closed-form architecture has high payload allowance and can better reject external mechanical disturbances. However, the performance of CPMs is often constrained by the limitations of synthesis techniques and fabrication methods. At present, it is still a challenge to synthesize multiple degrees-of-freedom (DOF) CPMs with spatial motions, optimized stiffness and dynamic properties. In addition, using conventional machining methods to fabricate the structure of CPMs by sub-parts will incur assembly errors. To address the limitations, this research focuses on the development of a new synthesis method for multi-DOF CPMs and the investigation on the mechanical characteristics of CPMs that are monolithically fabricated by 3D printing technology.

A novel structural optimization method, termed as beam-based structural optimization method, is proposed to synthesize CPMs with multi-DOF, optimized stiffness and desired dynamic properties. A well-defined objective function for the optimization process is also presented where the different units of components within the stiffness matrix of CPMs are normalized. It is shown that the desired motions of CPMs can be obtained by determining specific geometries of the curved-and-twisted beams. The effectiveness of the beam-based method is demonstrated by synthesizing a 3-DOF spatial-motion ($\theta_X - \theta_Y - Z$) CPM with high stiffness ratios of more than 200 for the rotations and 4000 for the translations, a large workspace of 8° × 8° × 5.5 mm and a targeted dynamic response of 100 Hz. A monolithic prototype of the synthesized CPM is fabricated by electron beam melting (EBM) technology and the characteristics of the 3D-printed CPM are experimentally investigated. By introducing a coefficient factor to compensate the difference between the designed thickness and effective thickness, the mechanical properties of 3D-printed CPMs can be well predicted. Experimental results show that EBM technology can be used to fabricate compliant devices for high-precision positioning systems.

CPMs with motion-decoupling capability are desirable to eliminate parasitic motions. Several design criteria are analytically derived for synthesizing 3-legged CPMs with any DOF and fully-decoupled motions. A design of 3-DOF ($\theta_X - \theta_Y - Z$) CPM with decoupled output motions is presented and experimentally evaluated. To demonstrate the versatility of the beam-based method and the decoupled-motion criteria, a new CPM with 6-DOF is synthesized. Its end effector is built by cellular structure to exploit the benefit of 3D printing technology. Experimental investigations show that the EBM-printed prototype of the 6-DOF CPM has motion-decoupling capability and is able to produce a large workspace of more than 6 mm for the translations and 12° the for the rotations. It is envisaged that results of this research can help engineers to develop a variety of high-precision machines with optimal performances.

Acknowledgment

First, I would like to express my deeply gratitude to my main supervisor, Professor Yeo Song Huat, from the School of Mechanical and Aerospace Engineering (MAE), Nanyang Technological University (NTU). From the very first day of my PhD study, he always shows his kindness and enthusiasm to help me in my life and support me in research.

Second, I am deeply grateful to my co-supervisor, Dr. Daniel Teo Tat Joo, from A*STAR. He is willing to help me with any issue, and always shares his academic and practical knowledge to help me in developing the theoretical approaches as well as conducting experiments.

I would like to express my special thanks to my Thesis Advisory Committee, and also acknowledge the ASEAN University Network/Southeast Asia Engineering Education Development Network (AUN/SEED-Net) and the Singapore Centre for 3D Printing (SC3DP) for giving me the opportunity to pursue PhD study.

I sincerely thank Dr. Wang Pan and Dr. Nai Mui Ling Sharon from Singapore Institute of Manufacturing Technology (SIMTech) for their support in 3D printing. I want to express my special thanks to Dr. Wang Pan, who always gives me helpful advises on fabrication issues. I would like to thank Dr. Zhu Haiyue from SIMTech for helping me to setup the experiments and my senior, Dr. Lum Guo Zhan, for sharing his valuable experience on this research topic. I also want to extend my appreciation to the staff from Robotics Research Centre (RRC), Mr. Lim Eng Cheng, Ms. Agnes Tan Siok Kuan and Mr. You Kim San, for their kindness.

Finally, I would like to thank all my family and especially my wife, for the continuous support and encouragement that they have given to me during the time I have been studying at NTU.

Contents

List of Figures

List of Tables

List of Abbreviations

3L-CPM	3-Legged Compliant Parallel Mechanism
BESO	Bi-directional Evolutionary Structural Optimization
CNC	Computer Numerical Control
CPM	Compliant Parallel Mechanism
C-T	Curved and Twisted
DOF	Degrees of Freedom
EBM	Electron Beam Melting
EDM	Electrical Discharge Machining
ESO	Evolutionary Structural Optimization
F/T	Force/Torque
FACT	Freedom and Constraint Topology
FEA	Finite Element Analysis
GA	Genetic Algorithm
MEMS	Micro-Electro-Mechanical Systems
PPS	Prismatic-Prismatic-Spherical
PRB	Pseudo Rigid Body
PRPR	Prismatic-Revolute-Prismatic-Revolute
PRR	Prismatic-Revolute-Revolute
PSS	Prismatic-Spherical-Spherical
RPS	Revolute-Prismatic-Spherical
RRR	Revolute-Revolute-Revolute
SIMP	Solid Isotropic Microstructure with Penalization
SYM	Symmetric

List of Notations

K^s	Global stiffness matrix of CPM
M^s	Global mass matrix of CPM
P^s	Load vector
U^s	Displacement vector
K^{beam}	Stiffness matrix of a beam element
M^{beam}	Mass matrix of a beam element
F_X	Force along the X axis
F_Y	Force along the Y axis
F_Z	Force about the Z axis
M_X	Moment about the X axis
M_Y	Moment about the Y axis
M_Z	Moment about the Z axis
Δ_X	Translational displacement along the X axis
Δ_Y	Translational displacement along the Y axis
Δ_Z	Translational displacement along the Z axis
θ_X	Rotational displacement about the X axis
θ_Y	Rotational displacement about the Y axis
θ_Z	Rotational displacement about the Z axis
K	General 6×6 stiffness matrix
P	General load vector
U	General displacement vector
D	Set of possible motions
N	Set of desired motions
M	Set of undesired motions
η	The number of desired motions
μ	The number of undesired motions
W	Work done
ω	Bandwidth vector
F	Natural frequency vector
F_1	The first natural frequency
F_d	Desired dynamic response
E	Young's modulus of material
I	Moment of inertia
h	Width of flexure

t	Thickness of flexure
L	Length of flexure
t_d	Desired thickness
t_e	Effective thickness
λ	Coefficient factor
K^m	Stiffness matrix of 3L-CPM
K^l	Stiffness matrix of a compliant leg
C^l	Compliance matrix of a compliant leg
C^{sc}	Compliance matrix of a serial chain
C^e	Compliance matrix of a flexure element
$\bar{C}^e$	Compliance matrix of a transformed flexure element
R	Rotation matrix
J	Translational matrix
α	Rotation angle about X'' axis
β	Rotation angle about Y'' axis
γ	Rotation angle about Z'' axis
M	Reflection matrix
J_Δ	Offset matrix for Δ distance

CHAPTER 1

INTRODUCTION

1.1 Background and Motivation

Compliant mechanism has been a popular solution for developing high-precision motion systems because it is able to provide repeatable motions that traditional bearing-based counterparts failed to deliver. The high repeatability can be obtained since the working principle of compliant mechanisms is based on elastic deformation of flexure elements that offers many advantages such as zero backlash, maintenance-free, frictionless, and no wear and tear [1]. Compliant mechanism can be classified into two types, i.e., serial and parallel designs. While the large work range of serial compliant mechanism is employed to create many devices in the field of soft robotics [2-4], compliant parallel mechanism (CPM) is preferred in positioning systems because its closed-loop parallel architecture offers the insensitivity to external mechanical disturbances, high payload and high non-actuating stiffness. CPMs have been widely used in various applications providing precise motions ranging from nanometers to centimeters, such as microgrippers [5-7], actuators [8-11], manipulators [12-15] and alignment systems [16-18]. Among them, positioning stages developed based on CPMs can be considered as one of the most important devices in many industrial fields [19-32]. The literatures over the past two decades demonstrate that the development of CPMs is governed by design methodology and fabrication technology.

For any CPM-based motion system, desired output motions which determined by the degrees-of-freedom (DOF) are always the main objective in the design process. In general,

DOF can be defined based on stiffness property of CPM, i.e., the desired motions are obtained by the low stiffness in actuating directions while the other stiffness in non-actuating directions needs to be high to constrain the unwanted motions. To satisfy those requirements, the ratio between non-actuating and actuating stiffness is proposed as a standard in synthesizing CPMs. The stiffness ratio is targeted as high as possible to ensure CPMs can easily generate desired motions and resist against external mechanical disturbances in non-actuating directions. Apart from achieving the desired DOF, the fast dynamic response is another important demand of advanced motion systems. However, CPMs with low actuating stiffness and large workspace often perform poor dynamic behavior. Therefore, a design methodology that can govern large workspace, high stiffness ratio and fast dynamic response for CPMs is necessary.

As CPM becomes an essential component in many industrial fields, design methodologies have been a focus of development in order to synthesize CPMs with various DOF for different applications. Typically, CPM can be synthesized by three main approaches: rigid body replacement, constraint-based and optimization approaches. The rigid body replacement (also known as task-oriented) approach, which synthesis process is shown in Figure 1.1, can be considered as the traditional design methodology for synthesizing CPMs. It utilizes architectures of conventional rigid-mechanisms as the skeletons and CPMs can be obtained by replacing the rigid joints by corresponding compliant joints while the rigid links are remained. Desired motions of CPMs can be easily defined by using traditional kinematics analysis. The finite element analysis (FEA) can then be carried out to optimize shape/size of the design, evaluate the stress distribution within the structure and determine the workspace.
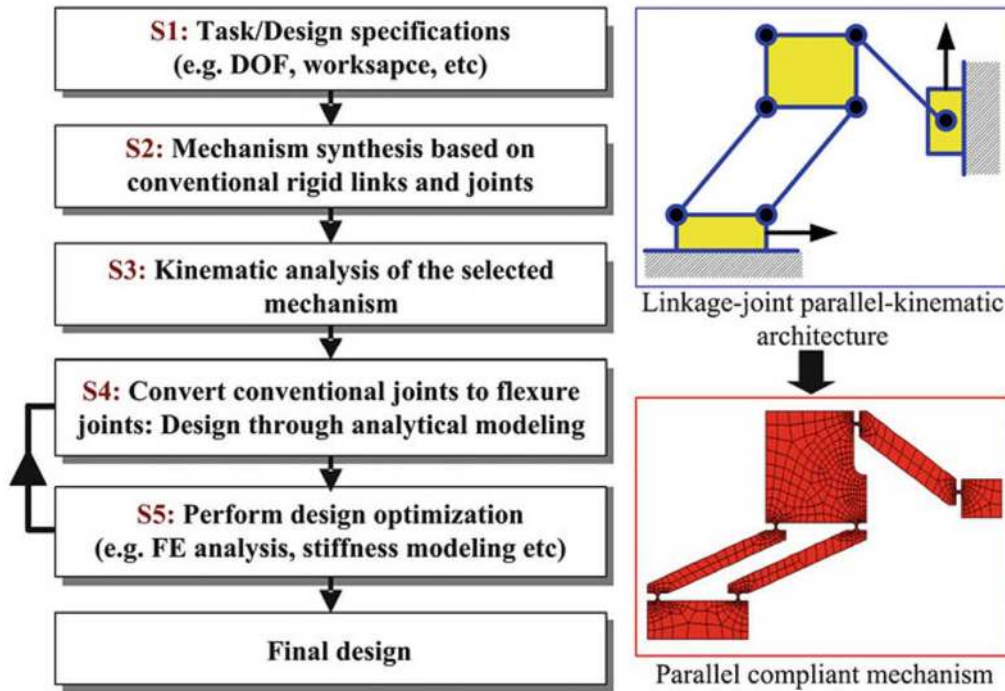
Figure 1.1: Flow of rigid body replacement approach [33].

Benefit of the rigid body replacement approach is the convenience in synthesizing desired DOF by employing existing designs of conventional rigid-mechanisms, and the simple actuation by analyzing the kinematics of the moving platform depending on input motions of active joints. Thus, a vast number of CPMs, vary from common designs of 1-DOF [7, 34, 35], 2-DOF [15, 31, 36-39], 3-DOF [17, 40-46] CPMs to complex designs of 5-DOF [47] and 6-DOF CPMs [48, 49], have been developed using the rigid body replacement approach. However, this approach also has many drawbacks such as the difficulty in optimizing dynamic behavior and the dependence on intuition of designers.

For the constraint-based approach, CPMs is synthesized based on the constraint space determined by the desired DOF. Suitable flexure elements will be selected and allocated at defined positions to constrain output motions of CPMs. The general fundamentals for adding constraints to a moving body in order to obtained targeted motions are illustrated in Figure 1.2.

	3T	2T	1T		0T
3R					
2R					
1R					
0R					

←— Translation axis   •—• Constrain   +—→ Rotation axis
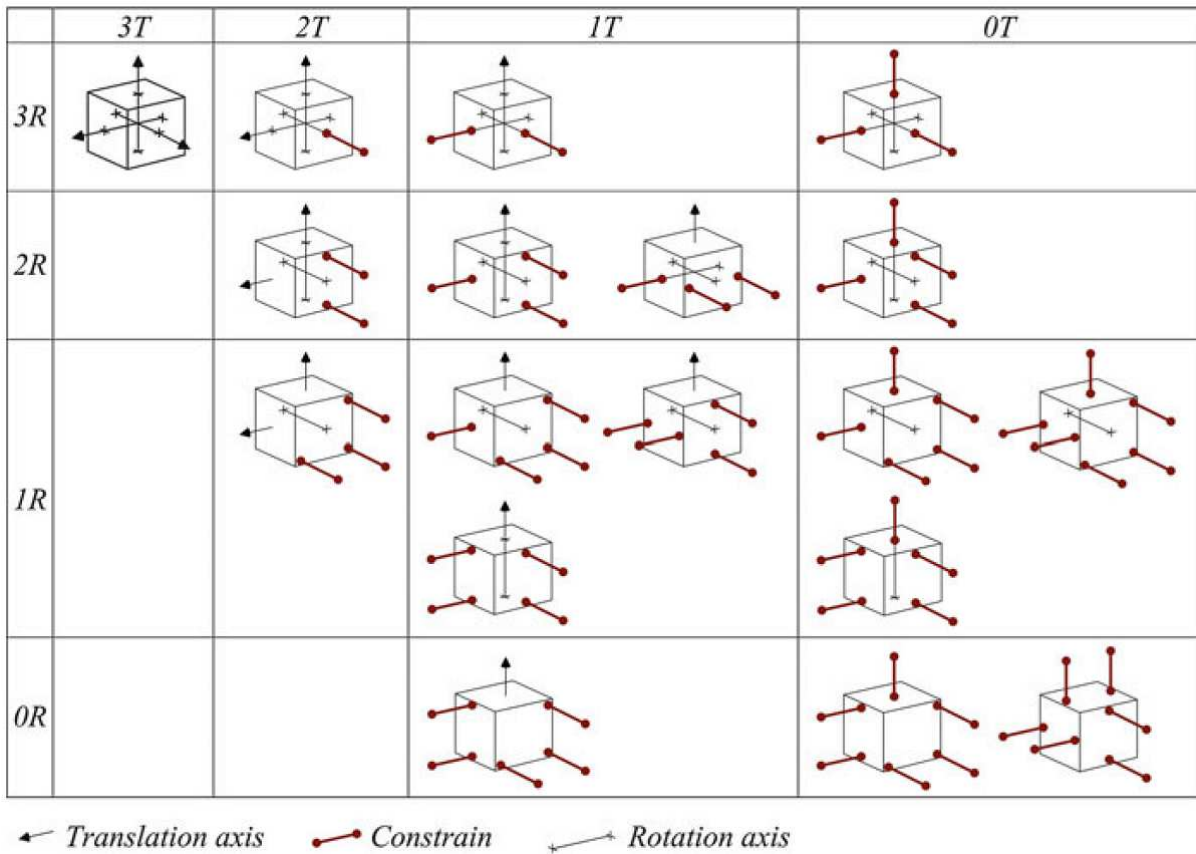
Figure 1.2: Fundamentals of constraint-based approach [33].

As compliant constraints and kinematics property can be quickly defined, various CPMs have been synthesized by the constraint-based approach [12, 50-54]. Even though existing architectures of conventional mechanisms are unnecessary in this approach, it is still dependent on human intuition since flexure elements are selected by designers. Moreover, resulting CPMs are not optimized since they are constructed by pre-defined flexures.

In contrast to the rigid body replacement and constraint-based approaches, the optimization approach is developed based on FEA and optimization techniques to find the optimal structure/topology of CPMs. The optimal design of CPM can be achieved if result of the objective (fitness) function satisfies defined criteria and additional constraints. The synthesis process of optimization approach is illustrated in Figure 1.3. First, the desired specifications and the boundary constraints must be specified for modeling the design domain.

The design domain will then be meshed by continuum or discrete elements. The optimal design

is achieved by repeating calculation process until result of the objective function converges.
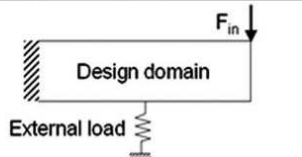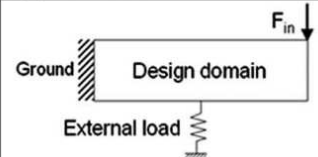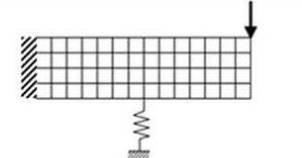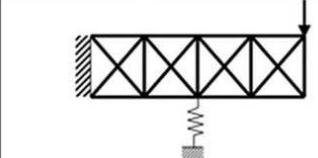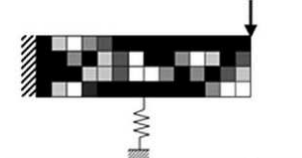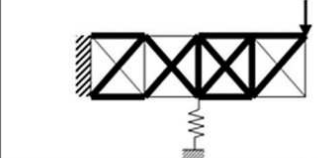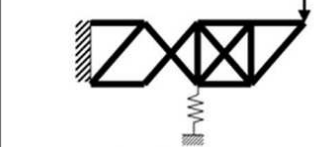
Typical Synthesis Procedure	(a) Continuum structure	(b) Discrete structure
Step 1: Problem Specification - Define design domain - Apply boundary conditions		
Step 2: Design Domain Parameterization - Discretize design domain - Define design variables		
Step 3: Topology Optimization - Define objective function - Choose and implement optimization method		
Step 4: Final Design Interpretation - Filter out elements with values under certain threshold - Interpret final topology		

Figure 1.3: Synthesis process of optimization approach [55].

The optimization approach overcomes drawbacks of the other two approaches since the

human-intuition dependence is eliminated. The design of CPM can be easily customized by

changing the objective function and additional constraints. In addition, the optimization

approach is able to synthesize the dynamic behavior of CPMs based on the merits of FEA. As

a result, various design methods have been developed based on optimization approach and

applied to synthesize numerous CPMs [14, 55-75]. Nevertheless, the number of multi-DOF

CPMs synthesized by this approach is limited due to the objective function. In particular, the

most popular objective functions have been used to synthesize compliant mechanisms are

based on the mutual potential energy that only considers the relative relation of energies

between input and output positions [1, 76]. Thus, almost developed CPMs have 1-DOF and are

applied to create grippers, force/motion amplifiers/inverters. Recently, a new objective

function has been proposed to synthesize multi-DOF CPMs [74], but its unit is not well defined because of the difference in the units (N/m or Nm/rad) of the components within the stiffness matrix.

In summary, all synthesis approaches perform their corresponding advantages and disadvantages. The multi-DOF CPMs can be easily synthesized by the rigid body replacement and constraint-based approaches but the designs are dependent on human intuitions; and the mechanical properties, especially the dynamic behavior, are difficult to optimized during the synthesis process. On the other hand, the optimization approach employs the numerical method that eliminates the dependence of intuition and can optimize both the stiffness and dynamic characteristics of CPMs. However, the synthesis of multi-DOF CPMs is constrained due to the limitations of existing objective functions. It is a major challenge to synthesize multi-DOF CPMs with the stiffness and dynamic characteristics being governed in the design process by well-defined objective functions.

To improve the performance of compliant positioning systems, the motion property of CPMs is highly important since it directly determines the positioning accuracy. As CPM operates based on elastic deformation, some unwanted parasitic motions could be generated when the flexures deform and reduce the accuracy of desired output motions. Hence, decoupled-motion characteristic is one of the main objectives to design CPMs for positioning systems. Nevertheless, the coupled/decoupled motions of CPMs have not been clearly discussed in the past literatures because most existing designs are synthesized with the aim of achieving desired DOF. Consequently, they are able to deliver the motions in the desired actuating directions but could produce parasitic motions in non-actuating directions. Therefore, the general criteria for designing CPMs with fully-decoupled motions are necessary to develop precise motion systems. If the design criteria are integrated into the synthesis process, obtained

CPMs can produce predictable motion property as well as optimized mechanical characteristics.

Apart from the design methodology, fabrication technology is one of the key factors that affect the performance of CPMs. As CPMs could be created by the combination of various flexures in different orientations [77], the fabrication process must provide abilities to fabricate thin features and complex structures. At present, milling and wire-cut electrical discharge machining (EDM) are the popular solutions for manufacturing CPMs. However, the accuracy of thin flexures fabricated by milling technology is low due to the cutting forces while the wire-cut EDM technology is only applicable to metallic-planar structures. In order to obtain the complex structures using such cutting methods, CPMs must be separated into many parts for fabrication and the assembly process is needed as the last step to create complete prototypes. As a result, the performance of CPMs could be affected by unpredictable assembly errors.

Nowadays, 3D printing (additive manufacturing) technology can be considered as a potential solution for building monolithic complex structures to eliminate assembly errors. Among various 3D printing methods, electron beam melting (EBM) is a popular method that can fabricate functional complex products with nearly-full density [78]. Several compliant joints and mechanisms with complex designs have been built by EBM method [79-81]. An example of 3D-printed flexure hinge having large elastic rotation of up to 90° is shown in Figure 1.4. Nevertheless, the number of 3D-printed CPMs for precision systems is still very limited and the mechanical characteristics of 3D-printed flexures have not been investigated.
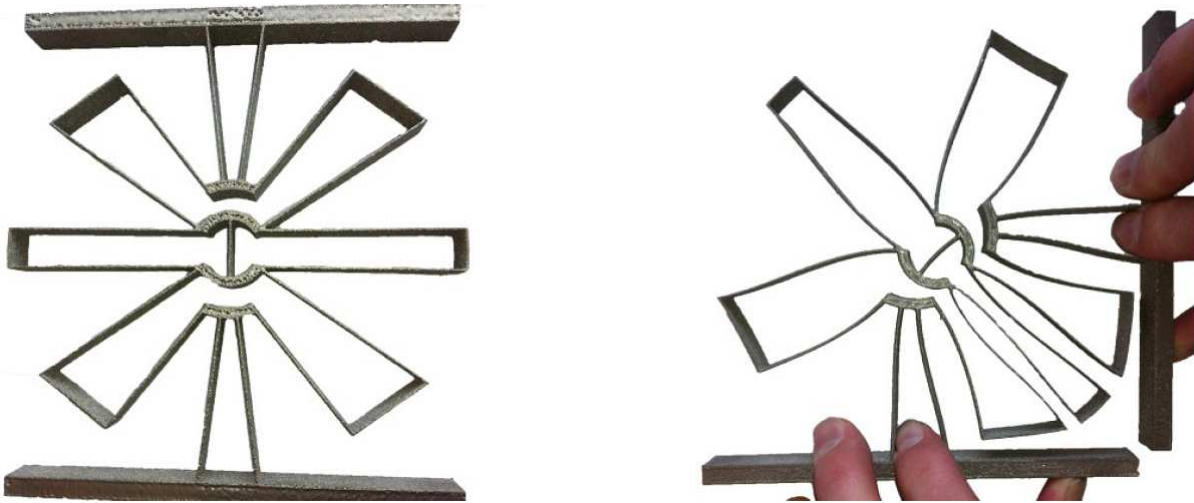
Figure 1.4: A flexure hinge with large elastic deformation fabricated by EBM method [80].

1.2 Objectives and Scope

The main objectives of the research are to develop a design methodology for CPMs with multi-DOF, to derive the fundamental criteria for synthesizing CPMs with fully-decoupled motions, and to investigate the mechanical characteristics of 3D-printed CPMs built by EBM technique.

To achieve the objectives, the scope of work includes:

- Proposing a novel synthesis method based on optimization approach for synthesizing CPMs. The proposed method must overcome the limitations of the existing structural/topological optimization methods. In particular, the new method should be capable of synthesizing multi-DOF CPMs for precise positioning applications.

- Deriving a new objective function for the stiffness optimization process. Most of the existing objective functions are used to synthesize CPMs with only 1-DOF for grippers, force/motion inverters, etc. The proposed objective function must be able to synthesize multi-DOF CPMs and its unit should be well defined.

- Integrating both the stiffness and dynamic optimizations into the synthesis process. This will enable the synthesized CPMs to produce desired DOF, possess highest stiffness ratios and achieve targeted dynamic response.

- Synthesizing a novel design of 3-DOF spatial-motion ($\theta_X - \theta_Y - Z$) CPM with optimized stiffness and dynamic properties. The performance of the synthesized CPM will be experimentally evaluated and compared to the predicted values to demonstrate the effectiveness of the proposed synthesis method.

- Employing EBM technique to fabricate the synthesized 3-DOF ($\theta_X - \theta_Y - Z$) CPM. The mechanical characteristic of the prototype will be investigated. A manipulator will be built based on the EBM-printed CPM and its performance will be measured to evaluate whether 3D-printed CPMs can be used in precise motion systems.

- Investigating the design criteria for synthesizing CPMs with fully-decoupled motions. A CPM will be synthesized, and its motions will be evaluated experimentally to validate the proposed design criteria.

- Synthesizing a novel 6-DOF CPM with fully-decoupled motions, optimized stiffness and dynamic properties. A prototype of the CPM will be built by EBM technique and its performance in terms of mechanical characteristics and motion-decoupling capability will be evaluated experimentally.

1.3 Organization of the Thesis

The remaining chapters of the thesis are organized as follows:

Chapter 2 provides the literature review on synthesis methodologies for CPMs, the benefits as well as limitations of each method are described. Existing multi-DOF CPMs are also presented and their performances are discussed. In addition, a review on applications of 3D printing technology in fabricating flexible structures and CPMs will also be included.

Chapter 3 introduces the beam-based structural optimization method used to synthesize CPMs for positioning systems. The modeling of stiffness and dynamic properties of CPMs will be described. The formulation of a new objective function specialized for multi-DOF CPMs with well-defined unit will also be presented. The proposed method is used to synthesize a 3-DOF spatial-motion $(\theta_X - \theta_Y - Z)$ CPM with optimized stiffness property and targeted dynamic response. A prototype of the synthesized CPM is fabricated by the conventional milling method and its performance is experimentally evaluated.

In Chapter 4, the investigation on the mechanical characteristics of a 3D-printed prototype of the synthesized 3-DOF CPM, built by EBM method, is presented. A coefficient factor is proposed to compensate the errors caused by fabricating tolerance and surface roughness of the EBM-printed flexures. In addition, the experimental results on the performance of a 3-DOF manipulator for precise motion system built based on the 3D-printed CPM are discussed.

Chapter 5 presents the derivation of criteria for synthesizing 3-legged CPMs with fully-decoupled motions. The position and orientation of each flexure element are analyzed to demonstrate how they affect the motion property of entire CPM. The proposed criteria will be used to synthesize a 3-DOF $(\theta_X - \theta_Y - Z)$ CPM with decoupled motions as a case study.

Chapter 6 introduces a decoupled-motion 6-DOF CPM synthesized by the beam-based method and the proposed design criteria. The advantages of 3D printing technology are exploited to fabricate the end effector with cellular structure in order to enhance the dynamic

behavior of the CPM. Experiments are carried out to evaluate the mechanical properties and the motion-decoupling capability of the 3D-printed prototype.

Finally, some conclusions of this research and proposed future work will be outlined in Chapter 7.

CHAPTER 2
LITERATURE REVIEW

In this chapter, the existing design methodologies for compliant mechanisms are classified by their principles, and the advantages as well as disadvantages of each synthesis method are outlined. The performances of state-of-the-art multi-DOF CPMs are also discussed. In addition, previous works on 3D-printed compliant mechanisms are presented, and the benefits as well as difficulties of using 3D printing technology to fabricate compliant structures are highlighted.

2.1 Design Methodologies

2.1.1 Rigid body replacement approach

In rigid body replacement approach, the Pseudo-Rigid-Body (PRB) model is used to synthesize compliant mechanisms. PRB model allows flexible structures to be represented as rigid structures. Thus, compliant mechanisms can be created by employing traditional design techniques. An example of compliant mechanism synthesized by this approach is illustrated by Figure 2.1. A rigid-mechanism, which constructed by the combination of rigid links and joints, is used as the design skeleton. The compliant mechanism is created by replacing all traditional joints by the corresponding types of compliant joint where the rigid links are remained.
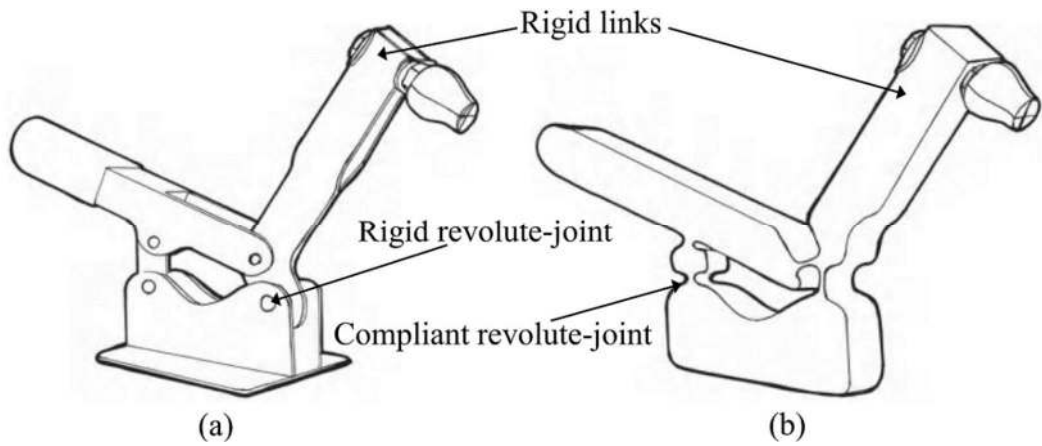
Figure 2.1: (a) Rigid mechanism and (b) compliant mechanism designed by the rigid body replacement approach [1].

Since compliant joint is the key factor in the rigid body replacement approach, various types of compliant joints have been developed to represent the motions of their rigid counterparts [1, 77]. Based on the construction of flexure such as leaf-spring or notch-hinge, compliant joints can be classified into two types, i.e., beam-type and notch-type as shown in Figure 2.2a and Figure 2.2b respectively.
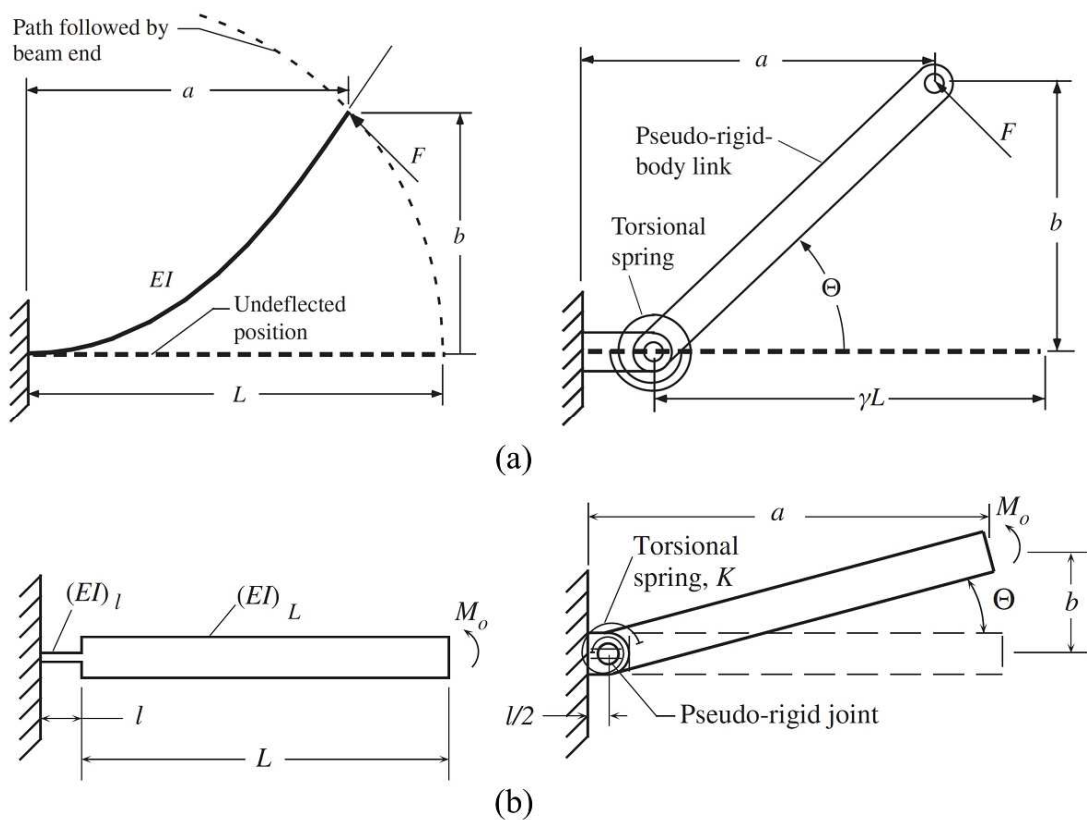
Figure 2.2: PRB models of compliant joint (a) beam-type and (b) notch-type [1].

13

It is seen from Figure 2.2, the beam-type and notch-type compliant joints are created by a long thin-beam and a small pivot respectively. Hence, the beam-type joint is able to produce large deflection along the actuating direction with a small actuating force, and it is also sensitive to the loads in non-actuating directions. On the other hand, the notch-type joint needs larger actuating force to achieve the same deflection as the beam-type joint, but it exhibits high stiffness in non-actuating directions to resist against the external disturbances. As large workspace becomes a common requirement for compliant mechanisms, beam-type joints are preferred. Thus, numerous complex designs of beam-type compliant joints have been developed as shown in Figure 2.3. They are able to produce various motions in different directions and the range of elastic deformation is significantly improved by specific designs of flexures.

(a)	(b)	(c)
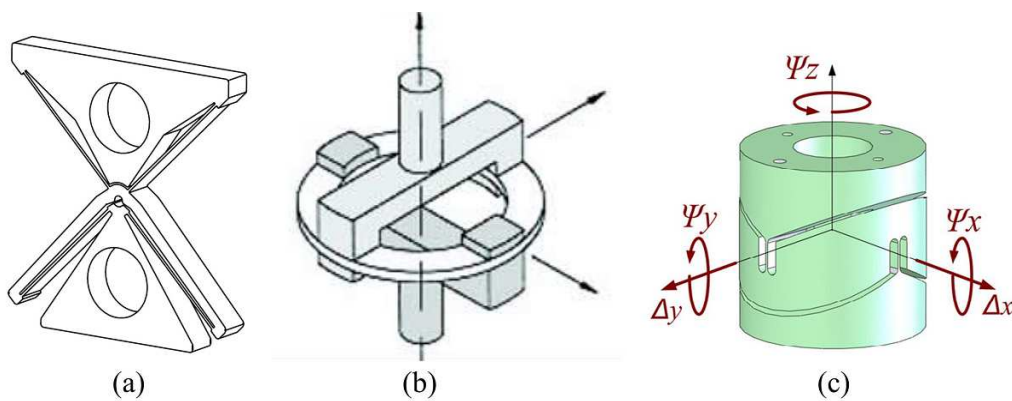
Figure 2.3: Complex beam-type compliant joints (a) revolute joint [82], (b) universal joint [77] and (c) spherical joint [83].

By using various types of compliant joints, many types of CPM have been developed from 1-DOF [7, 34, 35], 2-DOF [15, 31, 36-39], 3-DOF [17, 40-46] to 5-DOF [47] and 6-DOF CPMs [48, 49]. An example of 2-DOF ($X - Y$) CPM synthesized by this approach is shown in Figure 2.4. Due to the simple synthesis process and kinematics analysis, it has become the most popular method for synthesizing compliant mechanisms. However, because the synthesis process is carried out based on a chosen architecture of existing conventional mechanism, the

intuitional dependence can be considered as an important shortcoming of this approach that may lead to non-optimal designs.
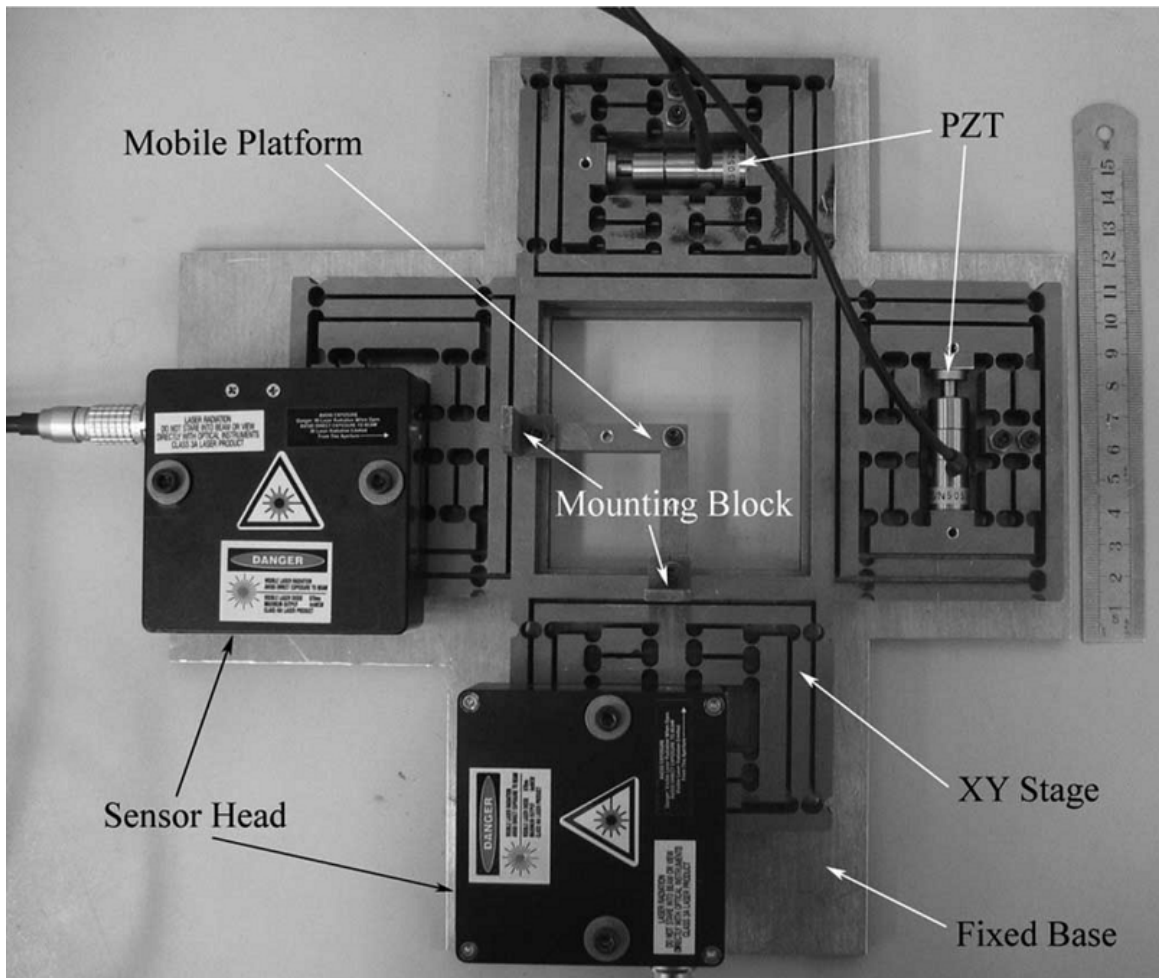
Figure 2.4: A 2-DOF $(X - Y)$ compliant manipulator synthesized by rigid body replacement approach [15].

2.1.2 Constraint-based approach

The constraint-based approach, also known as freedom and constraint topology (FACT) approach [84, 85], offers a systematic framework to create compliant mechanisms by applying the minimal number of flexure constraints. Beside the three regular geometries of flexure elements, i.e., wire, blade and hinge shapes, various flexure elements with irregular shapes have been developed in order to create any DOF for moving rigid bodies. The flexure elements provided by FACT are illustrated in Figure 2.5.
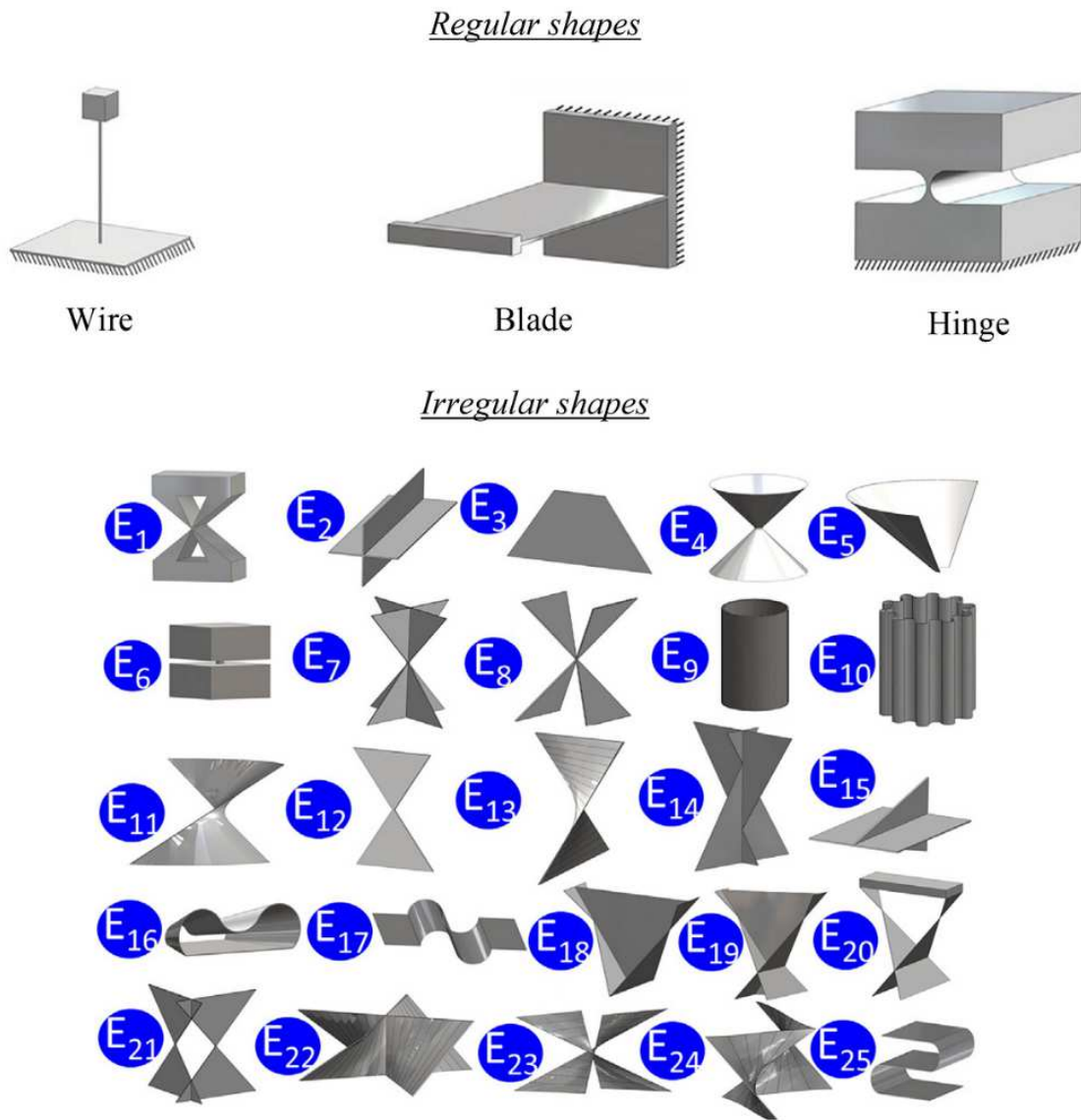
Figure 2.5: Flexure elements provided by FACT [51].

Based on screw theory, a library of freedom- and constraint-space pairs has been generated as shown in Figure 2.6. By using the library and the list of flexure elements, designers can synthesize compliant mechanisms with various desired motions.
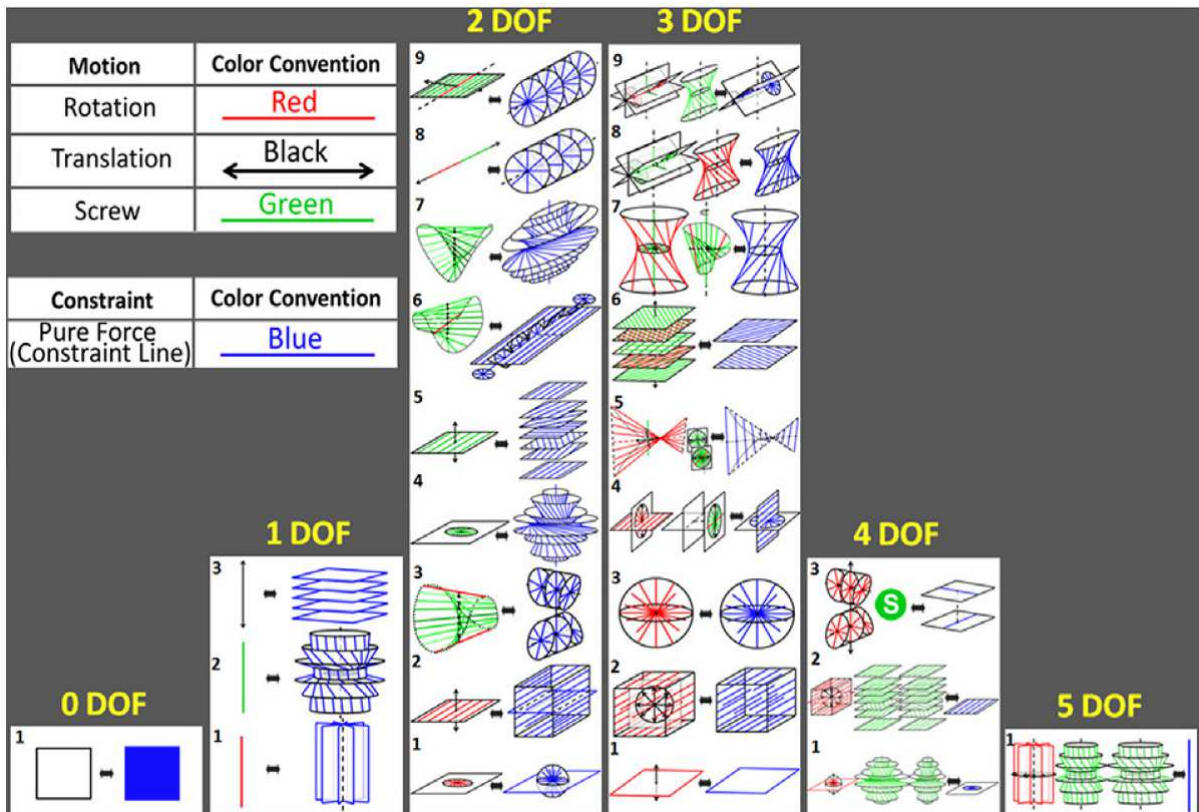
Figure 2.6: FACT library showing the relation between freedom- and constraint-space [51].

The advantage of the constraint-based approach is demonstrated by the simplicity in synthesizing complex multi-DOF CPMs [12, 50-54]. Structure of CPM can be quickly generated by selecting the appropriate model in the library based on the desired DOF, and suitable flexure elements will then be distributed into the positions of constraints. The synthesis process of a 3-DOF ($\theta_X - \theta_Y - \theta_Z$) CPM is illustrated in Figure 2.7 and an example of 3-DOF ($\theta_X - \theta_Y - Z$) compliant manipulator synthesized by this approach is shown in Figure 2.8.
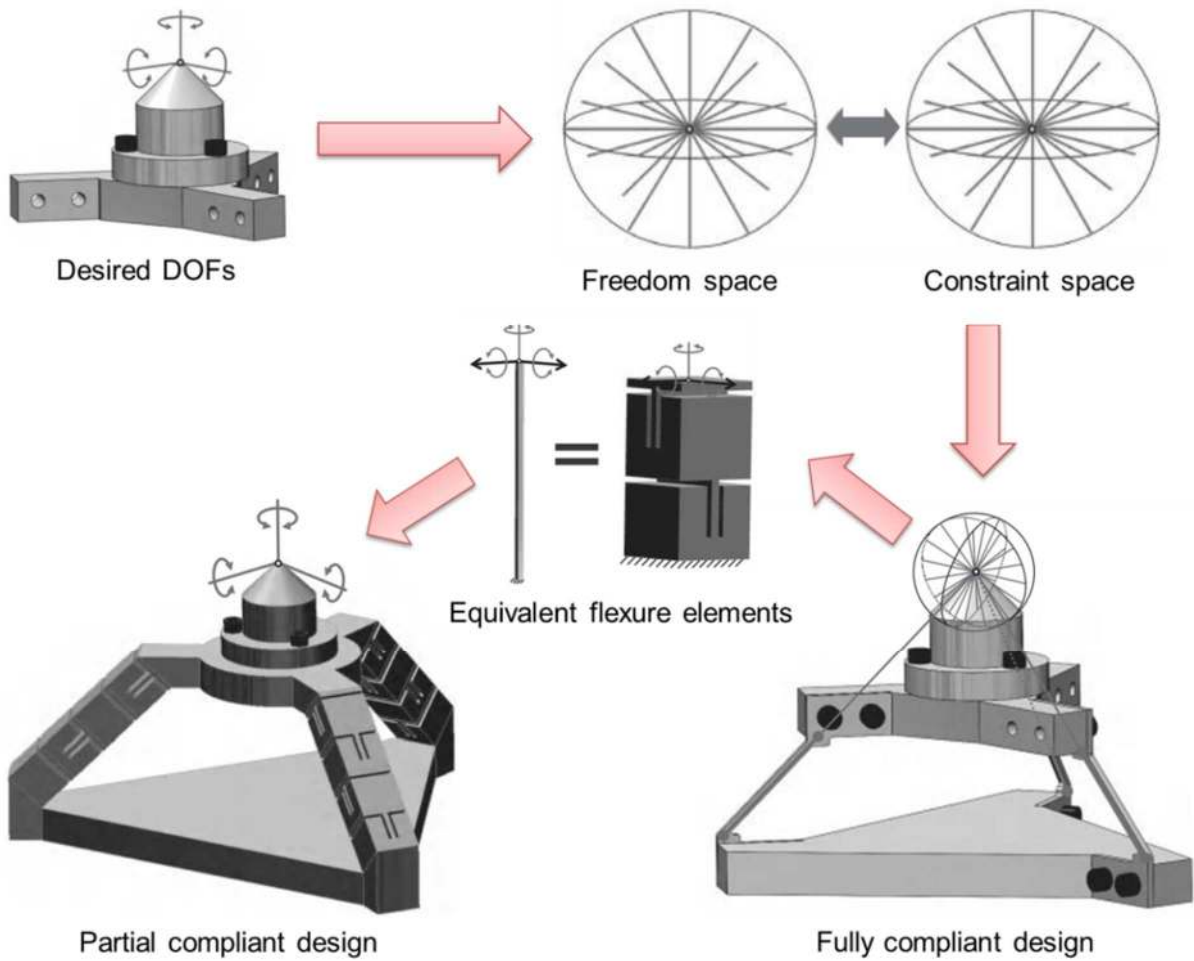
Figure 2.7: Synthesis process of a 3-DOF ($\theta_X - \theta_Y - \theta_Z$) CPM using FACT [1, 86].
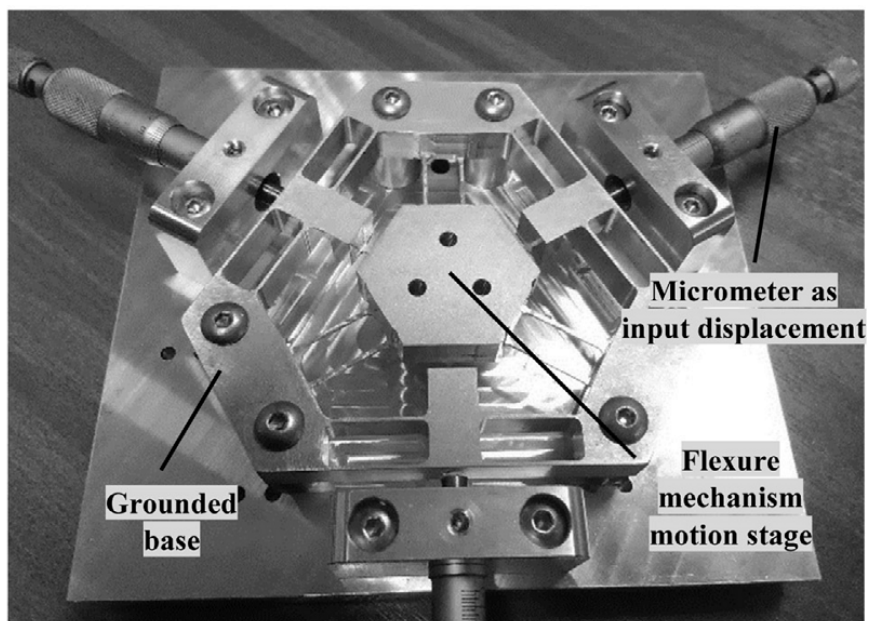
Figure 2.8: A 3-DOF ($\theta_X - \theta_Y - Z$) compliant manipulator synthesized by constraint-based approach [12].

Comparing to the rigid body replacement approach, the constraint-based approach is able to generate CPMs regardless of the corresponding architectures of rigid mechanisms. Although the constraint-based approach offers simple synthesis process, it is noted that the flexure elements within the CPM are chosen based on intuition of designers and the overall structure of the CPM is not optimized. As a result, CPMs synthesized by the constraint-based/FACT approach can satisfy the kinematics requirements, but the resulting designs are non-optimal and the desired mechanical (stiffness and dynamic) properties are difficult to achieve during the synthesis process.

2.1.3 Optimization approach

2.1.3.1 Homogenization method

Homogenization is a topological optimization method introduced by Bendsøe and Kikuchi [87] for continuum structures. Over the past decades, homogenization method has been improved and successfully applied in various fields, including synthesis of compliant mechanisms. The optimization problem of homogenization method is modeled by a group of elements where each of them is defined as a microstructure of unit cell constructed by solid material and void as illustrated in Figure 2.9.
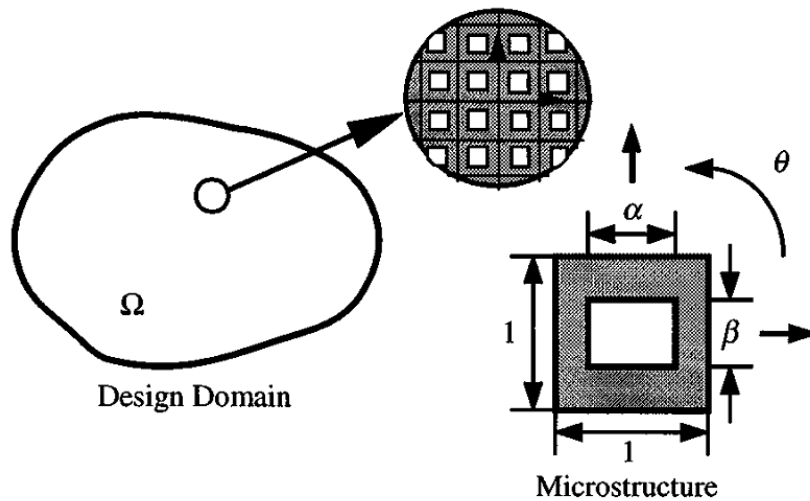
Figure 2.9: Details of a microstructure used in homogenization method [73].

19

Referring to Figure 2.9, an element is modeled by three individual variables α, β, and θ. The size of the void region is determined by α and β while the orientation of element is defined by θ. Basically, homogenization method can be considered as the size optimization of the void region. In particular, an element is fully solid or void when $\alpha = \beta = 0$ or $\alpha = \beta = 1$ respectively. If the values of α and β are different from 0 and 1, the property of element is undefined, and the element is represented by grey color in the final result. Figure 2.10 shows a compliant clamp with grey elements synthesized by homogenization method.
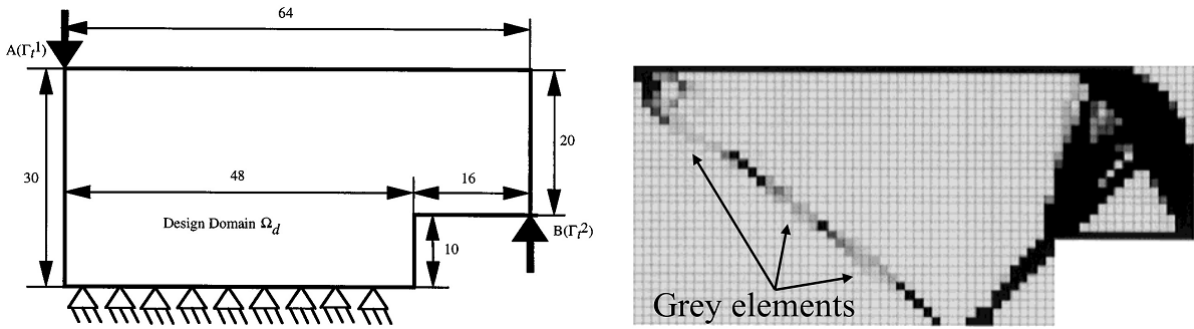
Figure 2.10: A compliant clamp synthesized by homogenization method [73].

The number of compliant mechanisms synthesized by homogenization method is limited due to the complicated process and long computational time [1]. Several compliant mechanisms designed by this method are presented in [73, 88]. Another drawback limits the application range of homogenization method is that some disconnected elements could be generated, they reduce the accuracy of results and may lead to infeasible structures.

2.1.3.2 Solid Isotropic Microstructure with Penalization (SIMP) method

SIMP, a topological optimization method for continuum structures, was first introduced by Bendsøe and Sigmund [89]. SIMP is the most popular topological optimization method and has been used in research as well as industry due to its simplicity and open source [90-93]. Each element in SIMP method is represented by a variable x_e ($0 \le x_e \le 1$) which determines the material property of the element.

Figure 2.11 illustrates three possible states that elements can achieve in SIMP method. If x_e is equal to 0 or 1, the element will be fully void or solid respectively. In many cases, its value is $0 < x_e < 1$ and produces a grey element. The grey element represents an undefined material which is weaker than the original material of entire structure. The number of grey elements can be reduced by applying some filters [94, 95] but they still exist and can affect the final results.
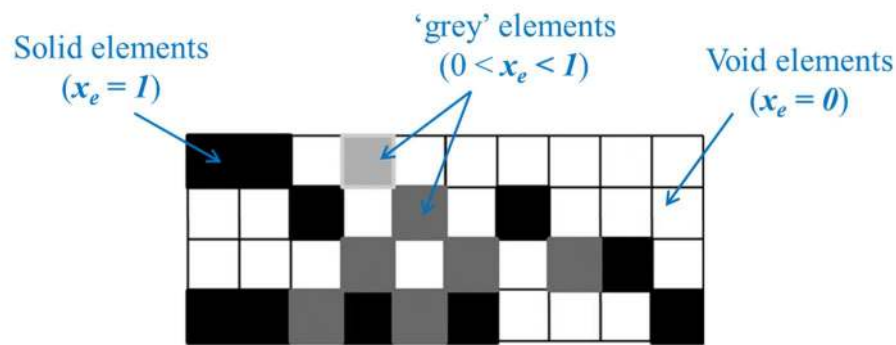
Figure 2.11: Three states of element in SIMP method [1].

With the open source, SIMP method has been improved and popularly used to synthesize numerous compliant mechanisms [58, 96-98] and CPMs [99]. However, SIMP method also generates disconnected elements as shown in Figure 2.12 that could lead to infeasible structures.
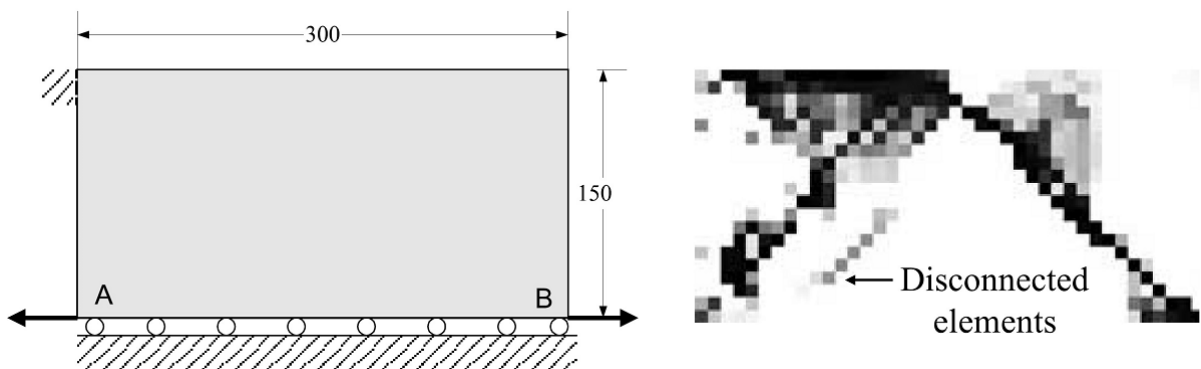
Figure 2.12: A compliant displacement inverter synthesized by SIMP method [98].

2.1.3.3 Evolutionary Structural Optimization (ESO) method

ESO is a topological optimization method introduced by Xie and Steven [100]. To obtain the optimal topology, material is distributed inside a design domain. During the optimization process using Genetic Algorithm (GA), redundant elements are removed from the design domain to produce lighter structures that satisfy defined requirements. By using this method, the grey elements are eliminated because elements only have two states, i.e., solid and void. The later version of ESO, namely bi-directional evolutionary structural optimization (BESO) method, allows to remove redundant elements while other elements are simultaneously added into the design domain to improve the computational time [101].

A number of compliant mechanisms have been developed using ESO/BESO method [57, 59, 66, 102-104]. Figure 2.13 illustrates a compliant gripper synthesized by BESO method. Although ESO/BESO method can successfully eliminate grey elements, the disconnected elements still exist and could generate impractical structures.

Figure 2.13: A compliant gripper synthesized by BESO method [59].

2.1.3.4 Level set method

Level set, a topological optimization method for continuum structures based on the numerical algorithm of fronts propagating with curvature-dependent speed, was developed by

Osher and Sethian [105]. The optimal topology is obtained by the resulting moving-boundaries of Hamilton-Jacobi partial differential equation [106-108]. In contrast to the mentioned methods, level set method is able to generate smooth boundaries due to its mesh-independence principle. Figure 2.14 illustrates the generation of topology using level set method. Here, ϕ is the surface represents the level set function and c is a constant [109]. The region defined by $\phi = c$ represents the resulting material domain where Γ is the boundary of the domain, Ω and D demonstrate the areas of solid material and void respectively.

Level set function   *Resulting material domain*
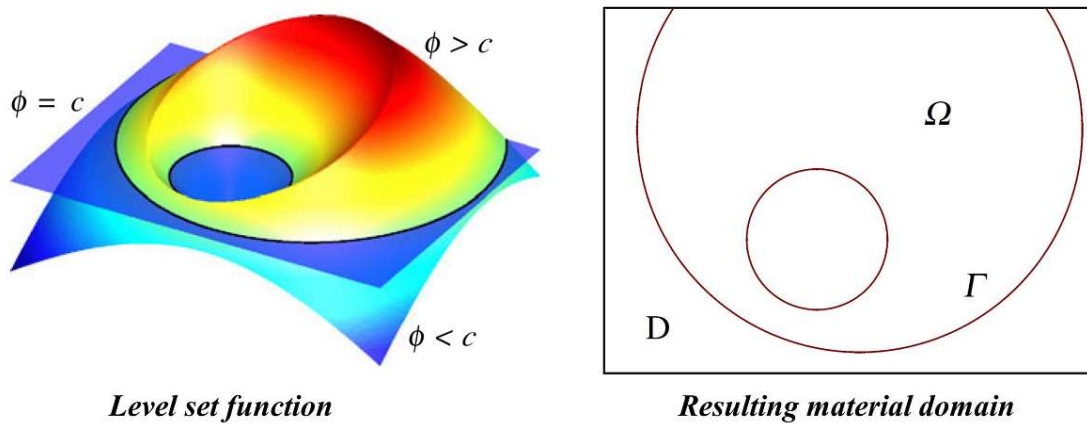
Figure 2.14: Demonstration of level set method [109].

In recent years, level set method has been the focus of development because it can generate smooth profiles and no post-processing is needed to refine the designs. Therefore, a number of compliant mechanisms for different applications have been synthesized by this method [56, 60, 61, 64, 67, 107, 110, 111]. An example of compliant gripper designed by level set method is shown in Figure 2.15. It is seen that the result of level set method has smoother surfaces as compared to similar structure designed by BESO method shown in Figure 2.13.
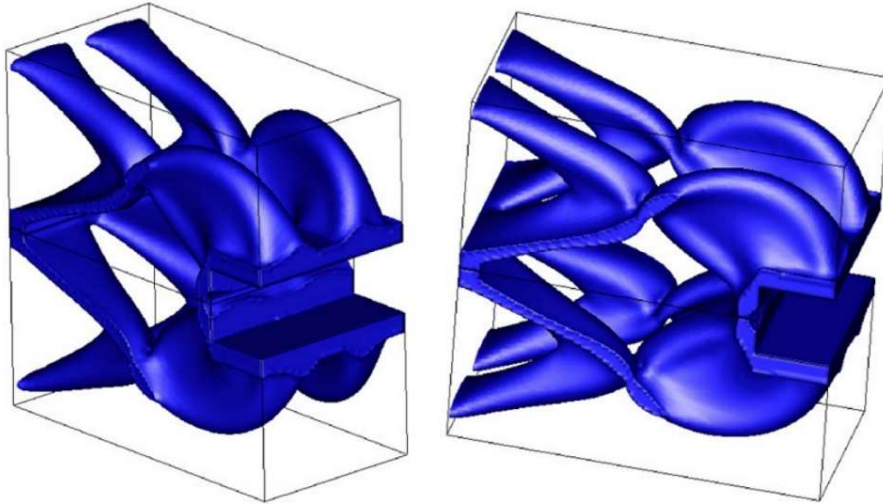
Figure 2.15: A compliant gripper synthesized by level set method [107].

Using level set method, the final design corresponds to the intersection between the level set surface and a specific plane, and disconnected regions may be present. Furthermore, the convergence of this method is dependent on the formulation of the level set function [109].

2.1.3.5 Ground structure method

The ground structure method is a topological optimization method that utilizes discrete elements (trusses or frames) to represent continuum design domains. One of the first research that used ground structure method to synthesize compliant mechanisms was by Frecker et al. [112]. In ground structure method, the optimal topology is defined by the connectivity of beam/truss elements and the design variables are the cross-sectional areas of the elements. If an area is smaller than a pre-defined limit, the corresponding element will be disappeared. Hence, the grey elements can be eliminated. The synthesis process of a compliant gripper using ground structure method is demonstrated in Figure 2.16.
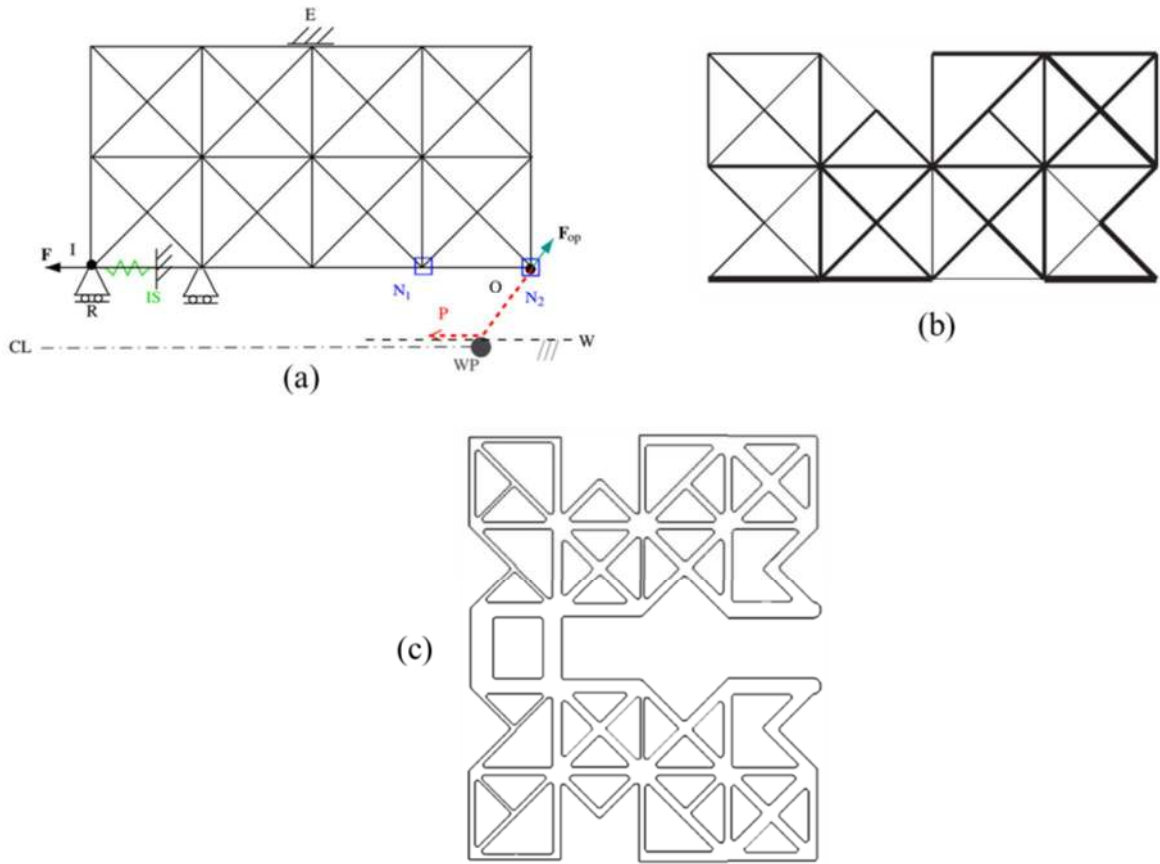
Figure 2.16: Demonstration of ground structure method (a) design domain, (b) optimized result and (c) final design [113].

Ground structure method has been widely used to synthesize compliant mechanisms due to the simple process and low computational resource [63, 112-117]. However, the disconnected structures could be present and generate infeasible results as shown in Figure 2.17.
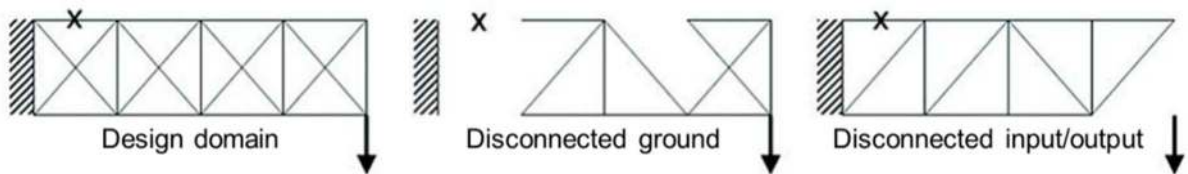
Figure 2.17: Disconnected structures generated in ground structure method [55].

2.1.3.6 Morphological representation method

Morphological representation method, introduced by Tai and Chee [72], is also known as path generating method [71, 118]. It is a structural optimization method specialized for

synthesizing compliant mechanisms. This method was developed to overcome the limitations of the other optimization methods, e.g., grey elements and disconnected structures. It employs several defined paths as skeletons for distributing material. During the optimization process, the geometries of paths and material distribution are determined by GA.

Figure 2.18 demonstrates the synthesis process of a compliant mechanism using morphological representation method. First, a skeleton that connects the input, output and constraint points is modeled by Bezier curves as shown in Figure 2.18a. Subsequently, the original elements that represent the solid material are added along the curves to create a basic structure as illustrated in Figure 2.18b. Then, GA is used to determine the optimal geometries of Bezier curves and additional material, represented by 'flesh' elements, will be added at suitable positions within the structure as demonstrated in Figure 2.18c in order to enhance the performance for the entire compliant mechanism. Figure 2.19 shows a compliant gripper synthesized by morphological representation method.
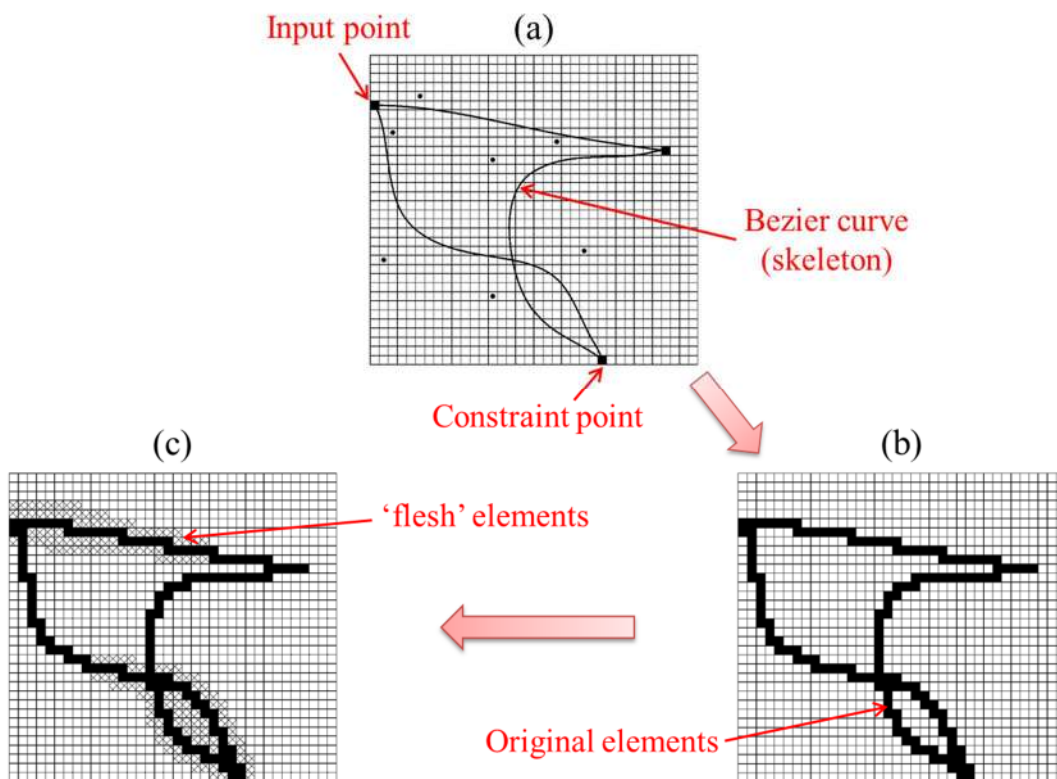
Figure 2.18: Synthesis process of morphological representation method [71].
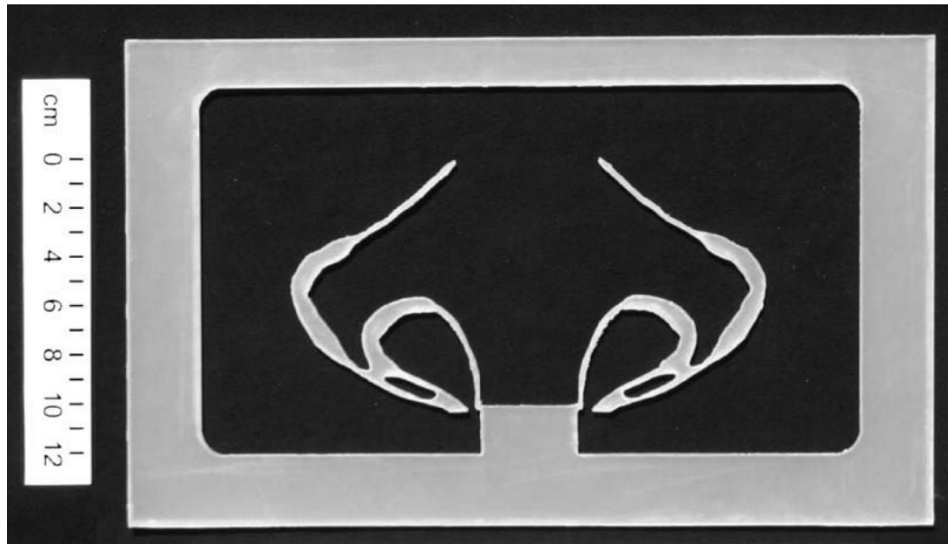
Figure 2.19: A compliant gripper synthesized by morphological representation method [118].

Despite overcoming the shortcomings of existing optimization methods, morphological representation method is only suitable for synthesizing planar compliant mechanisms [14, 71, 72, 118, 119], spatial designs are difficult to obtain due to the complexity of structure modeling.

2.1.3.7 Mechanism integrated method

Mechanism integrated method was introduced by Lum et al. for synthesizing CPMs by integrating configuration of traditional rigid-mechanisms into the structural optimization process [75]. Traditional mechanism is used as the seeds for a special mapping technique based on evolutionary process. Compliant mechanism is modeled by adding elements inside the region defined by a pair of cubic – harmonic curves and their reflections. A variable, m, is used to determine the distribution of material as shown in Figure 2.20. In particular, if $m = 1$ or 2, material is distributed in the region created by a pair of curves on the right or left respectively; and if $m = 3$, the regions at both sides will be filled with material.
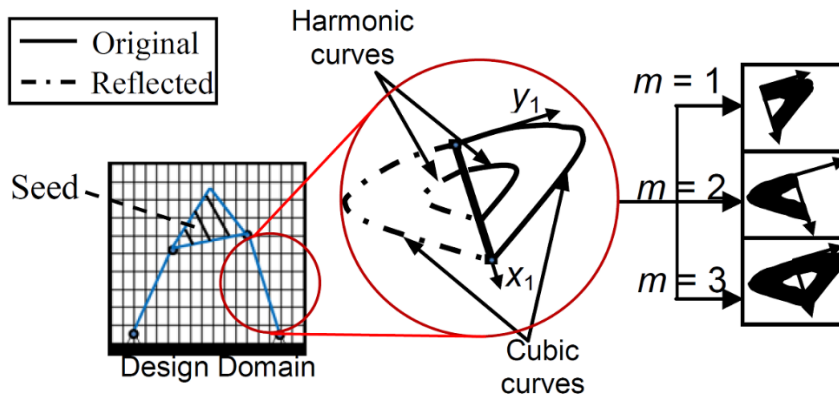
Figure 2.20: Concept of mechanism integrated method [120].

This method can be applied to synthesize multi-DOF CPMs. First, the seed is defined by a classical rigid-mechanism which has the same DOF as the CPM. After modeling the design domain as illustrated in Figure 2.20, GA will be carried out to determine the optimal structure of CPM by changing the geometries of the linkages and curves until the best result is achieved. An example of using mechanism integrated method to synthesize a prismatic joint (1-DOF CPM) based on the traditional four-bar linkage mechanism is shown in Figure 2.21.
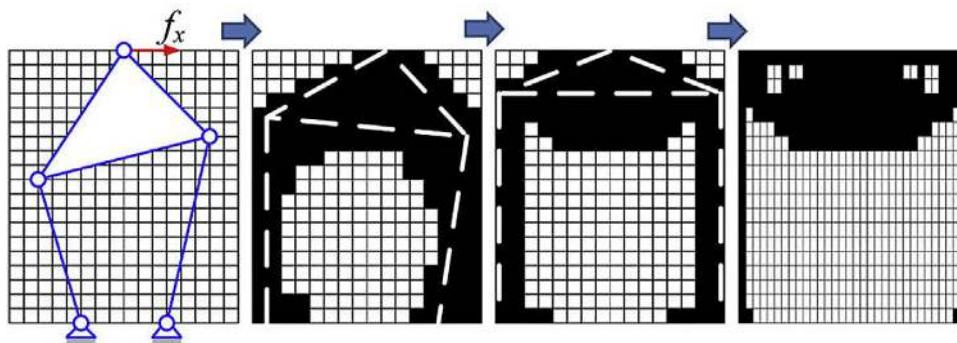
Figure 2.21: Synthesis process of a prismatic compliant joint [75].

To synthesize multi-DOF designs such as 3-DOF ($X - Y - \theta_Z$) CPM, the common 3-legged configuration with a group of Prismatic-Prismatic-Revolute (P-P-R) joints in a limb is selected as the schematic for the synthesis process as shown in Figure 2.22a. The final design of CPM can be obtained by determining the optimal structure of the limbs. Here, each limb is considered as a 3-DOF compliant mechanism and the ten-bar linkage mechanism having the

same DOF is used as the seed. The evolution of a limb during the optimization process is demonstrated in Figure 2.22b. It is observed that after a specific number of iterations (or 18 generations), the result converges and the final structure of limb is achieved.
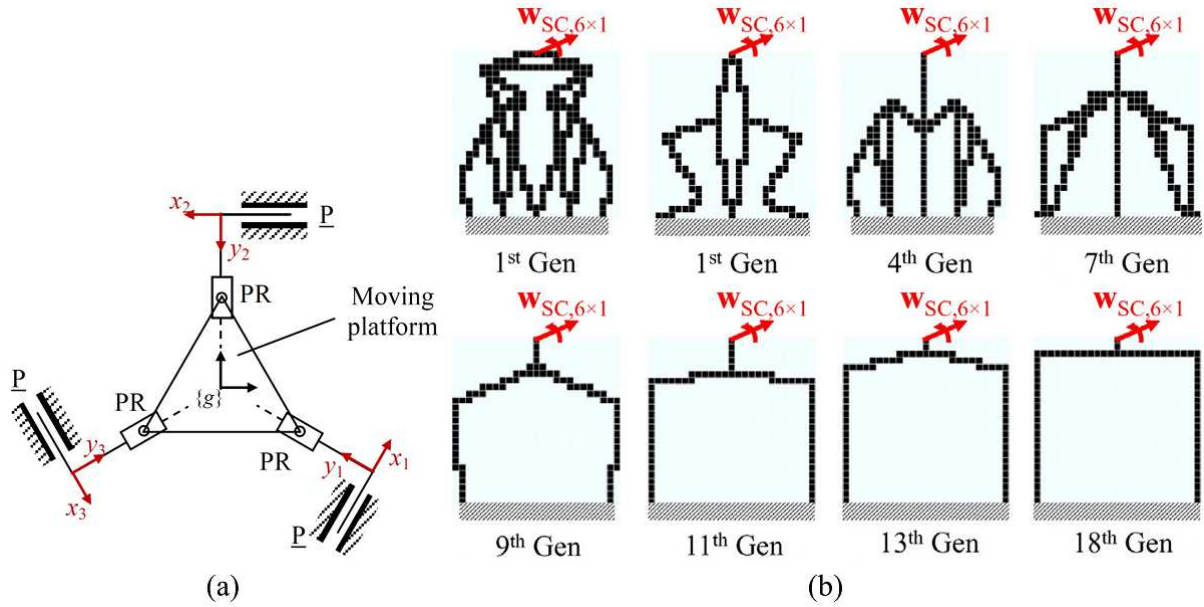
Figure 2.22: (a) Schematic of 3-DOF ($X - Y - \theta_Z$) CPM [120] and (b) evolution of the structure of a limb during the synthesis process [74].

A major benefit offered by the mechanism integrated method is the ability to optimize dynamic behavior of CPMs. After the stiffness optimization process shown in Figure 2.22, the obtained structure of limb is used as the design domain for the dynamic optimization process. As the dynamic response can be improved by determining the suitable distribution of mass within the design domain, two symmetrical cubic curves are used to create the regions for adding material as illustrated in Figure 2.23a. The evolutionary process of the limb is demonstrated in Figure 2.23b, the geometries of curves are changed during the optimization in order to find the best material distribution. After 10 generations, the optimal structure of limb that can produce the best dynamic behavior for the entire CPM is achieved. The final design of the CPM based on the optimized results is shown in Figure 2.23c.
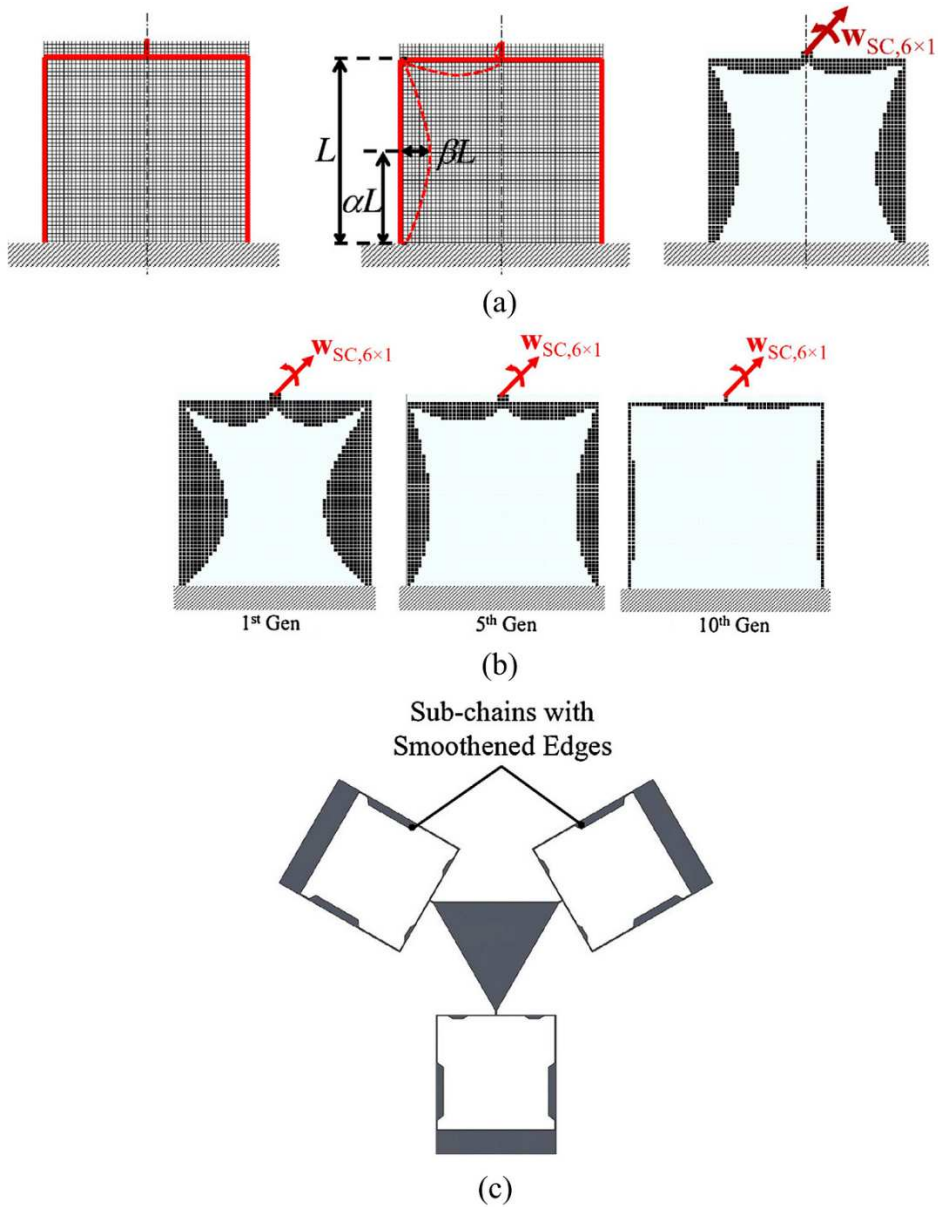
Figure 2.23: (a) Problem modeling of dynamic optimization, (b) dynamic optimization process and (c) optimized structure of the CPM [74].

In summary, both the stiffness and dynamic properties of CPMs can be optimized by the mechanism integrated method. This method is developed to synthesize multi-DOF CPMs and most importantly, the successful implementation of dynamic optimization allows it to overcome the common drawback of existing methods. Nevertheless, the mechanism integrated method is only applicable for synthesizing multi-DOF planar-motion CPMs such as the 3-DOF $(X-Y-\theta_Z)$ designs [74, 75, 121], spatial-structure CPMs are unable to obtain due to limitations of the mapping technique. In addition, several objective functions were proposed in the

mechanism-integrated method in order to synthesize multi-DOF CPMs. Yet, the final units of such objective functions are not well defined because the components within the stiffness matrix of CPM have different units such as N/m and Nm/rad.

2.1.4 Summary

Based on the literatures, the advantages as well as disadvantages of the three synthesis approaches are summarized in Table 2.1.

Table 2.1: Comparison of synthesis approaches.

Synthesis approach	Advantages	Disadvantages
Rigid body replacement	- Able to synthesize any CPM. - A large number of compliant joints are available.	- Depend on intuition of designers and existing architectures of rigid-mechanisms.
Constraint-based	- Simple synthesis process based on FACT library.	- Difficult to synthesize stiffness and dynamic properties.
Optimization	- Able to synthesize any CPM. - Independent of intuition of designers.	- Depend on problem modeling and objective function.

From Table 2.1, it can be said that the optimization approach is most suitable for synthesizing complex multi-DOF CPMs since it is independent on human intuition. However, the modeling of optimization problem as well as the objective function need to be well defined in order to obtain good designs. Table 2.2 shows the properties of existing optimization methods.

Table 2.2: Properties of optimization synthesis methods.

Optimization method	Spatial structures	Dynamic optimization support	Elimination of 'grey' elements	Elimination of disconnected elements
Homogenization	✓	✗	✗	✗
SIMP	✓	✗	✗	✗
ESO/BESO	✓	✗	✓	✗
Level set	✓	✗	✓	✗
Ground structure	✓	✗	✓	✗
Morphological representation	✗	✗	✓	✓
Mechanism integrated	✗	✓	✓	✓

From Table 2.2, it is seen that each optimization method has its own merits and limitations. Among them, the mechanism integrated method is the best candidature for synthesizing CPMs in precise motion systems since it is able to optimize both the stiffness and dynamic properties. However, this method is unable to synthesize spatial structures due to the shortcomings of its modeling technique.

The synthesis of multi-DOF CPMs using optimization approach is characterized by the objective function. Objective functions, based on mutual strain energy [88], mechanical advantage [94], artificial spring [94], efficiency [122] and characteristic stiffness [110], have been proposed for synthesizing 1-DOF CPMs such as compliant grippers, as well as force and motion amplifiers/inverters. However, these objective functions only focus on the behaviors at the input and output positions while the stiffness in non-actuating directions is not considered, and are not applicable for CPMs in motion systems. In order to synthesize multi-DOF CPMs for positioning applications, several objective functions based on stiffness ratio [74] and kinematics with actuating isolation [99] have been reported recently. However, the units of these objective functions are not consistent and well-defined due to the mixing of different

units of components in the stiffness matrix such as N/m or Nm/rad. Therefore, an objective function that offers a well-defined unit and the ability to synthesize multi-DOF CPMs is essential for the development of flexure-based positioning systems.

2.2 3-Legged CPMs for Motion Systems

2.2.1 Fundamentals and benefits

In precise motion systems, CPMs are used as frictionless bearing-supports in order to generate highly repeatable motions. To adapt numerous applications in different industrial fields, motion systems are required to perform a variety of output motions. Thus, the development of multi-DOF CPMs is essential. Past literatures demonstrate that a vast number of multi-DOF CPMs, vary from 2 DOF to 6 DOF, have been proposed. In addition, most of those CPMs are synthesized based on two main architectures, which are 4-legged and 3-legged configurations. While the 4-legged configuration is preferred in 2-DOF ($X - Y$) CPMs [15, 26, 29, 31, 36, 37, 39, 53] due to the advantage in synthesizing two decoupled in-plane linear motions, the 3-legged configuration is widely used to design other multi-DOF CPMs. Developed based on three rotational-symmetric compliant limbs, 3-legged CPM (3L-CPM) is able to provide not only more compact structure and higher flexibility than the 4-legged counterparts but also various spatial output motions, e.g., 3-DOF in-plane motions ($X - Y - \theta_Z$), 3-DOF out-of-plane motions ($\theta_X - \theta_Y - Z$), and also 6-DOF motions.

Due to these advantages, 3L-CPM is the focus in this research. Any term of CPM used in the remaining of this thesis is referred to 3L-CPM. Characteristics of some popular CPMs will be presented in the following subsections.

2.2.2 3-DOF planar-motion ($X - Y - \theta_Z$) CPM

3-DOF planar-motion ($X - Y - \theta_Z$) CPM, which has been popularly used in numerous positioning stages in microscopes, micro/nano manufacturing systems, micro-electro-mechanical systems (MEMS), etc., can be considered as the most common type of multi-DOF CPMs. A number of 3-DOF ($X - Y - \theta_Z$) CPMs have been synthesized by the rigid body replacement and optimization approaches [40-42, 46, 74, 75, 99, 121, 123-128]. Two existing designs of 3-DOF planar-motion ($X - Y - \theta_Z$) CPM developed for precise motion system [42] and MEMS [128] are shown in Figure 2.24a and Figure 2.24b respectively.

| (a) | (b) |
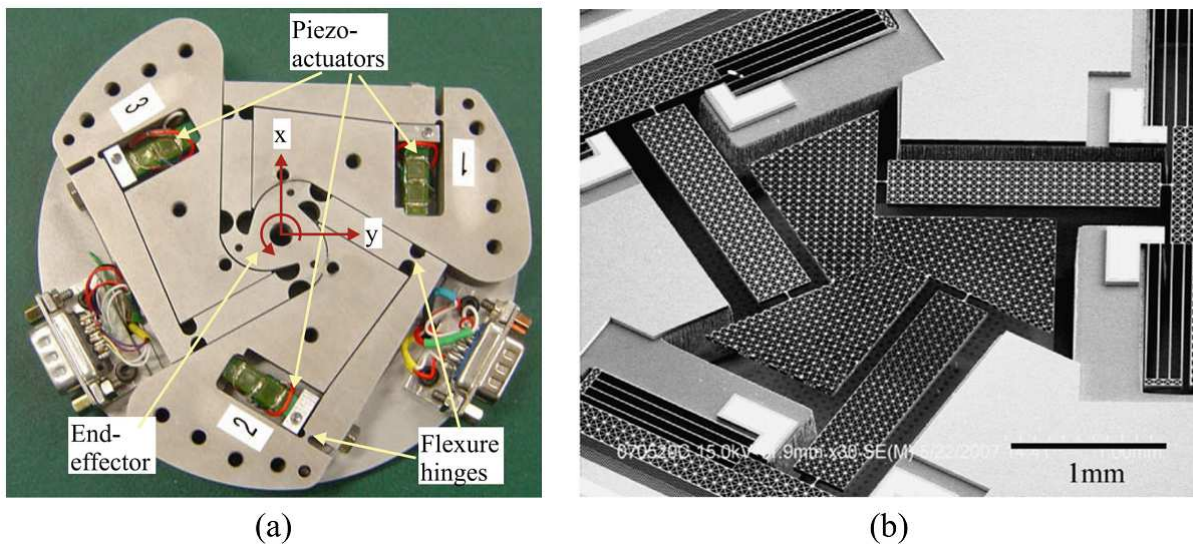
Figure 2.24: 3-DOF planar-motion ($X - Y - \theta_Z$) CPMs used in (a) precise motion system [42] and (b) MEMS device [128].

For large-workspace 3-DOF ($X - Y - \theta_Z$) CPMs synthesized by the rigid body replacement approach, the stiffness and dynamic properties are limit with the stiffness ratio and dynamic response being less than 60 and 45 Hz respectively [74]. Such limitations have been overcome by using optimization approach. In particular, a 3-DOF ($X - Y - \theta_Z$) CPM with large workspace of 1.2 mm × 1.2 mm × 6° as shown in Figure 2.25 has been synthesized by the mechanism integrated method [74]. This design is able to produce high stiffness ratios of

130 for translations and 108 for rotations, and fast dynamic response via the first resonance frequency of 117 Hz.
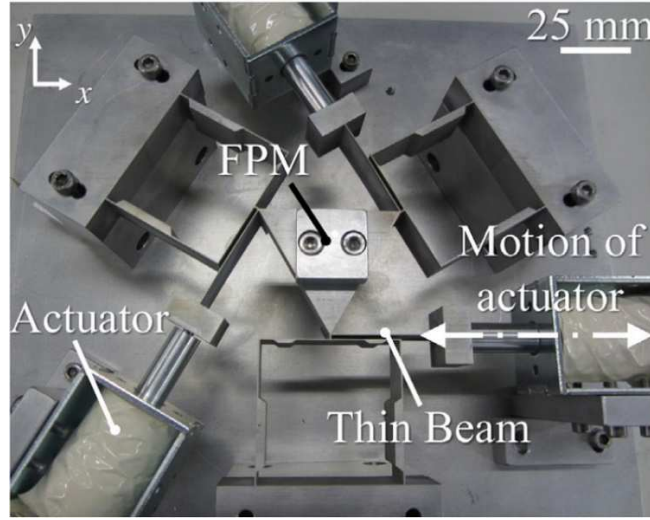
Figure 2.25: Large-workspace 3-DOF ($X - Y - \theta_Z$) CPMs with optimized stiffness and dynamic properties [74].

Recently, another 3-DOF ($X - Y - \theta_Z$) CPM synthesized by the same method has been introduced [121]. This CPM is able to perform better actuating stiffness, higher stiffness ratio and larger workspace (2.5 mm × 2.5 mm × 10°), but lower dynamic response (70 Hz). This demonstrates that the minimum actuating stiffness and maximum dynamic behavior are unable to be accomplished together due to the conflict of stiffness and dynamic properties, i.e., the faster dynamic response can be achieved when increasing the stiffness of structure.

2.2.3 3-DOF spatial-motion ($\theta_X - \theta_Y - Z$) CPM

CPM with 3-DOF spatial motions ($\theta_X - \theta_Y - Z$), another popular type of multi-DOF CPMs, is often used in precision manipulators and optical alignment systems [17, 83, 129-134]. Past literatures demonstrate that the number of synthesized 3-DOF ($\theta_X - \theta_Y - Z$) CPMs is less than the 3-DOF ($X - Y - \theta_Z$) CPMs due to the difficulties in synthesizing out-of-plane motions based on existing architectures of conventional mechanisms. Examples of two developed

precision manipulators using 3-DOF ($X - Y - \theta_Z$) CPMs for driving micro-finger module and nanoimprint lithography process are shown in Figure 2.26a and Figure 2.26b respectively.
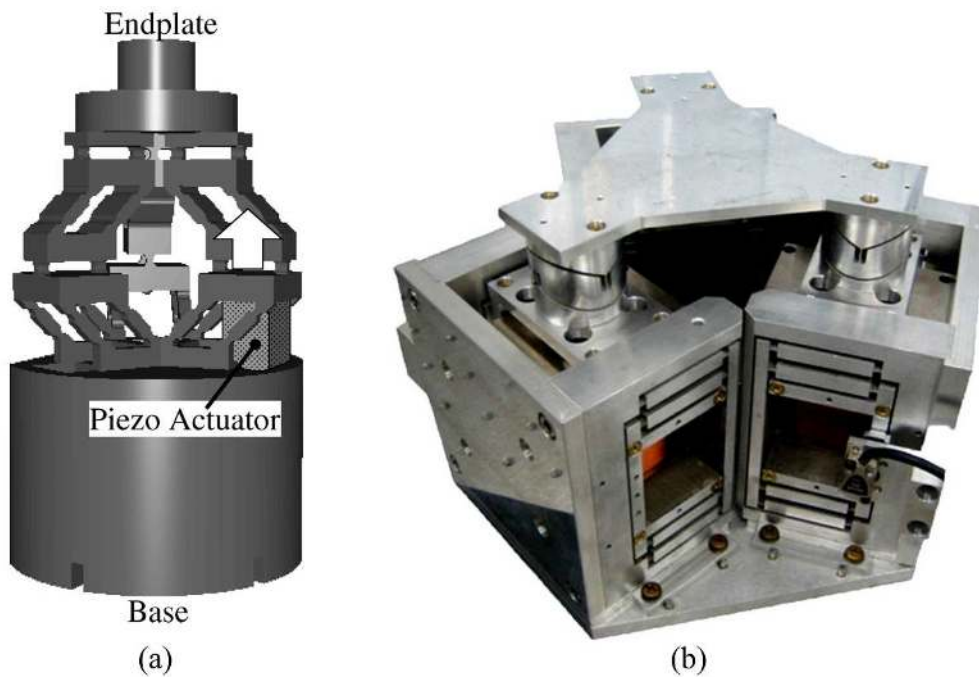
Figure 2.26: Manipulators developed based on 3-DOF ($\theta_X - \theta_Y - Z$) CPMs used in (a) micro-finger module [132] and (b) nanoimprint lithography process [129].

As most existing 3-DOF ($\theta_X - \theta_Y - Z$) CPMs are developed by the rigid body replacement approach, their dynamic characteristics have not been synthesized. Figure 2.26b is the 3-DOF ($\theta_X - \theta_Y - Z$) CPM that can produce a large workspace of up to $5° \times 5° \times 5$ mm. However, its mechanical behaviors are limited through the low stiffness ratio of less than 2 and slow dynamic response of about 15 Hz. Those performances are unsatisfied the requirements of advanced motion systems. In addition, the complex structures of 3-DOF ($\theta_X - \theta_Y - Z$) CPM are unable to be fabricated monolithically using computer-numerical-control (CNC) machining processes. As demonstrated in Figure 2.26b, the CPM is built by assembling many sub-components together. As a result, its performance can be affected by various unpredictable sources, such as assembly errors. Thus, the development of a 3-DOF ($\theta_X - \theta_Y - Z$) CPM with large workspace, good stiffness and dynamic properties is needed to create advanced motion systems.

2.2.4 6-DOF CPM

As 6-DOF design is the most complicated type of multi-DOF CPMs, the number of 6-DOF CPMs that have been proposed is very limited [49, 135-137]. The structure of a 6-DOF manipulator synthesized by the rigid body replacement approach is illustrated in Figure 2.27.
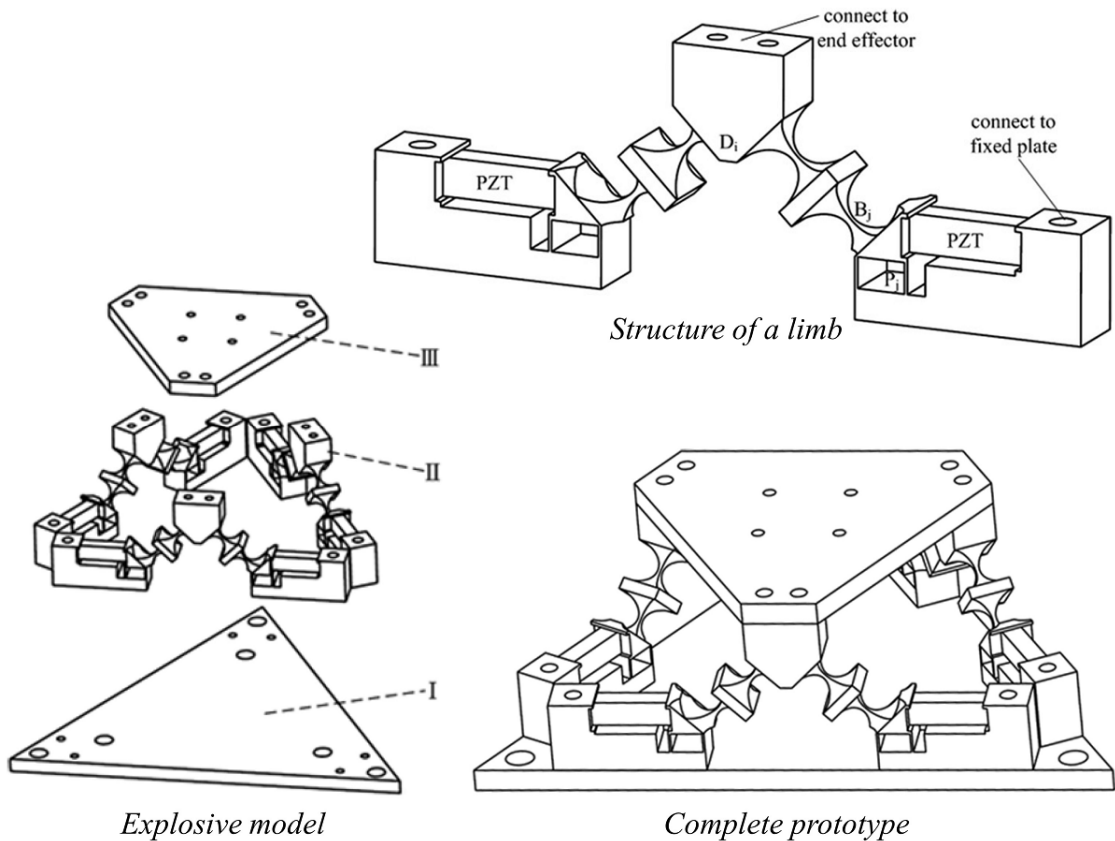
Figure 2.27: 6-DOF CPM synthesized by rigid body replacement approach [49].

It is seen from Figure 2.27, the CPM is created by three symmetrical limbs with each limb being constructed by a parallel pair of flexure chains. Due to the complex structure, it is separated into many parts for machining and hence, the performance of the final prototype can be affected by assembly errors. This design offers a small deformation range with 8 μm for translations and 200 μrad for rotations. However, its dynamic behavior was not synthesized.

Another design of 6-DOF CPM synthesized by the constraint-based approach is illustrated in Figure 2.28. This CPM is able to produce a workspace of < 1 mm for translations

and < 1° for rotations, and the first natural frequency of 40 Hz. Depending on the performances of existing 6-DOF CPMs, it is suggested that the workspace must be enlarged to few millimeters and degrees while the dynamic response needs to be improved to fulfill the requirements of advanced positioning devices.
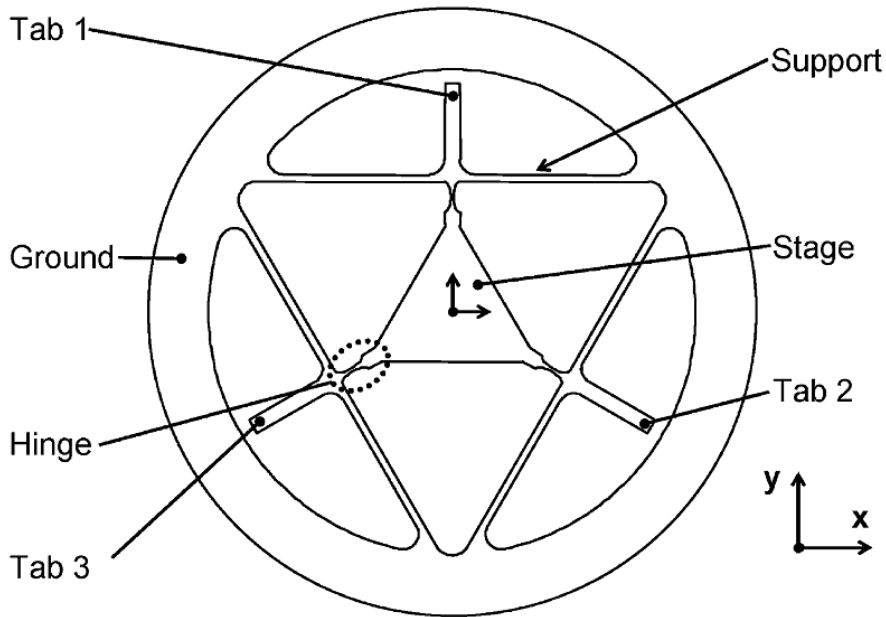
Figure 2.28: 6-DOF CPM synthesized by constraint-based approach [135].

2.2.5 Discussion

Based on the characteristics of the existing multi-DOF CPMs, only the 3-DOF planar-motion ($X - Y - \theta_Z$) CPM has been successfully optimized for stiffness property, dynamic response and workspace. The other types of multi-DOF CPM, i.e., 3-DOF spatial motions ($\theta_X - \theta_Y - Z$) and 6-DOF CPMs, have limited stiffness performances while the dynamic behaviors have not been the focus of synthesis. Therefore, the optimized designs of these CPMs need to be developed.

As multi-DOF CPMs are essential in positioning systems, their motion property directly determines the accuracy of output motions. A CPM is desired to produce a specific motion under the actuating load in the same direction, any undesired parasitic motion can reduce the

overall performance of entire positioning system. However, past literatures have shown that the motion property of existing CPMs is generally neglected [40-43, 46, 48, 49, 99, 123-126, 135, 136]. Because the motion decoupling of CPMs plays an important role in precision devices, it must be well specified and considered in the synthesis process.

For CPMs having complex structures such as the designs shown in Figure 2.26 and Figure 2.27, the abilities of machining techniques must be considered during the design process so that designers can separate structures for further fabrication. Nevertheless, the quality of assembly structures is determined by unpredictable assembly errors; and even the additional masses of mounting parts, e.g., screws, nuts, dowel pins, etc., may change the dynamic performance of CPMs. At present, 3D printing technology is the best solution for manufacturing functional products monolithically and it can be exploited to fabricate complex CPMs to eliminate assembly errors.

2.3 3D-Printed CPMs

As presented, EBM is the best solution for fabricating CPMs for precision systems due to the nearly-full density of printed material. However, this fabrication technique also has some drawbacks such as high surface roughness, thermal distortion and lower accuracy as compared to traditional machining methods. Therefore, the number of EBM-printed CPMs developed for precise positioning applications is very limited because many uncertainties may affect the predicted data.

One of the first EBM-printed CPMs have been developed is the 2-DOF pointing CPM for positioning the rotation angles of spacecraft thruster, antenna or solar systems [79]. The 3D-printed prototype of this CPM built by Titanium alloy Ti6Al4V is shown in Figure 2.29a and its actual application in aerospace field is demonstrated in Figure 2.29b. FEA and

experimental measurements have been carried out to evaluate the performance of the pointing mechanism, the measured data agrees with the analytical results demonstrating that the 3D-printed prototype can be applied in positioning applications.

(a)   (b)
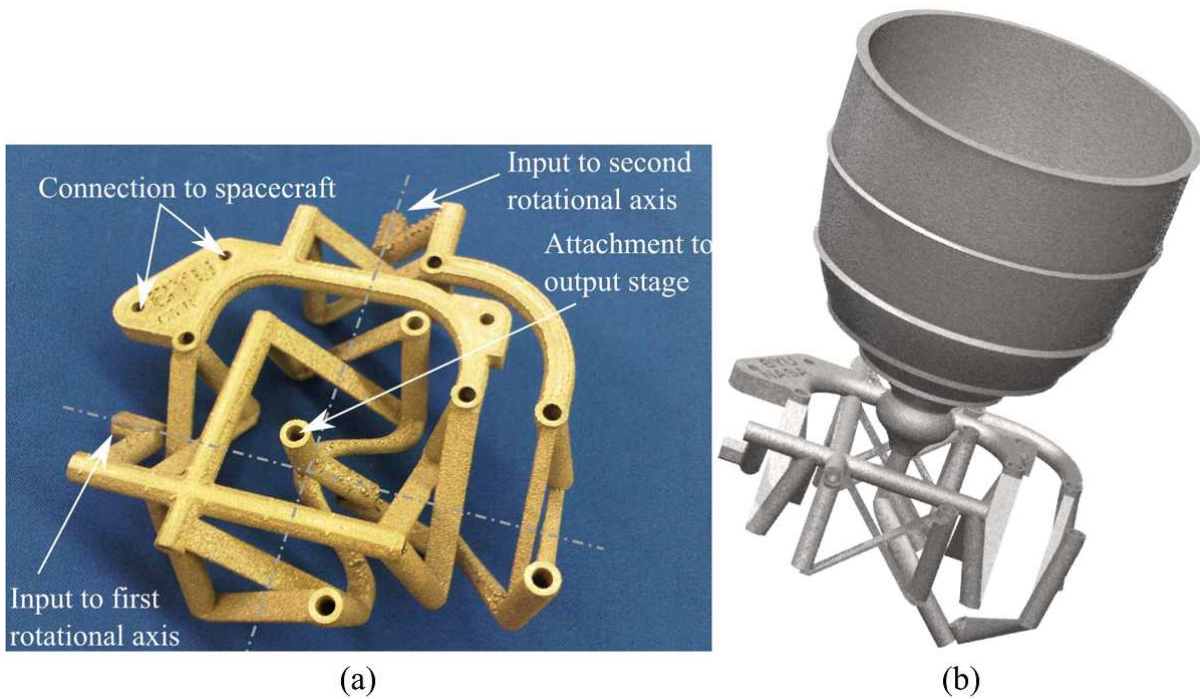
Figure 2.29: EBM-printed 2-DOF pointing CPM (a) physical prototype built by Ti6Al4V material and (b) integrated with a thruster for positioning application [79].

Even though the performance of the 3D-printed pointing CPM has been demonstrated, there are numerous matters need to be explored. As this CPM was developed to adapt large payload of aerospace systems, the thickness of flexures was defined as ≥ 1 mm and hence, it is much stiffer than positioning systems in other fields. As a result, the actuating forces/moments need to be large and lead to bulky structures that are not suitable for precision devices.

Recently, a 2-DOF ($X - Y$) CPM fabricated by EBM technology and Ti6Al4V material as shown in Figure 2.30 has been developed for a precision positioner [138]. The thickness of flexures was chosen as ~ 0.7 mm in order to obtain low actuating stiffness. Experimental results demonstrate that the performance of the 3D-printed prototype is not well determined by the

designed thickness. In particular, for sub-millimeter-thick flexures, the actual thickness of EBM-printed flexures mismatches the designed value due to the high surface roughness.
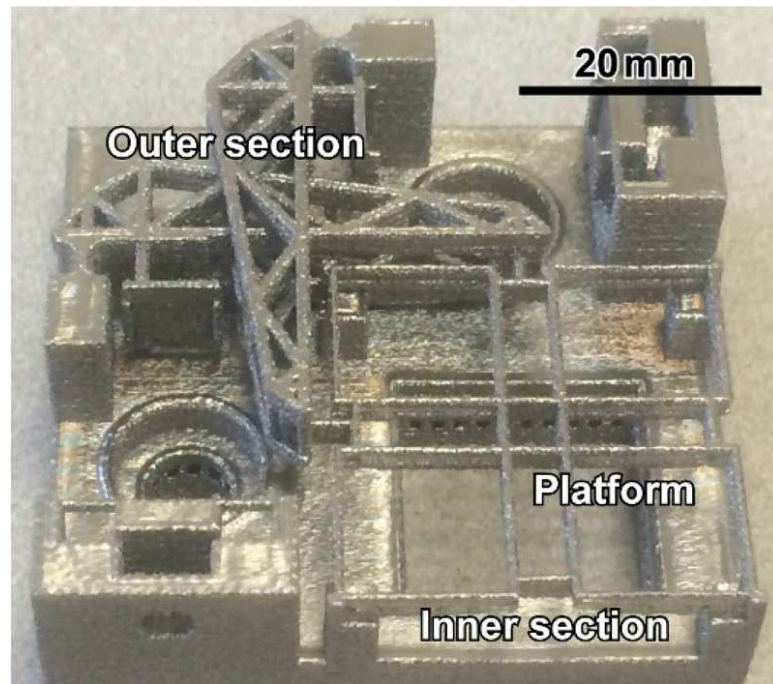
Figure 2.30: EBM-printed 2-DOF ($X - Y$) nano-positioner [138].

To overcome the problem, an equivalent Young's modulus of material has been proposed to compensate the difference between designed and fabricated thicknesses [138]. However, the equivalent Young's modulus is derived based on the measured thickness and estimated surface roughness of the printed flexures, that are inconsistent due to various manufacturing conditions, such as different building directions and orientations of flexures. Thus, a more general compensation approach is necessary to well predict the characteristics of EBM-printed flexures.

Another important benefit offered by 3D printing technology, the ability to build lattice/cellular structures, has been exploited to fabricate compliant mechanisms. Previous literatures demonstrate that the stiffness performance of compliant systems can be improved by using lattice flexures [139]. Several prototypes of compliant joints with lattice flexures fabricated by EBM method and Ti6Al4V are shown in Figure 2.31.
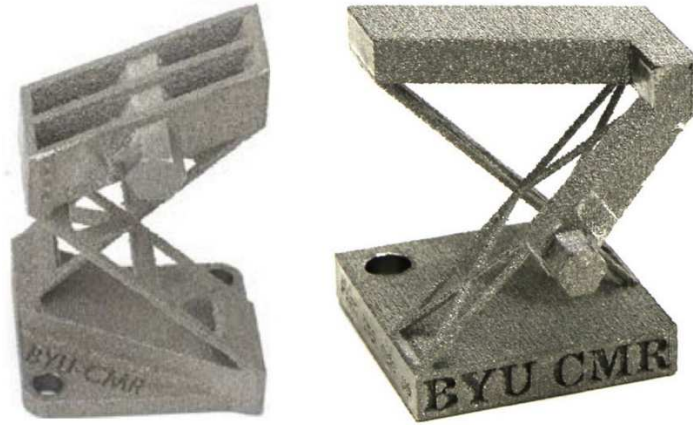
Figure 2.31: Compliant joints with lattice flexures fabricated by EBM method [139].

As 3D-printed CPMs are fabricated monolithically, their dynamic characteristics can be well determined by the relationship between stiffness and mass distribution within the structures. In order to improve the dynamic behavior of CPMs, the masses of rigid bodies can be reduced while their stiffness property is remained. Rigid bodies with low mass and high stiffness can be achieved with cellular/lattice structures. Various cellular structures have been presented in [140] and successfully fabricated by EBM method as shown in Figure 2.32. They can be employed to create CPMs with better dynamic properties.
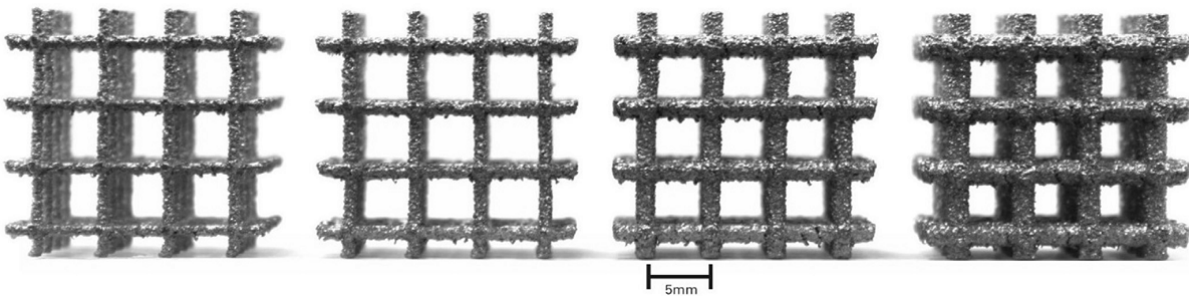
Figure 2.32: Lattice structures fabricated by EBM method [141].

2.4 Conclusion

In this Chapter, three synthesis approaches for CPM are first described and compared. This is followed by the review of 3-legged CPMs for motion systems and the fabrication of CPMs by 3D printing. It has been seen that CPM has become an essential device in many

industrial fields and the performance of CPMs hinges on the design methodology and fabrication technology. From the review, the following research gaps have been identified in order to improve the performance of CPMs in advanced motion systems:

- For the design methodology, a novel optimization method and a new objective function with well-defined unit for synthesizing multi-DOF spatial-motion CPMs with optimal stiffness and dynamic characteristics are important. Furthermore, the criteria for designing CPMs must be able to take into consideration the motion property i.e. coupled or decoupled.

- For the fabrication technology, while EBM can be the best solution for monolithically fabricating CPMs with complex structures and high density, the performance of EBM-printed flexible structures has not been sufficiently investigated. Hence, it is necessary to explore the mechanical properties of EBM-printed flexures and assess experimentally the performance of EBM-printed CPMs in precise motion systems.

CHAPTER 3
BEAM-BASED METHOD

3.1 Background

Depending on the limitations of existing methods, a novel method based on structural optimization approach, termed as beam-based, is developed for synthesizing CPMs in positioning systems. The proposed method is able to synthesize multi-DOF CPMs with both the stiffness and dynamic properties being governed during the optimization process. To overcome the drawback of existing methods in synthesizing multi-DOF CPMs, the stiffness optimization process is enhanced by using a new objective function with a well-defined unit. The objective function is based on a novel analytical approach which can normalize different units of components in the stiffness matrix of CPMs, e.g., N/m or Nm/rad, etc. Subsequently, the dynamic response of CPMs is improved to the targeted frequency while the optimized stiffness property is maintained through the dynamic optimization process.

To verify the effectiveness of the proposed method, it is used to synthesize a 3-DOF spatial-motion ($\theta_X - \theta_Y - Z$) CPM with optimized stiffness characteristics and targeted dynamic behavior. A working prototype of the synthesized CPM is developed, and experiments are carried out to evaluate the actual performance of the prototype. Lastly, some comparisons between the experimental results and the predicted data are conducted to validate the beam-based method.

3.2 Principle

In the beam-based method, the common 3-legged configuration is used to model CPMs. A typical CPM consists of a solid moving-platform (end effector) connected to three symmetric compliant limbs about the platform's center as illustrated in Figure 3.1. The limbs are considered as frictionless support bearings which elastic deformations generate output motions at the end effector. Here, the design space of each limb is a cube with one end being fixed to the ground while the other end is rigidly connected to the end effector. Each compliant limb is constructed by a pair of novel curved-and-twisted (C-T) beams as shown in Figure 3.2. The geometry of C-T beams can be optimized within the design space in order to generate various multi-DOF at the end effector.
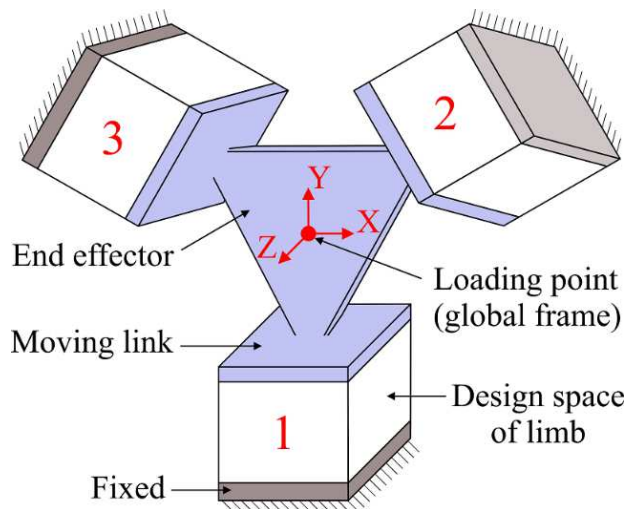
Figure 3.1: Model of CPM used in beam-based method.

Here, the C-T beams are proposed to produce spatial motions for multi-DOF CPMs. A Bezier curve defined by four control points is used to create the curved profile while the twist property is determined by the orientations at two ends of the C-T beam. With this special geometry, a general C-T beam is able to generate up to 6 DOF at its free end that can satisfy various requirements of multi-DOF CPMs.

45

An important merit of the C-T beam is that it can change into any form of flexure, from traditional straight beam-like shape to many complex geometries, to produce the desired output motions at the end effector. As illustrated in Figure 3.2a, a C-T beam can become a straight-and-flat flexure when all control points of the Bezier curve locate on a line with the difference between the twist angles at both ends being zero. Figure 3.2b represents the structure of a compliant limb in the CPM. With the local frame $X'Y'Z'$ of the limb being attached at the center of its free end, the design domain of a limb is modeled by a pair of symmetrical C-T beams about the $Y'Z'$ ($X' = 0$) plane. The Bezier center-curves are first defined based on the coordinates of their control points and then the C-T beams are created by sweeping a thin rectangular cross-sectional area through these curves. The twist property of a C-T beam is defined by the start and end twist angles (α_A and α_B respectively) at two end points of the Bezier curve as shown in Figure 3.2a. Here, the twist angle at a specific point along the beam is determined based on the local frame $X''Y''Z''$ located that position. In particular, the Z'' axis of the local frame is coincident with the tangent vector of the Bezier curve at that point while the X'' axis is defined by the projection of the global X axis onto the local $X''Y''$ plane. The twist angle at a specific point is measured from the corresponding X'' axis to the long edge of the rectangular cross-sectional area.
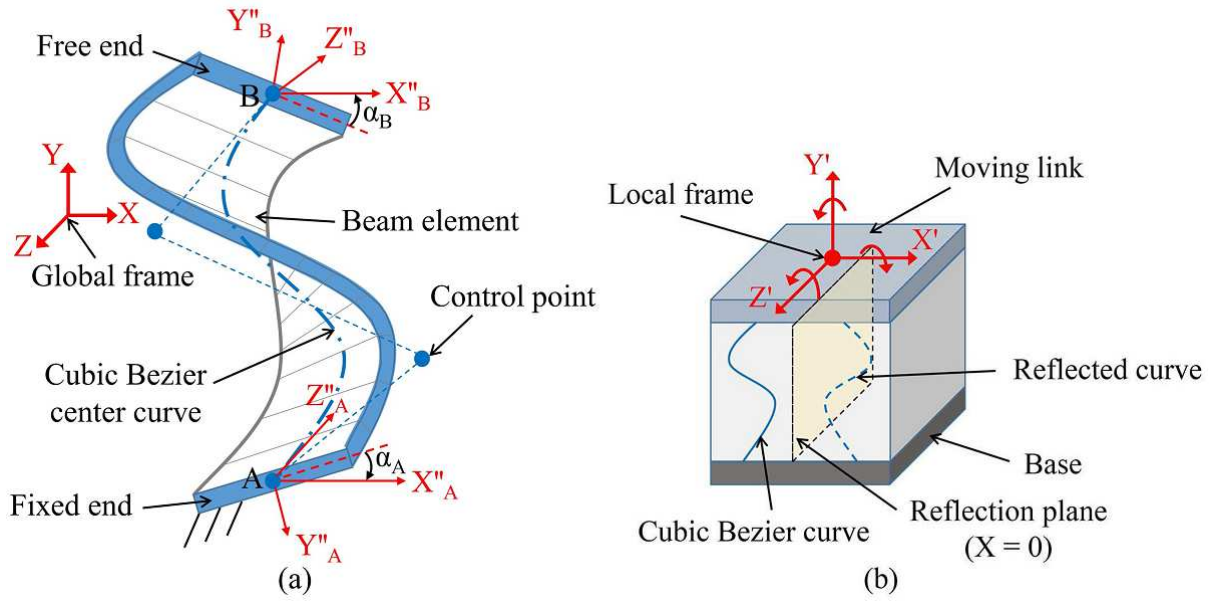
Figure 3.2: Structure of (a) C-T beam and (b) compliant limb.

The synthesis flow of the proposed beam-based method is shown in Figure 3.3. First, the desired DOF together with the general specifications for modeling the CPM, such as boundary dimensions of the design space and initial cross-sectional area of the C-T beams, must be specified. The geometrical design variables that determine structure of compliant limbs are then be defined. This is followed by the stiffness optimization process to find the optimal value of the stiffness objective function, f, as expressed in Eq. (3.10). The structure of C-T beams in each limb as well as the overall structure of the entire CPM are obtained after the stiffness optimization process. To achieve the targeted dynamic behavior, the dynamic optimization process for determining the mass distribution within the CPM is carried out to find the optimal size and shape of the C-T beams and the end effector. The dynamic optimization can be done by solving the dynamic objective function formulated by two sub-equations as expressed in Eq. (3.13). Lastly, based on the results obtained from the dynamic optimization process, the final design the CPM is able to achieve the desired DOF with optimized stiffness performance and targeted dynamic response.
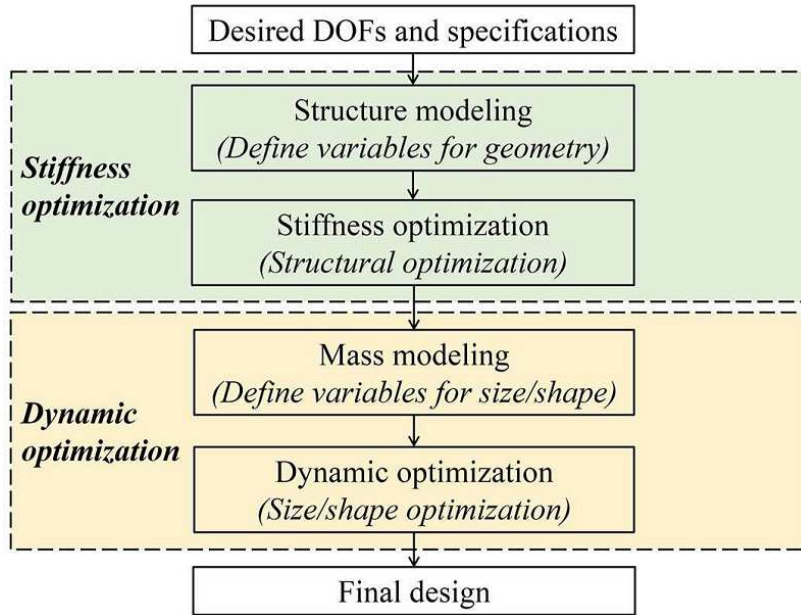
Figure 3.3: Flow of the beam-based method.

3.3 Stiffness Modeling

The aim of the stiffness optimization process in the beam-based method is to find the structure of C-T beams so that the CPM can achieve the highest stiffness ratio. With the three limbs within the CPM being symmetrical and identical, the overall design of the entire CPM can be defined based on the structure of one C-T beam. The stiffness property of CPM is analyzed by FEA with C-T beams being meshed by a number of 2-node beam elements. Fourteen parameters represent the geometry of a C-T beam as illustrated in Figure 3.2a are used as the design variables for the stiffness optimization. The curved profile of the beam is defined by twelve design variables represents the coordinates (x_i, y_i, z_i) of four control points ($i = 1,\ldots,4$) of the Bezier curve while the twist property is determined by the other two variables, which are the twist angles at the start and end points (α_A and α_B respectively) of the C-T beam. Here, the twist angle of the C-T beam is assumed to change linearly through its length.

48

Let K^{beam} be the 12×12 stiffness matrix of a 2-node beam element. If the total number of elements in the CPM is n, then the $s \times s$ global stiffness matrix of the entire CPM, K^s, is given as

$$K^s = \sum_{q=1}^{n} K_q^{\text{beam}} \tag{3.1}$$

where s denotes the dimension of K^s.

As discussed, a well-defined objective function is essential for the stiffness optimization process. Referring to previous works on the mutual potential energy [1], the characteristic stiffness [65] and the stiffness ratio [74], the objective function can be formulated by energies (works done) of the external loads. Here, the CPM is considered under effect of a general load vector, P, that contains three forces F_X, F_Y, F_Z components along, and three moments M_X, M_Y, M_Z components about the X, Y and Z axes respectively. Note that the loading point is at the center of the end effector as illustrated in Figure 3.1. Under the presence of P, six corresponding displacements (Δ_x, Δ_y, Δ_z, θ_x, θ_y, θ_z) at the loading point as shown in Figure 3.4 are represented by the displacement vector, U.
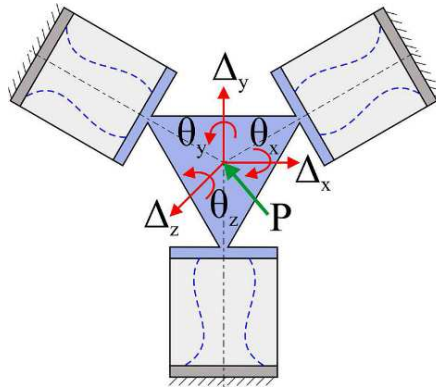
Figure 3.4: Corresponding displacements of the CPM under a general load.

The 6×6 stiffness matrix, K, that represents the stiffness property of the CPM can be obtained by the condensation of K^s [65], expressed as

$$K = K^s_{[6\times6]} - K^s_{[6\times(s-6)]} \cdot \left(K^s_{[(s-6)\times(s-6)]} \right)^{-1} \cdot K^s_{[(s-6)\times6]} \tag{3.2}$$

where $[a \times b]$ represents the dimension of matrix (a denotes the row and b denotes the column). Eq. (3.2) is derived based on the equilibrium equation of the CPM, given as

$$\underbrace{\begin{bmatrix} K^s_{[(s-6)\times(s-6)]} & K^s_{[(s-6)\times6]} \\ K^s_{[6\times(s-6)]} & K^s_{[6\times6]} \end{bmatrix}}_{K^s_{[s\times s]}} \cdot \underbrace{\left\{ \begin{matrix} U'_{[(s-6)\times1]} \\ U_{[6\times1]} \end{matrix} \right\}}_{U^s_{[s\times1]}} = \underbrace{\left\{ \begin{matrix} 0 \\ P_{[6\times1]} \end{matrix} \right\}}_{P^s_{[s\times1]}} \tag{3.3}$$

where U^s and P^s are vectors consist of s components, which represent the displacements and loads over the entire CPM. As the CPM is only subjected to point loading, P; U^s and P^s are separated into two parts where U' indicates the displacements of the nodes under the zero load and U indicates six corresponding displacements at the loading point subjected to P. Similarly, K^s is also partitioned into four corresponding parts as expressed in Eq. (3.3).

Based on the equilibrium equation, the relationship of U and P is re-expressed as

$$KU = P \tag{3.4}$$

Assuming that $D = \{1, 2, \ldots, 6\}$ is the set of six possible motions of the CPM, those motions are represented by the members of D where 1, 2, 3 represent three translational motions along; and 4, 5, 6 represent three rotational motions about the X, Y and Z axes respectively. Let N be the set of desired motions and M be the set of undesired motions of the CPM, N and M are the subsets of D and $N \cup M = D$. If the number of elements within

N and M are η and μ respectively, the relationship of η and μ with the six possible motions is given as

$$\eta + \mu = 6 \tag{3.5}$$

Let P_i and U_i indicate the loads and displacements in the desired motions, P_j and U_j indicate the loads and displacements in the undesired motions of the CPM where i and j denote the members in N and M respectively. Based on Eq. (3.4), the desired work done, W_i, and the undesired work done, W_j, are written as

$$W_i = \int_0^{P_i} U_i dP_i = \int_0^{P_i} \frac{P_i}{K_i} dP_i = \frac{1}{2}\frac{P_i^2}{K_i} \tag{3.6}$$

$$W_j = \int_0^{P_j} U_j dP_j = \int_0^{P_j} \frac{P_j}{K_j} dP_j = \frac{1}{2}\frac{P_j^2}{K_j} \tag{3.7}$$

where K_i (or K_j) denotes the ith (or j^{th}) component along the diagonal of K.

Here, the ratio between an individual desired work done and the product of all undesired works done is used to represent the flexibility of the entire CPM in a specific DOF. In particular, the ratio of the work done in the ith DOF, R_i, and the product of all undesired works done is expressed as

$$R_i = \prod_{j=1}^{\mu} \frac{W_{N_i}}{W_{M_j}} = \frac{W_{N_i}^{\mu}}{\prod_{j=1}^{\mu} W_{M_j}} \tag{3.8}$$

where N_i and M_j indicate the ith and j^{th} components in N and M respectively. When considering all the desired DOF, the total work done ratio, R, is given as

$$R = \prod_{i=1}^{\eta} R_i = \prod_{i=1}^{\eta} \frac{W_{N_i}^{\mu}}{\prod_{j=1}^{\mu} W_{M_j}} = \frac{\prod_{i=1}^{\eta} W_{N_i}^{\mu}}{\prod_{j=1}^{\mu} W_{M_j}^{\eta}} \tag{3.9}$$

The objective function, f, can be achieved by substituting Eqs. (3.6) and (3.7) to Eq. (3.9). The minimum value of f gives the best stiffness performance of the CPM, written as

$$\text{minimize} \quad f = \frac{1}{R} = \frac{\prod_{j=1}^{\mu} \left(\frac{1}{2} \frac{P_{M_j}^2}{K_{M_j}} \right)^{\eta}}{\prod_{i=1}^{\eta} \left(\frac{1}{2} \frac{P_{N_i}^2}{K_{N_i}} \right)^{\mu}} = \kappa \cdot \frac{\prod_{j=1}^{\mu} K_{M_j}^{-\eta}}{\prod_{i=1}^{\eta} K_{N_i}^{-\mu}}, \tag{3.10}$$

$$\text{where} \quad \kappa = \frac{\prod_{j=1}^{\mu} P_{M_j}^{2\eta}}{\prod_{i=1}^{\eta} P_{N_i}^{2\mu}}$$

Note that f is formulated by the ratio of energy so it is dimensionless. In Eq. (3.10), κ is a coefficient factor. In case P is the unit load, $\kappa = 1$ because values of all loads (P_{N_i} and P_{M_j}) are equal to 1 and f represents the product of stiffness ratios. The proposed objective function can be used to maximize the flexibility of the CPM in the desired DOF by minimizing the actuating stiffness, and to constrain motions in undesired directions by maximizing the non-actuating stiffness. The unit issue is solved by using the ratio of energy so that this function is useful for synthesizing any case of CPM.

3.4 Dynamic Modeling

The purpose of the dynamic optimization process is to improve the dynamic response of the CPM, i.e. the first resonant mode, to the targeted frequency. This can be done by

determining the cross-sectional area of the C-T beams and the material distribution within the CPM. Figure 3.5 shows eight design variables used to represent the size and shape of the C-T beam and the end effector of the CPM for the dynamic optimization process. Among them, two variables (b_1, h_1) represent the cross-sectional area of the C-T beam, two variables (b_2, h_2) determine the cross-sectional area of the additional mass, two variables (p, l) define the position and the length of the additional mass, and the last two variables (r, t) represent the size and mass of the end effector.
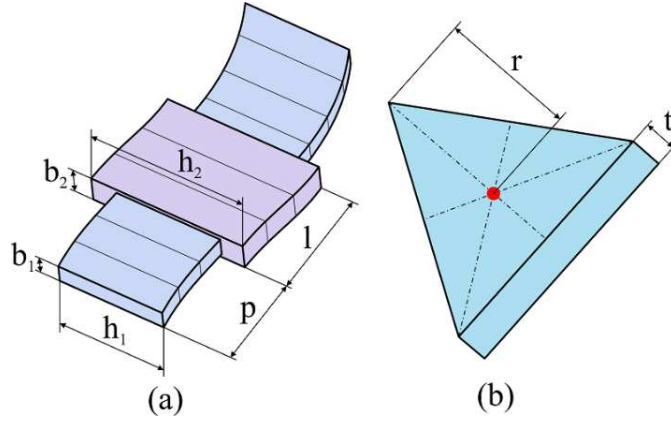
Figure 3.5: Design variables of the dynamic optimization process defined by (a) the C-T beam and (b) the end effector.

Let M^{beam} be the 12×12 mass matrix of each beam element, the $s \times s$ global mass matrix of a CPM, M^s, is written as

$$M^s = \sum_{q=1}^{n} M_q^{\text{beam}} \tag{3.11}$$

The relationship of the bandwidth vector, ω, and the natural frequency vector, F, of the CPM is expressed as

$$F_{[s \times 1]} = \frac{\omega_{[s \times 1]}}{2\pi}, \quad \text{where} \left| -\omega^2 \cdot M_{[s \times s]}^s + K_{[s \times s]}^s \right| = 0 \tag{3.12}$$

In Eq. (3.12), the full-rank mass and stiffness matrices are used to formulate the dynamic problem so that any vibration mode of the CPM can be extracted. Here, the first resonant frequency of the entire CPM is represented by F_1, which is the component having the smallest value in F.

A common problem in synthesizing dynamic property of compliant systems is that the dynamic response can be improved by an increase in the stiffness. As a result, it is a challenge to strike a balance between the stiffness and dynamic characteristics of a CPM. In the beam-based method, the objective of the dynamic optimization process is represented by a set of two equations as shown in Eq. (3.13) in order to find an optimal structure for the CPM that can maintain optimal stiffness property and achieve desired dynamic response.

$$\begin{cases} \text{minimize} \ \left(\left| F_d - F_1 \right| \right) \\ \text{minimize} \ \left(f \right) \end{cases} \tag{3.13}$$

Here, F_d is the targeted frequency response. The aim of the dynamic optimization is to find the optimal mass distribution within the CPM in order to enhance the first resonance mode to the desired value ($F_1 = F_d$) defined by the first equation while the stiffness property is kept as high as possible through the second equation.

3.5 Synthesis and Evaluation of a 3-DOF Spatial-Motion $(\theta_X - \theta_Y - Z)$ CPM

3.5.1 Problem formulation

The proposed beam-based method is employed to synthesize a 3-DOF spatial-motion $(\theta_X - \theta_Y - Z)$ CPM. The synthesized CPM is desired to have low actuating stiffness to achieve a large workspace under small actuating forces. Moreover, the stiffness ratios between the non-

actuating stiffness and actuating stiffness need to be large to resist against the external disturbances. To satisfy the requirement of positioning applications, the dynamic response of the CPM must be fast. Here, the first resonant mode of the CPM is targeted to be 100 Hz. The material used to build the CPM is Al7075-T6, which has a Young's modulus of 71.7 GPa, Poisson ratio of 0.33, density of 2.81 g/cm^3 and yield strength of 503 MPa. The design space of each compliant limb is assigned as $50 \times 50 \times 50$ mm^3.

3.5.2 Stiffness optimization

Referring to Section 3.3, the desired 3 DOF are θ_X, θ_Y, Δ_Z and thus directly correspond to the 4th, 5th and 3rd diagonal components within the stiffness matrix of the CPM. With the number of DOF being assigned as 3, $N = \{4,5,3\}$ ($\eta = 3$) represents the desired motions of θ_X, θ_Y and Δ_Z while $M = \{1,2,6\}$ ($\mu = 3$) represents the undesired motions of Δ_X, Δ_Y, and θ_Z. Note that $\eta + \mu = 6$ satisfies Eq. (3.5). By using Eq. (3.6), the desired works done, i.e., W_4 about the X axis, W_5 about the Y axis, and W_3 along the Z axis, are defined and expressed as

$$W_4 = \frac{1}{2}\frac{M_X^2}{K_{\theta_X}}, \quad W_5 = \frac{1}{2}\frac{M_Y^2}{K_{\theta_Y}}, \quad W_3 = \frac{1}{2}\frac{F_Z^2}{K_{\Delta_Z}} \qquad (3.14)$$

Similarly, by using Eq. (3.7), the undesired works done, i.e., W_1 along the X axis, W_2 along the Y axis, W_6 about the Z axis are defined and written as

$$W_1 = \frac{1}{2}\frac{F_X^2}{K_{\Delta_X}}, \quad W_2 = \frac{1}{2}\frac{F_Y^2}{K_{\Delta_Y}}, \quad W_6 = \frac{1}{2}\frac{M_Z^2}{K_{\theta_Z}} \qquad (3.15)$$

Applying Eq. (3.10), the objective function, f, is derived as

$$\text{minimize } f = \kappa \cdot \frac{K_{\theta_X}^3 K_{\theta_Y}^3 K_{\Delta_Z}^3}{K_{\Delta_X}^3 K_{\Delta_Y}^3 K_{\theta_Z}^3}, \quad \text{where } \kappa = \frac{F_X^6 F_Y^6 M_Z^6}{M_X^6 M_Y^6 F_Z^6} \tag{3.16}$$

Considering P as a unit wrench with $\kappa = 1$, Eq. (3.16) can be simplified as

$$\text{minimize } f = \frac{K_{\theta_X}^3 K_{\theta_Y}^3 K_{\Delta_Z}^3}{K_{\Delta_X}^3 K_{\Delta_Y}^3 K_{\theta_Z}^3} \tag{3.17}$$

Twelve design variables are defined for the stiffness optimization process as shown in Figure 3.2a. The stiffness optimization is carried out using the GA solver of Matlab to solve the objective function expressed in Eq. (3.17). In this research, GA is chosen because it has been successfully used in many existing optimization methods, such as ESO/BESO, morphological representation and mechanism integrated methods. Basically, the GA solver manages the optimization problem defined by an objective function (can be single- or multiple-objective function), design variables and constraints. The optimal result is found via the natural selection of biological evolution. Firstly, a population of many individuals is randomly created for the first generation. Subsequently, the best individuals from the current generation are selected as parents to create children for the next generation. After a number of generations, the population evolves and the best individual (optimal result) that satisfies the optimization requirement (defined by the objective function and constraints) is obtained.

The structure of one compliant limb obtained after the stiffness optimization process is illustrated in Figure 3.6a. It is observed that the C-T beams became straight flexures with zero twist angle. At this stage of the research, two reflecting C-T beams are constrained to have no intersection between each other to eliminate any undesired computational error that could occur during the synthesis process. In this design, two C-T beams are separated by a gap of 1 mm. Based on the optimized design variables of the stiffness optimization process, the 3D structure

of the CPM is modeled and shown in Figure 3.6b. The compliant matrix of this CPM, $C_s^{\text{3-DOF}}$, is expressed as

$$
C_s^{\text{3-DOF}} = \begin{bmatrix}
1.45e-7 & & & & & \\
0 & 1.45e-7 & & & SYM & \\
0 & 0 & 1.28e-3 & & & \\
-1.61e-5 & 0 & 0 & 2.07e-1 & & \\
0 & -1.61e-5 & 0 & 0 & 2.07e-1 & \\
0 & 0 & 9.53e-6 & 0 & 0 & 4.63e-4
\end{bmatrix} \tag{3.18}
$$
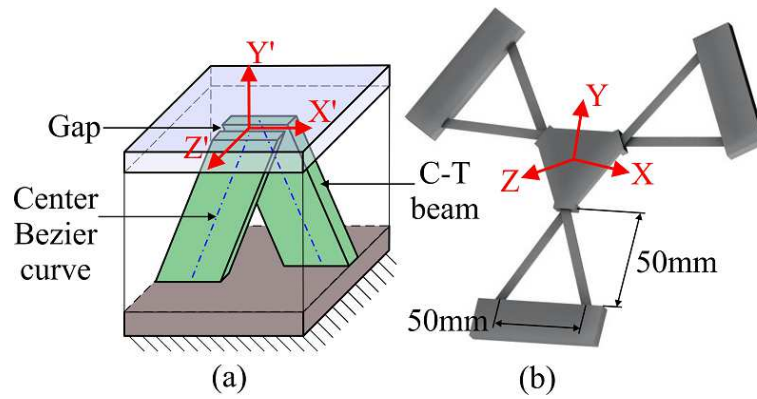
Figure 3.6: Structure of (a) one compliant limb and (b) the entire CPM after the stiffness optimization process.

3.5.3 Dynamic optimization

After the stiffness optimization, the dynamic optimization process is conducted to further optimize the mass distribution within the synthesized CPM illustrated in Figure 3.6b based on a targeted natural frequency of 100 Hz. The multi-objectives optimization GA solver of Matlab is used to solve the dynamic optimization problem. Here, the eight design variables of the dynamic optimization process shown in Figure 3.5 are optimized by solving the objective function defined by two equations as expressed in Eq. (3.13) with the value of F_d being substituted by 100. After the natural selection of GA, the final design of the CPM modeled based on the obtained results of the dynamic optimization process is shown in Figure 3.7a. It is observed that the size of the C-T beams and the end effector are optimized, some additional

57

masses are also added along the C-T beams. With the optimized mass distribution found after the dynamic optimization process, the synthesized CPM is able to produce the desired dynamic response of 100 Hz. FEA is used to verify the correctness of the optimized results. Figure 3.7b illustrates the first resonance mode of the CPM simulated using ANSYS. The simulation result shows that the resonance occurs at 100.354 Hz. From the overall deformation of the CPM and the values of displacement given in the color bar, it is seen that the CPM deforms along the Z axis with the increasing displacement from the legs (represented by the blue color) to the end effector (represented by the red color). This result demonstrates that the first vibration mode of the CPM is along the Z axis and well matches the optimization data. After the dynamic optimization process, the compliant matrix of the optimized CPM becomes

$$C_d^{\text{3-DOF}} = \begin{bmatrix} 5.91e-8 & & & & & \\ 0 & 5.91e-8 & & & SYM & \\ 0 & 0 & 2.59e-4 & & & \\ -6.49e-6 & 1.32e-7 & 0 & 6.78e-2 & & \\ -1.32e-7 & -6.49e-6 & 0 & 0 & 6.78e-2 & \\ 0 & 0 & 6.46e-6 & 0 & -1.5e-14 & 2.54e-4 \end{bmatrix} \quad (3.19)$$
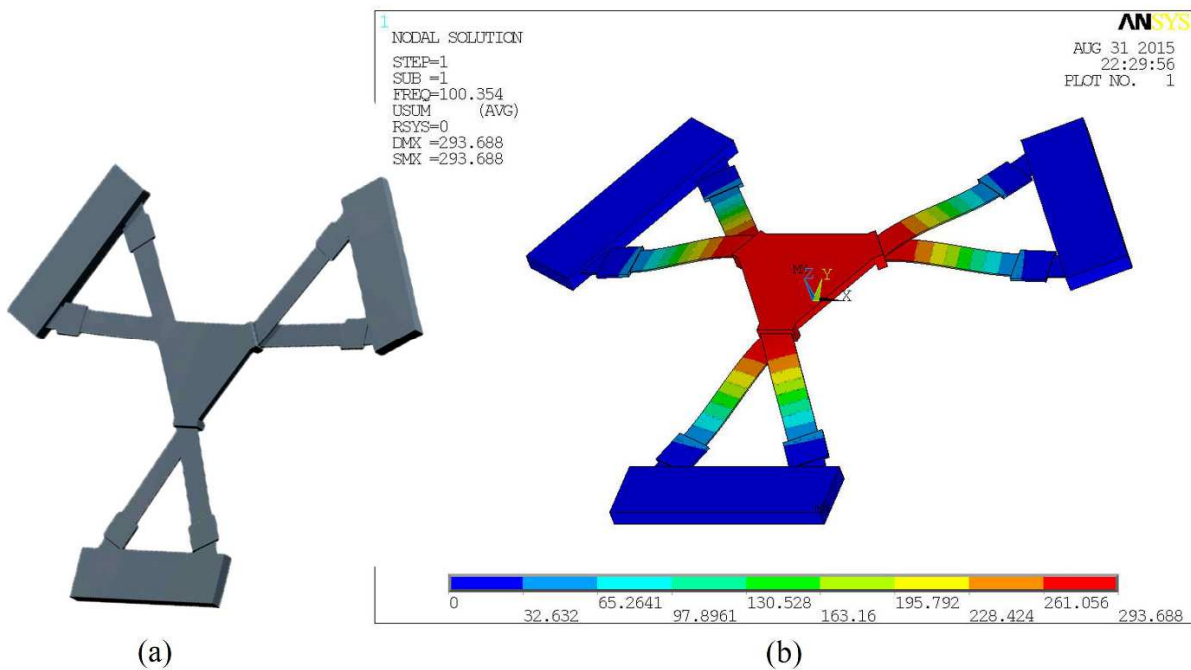
Figure 3.7: (a) Synthesized CPM and (b) the first resonant mode simulated via ANSYS.

Eq. (3.19) suggests the synthesized CPM has good motion decoupling since the off-axis components are much smaller than the diagonal components. However, its motion property is still coupled. In addition, the two stiffness ratios of the CPM can be calculated by taking the ratios of the corresponding compliance as given in the following

$$
\begin{aligned}
\frac{K_{\Delta_X}^{\text{3-DOF}}}{K_{\Delta_Z}^{\text{3-DOF}}} = \frac{K_{\Delta_Y}^{\text{3-DOF}}}{K_{\Delta_Z}^{\text{3-DOF}}} = \frac{C_{\Delta_Z}^{\text{3-DOF}}}{C_{\Delta_X}^{\text{3-DOF}}} = \frac{C_{\Delta_Z}^{\text{3-DOF}}}{C_{\Delta_Y}^{\text{3-DOF}}} = 4382 \\
\frac{K_{\theta_Z}^{\text{3-DOF}}}{K_{\theta_X}^{\text{3-DOF}}} = \frac{K_{\theta_Z}^{\text{3-DOF}}}{K_{\theta_Y}^{\text{3-DOF}}} = \frac{C_{\theta_X}^{\text{3-DOF}}}{C_{\theta_Z}^{\text{3-DOF}}} = \frac{C_{\theta_Y}^{\text{3-DOF}}}{C_{\theta_Z}^{\text{3-DOF}}} = 267
\end{aligned}
\tag{3.20}
$$

Numerical simulation via ANSYS is used to analyze the workspace of the CPM with the yield strength of 503 MPa as the limit. The simulation results show that the synthesized CPM can offer a large workspace of $\pm 4° \times \pm 4° \times \pm 2.75$ mm. Referring to Eq. (3.20) and [74], it is seen that the stiffness ratios of the synthesized CPM are very high for a large workspace CPM. In summary, the 3-DOF CPM synthesized by the proposed beam-based structural optimization method is able to achieve large workspace, optimized stiffness property and targeted dynamic behavior.

3.5.4 Experimental investigations and results

A prototype is built to validate the proposed synthesis method. As the final design of the synthesized 3-DOF CPM has a complex structure with thin flexures and solid blocks, it requires some post-processing before fabrication. The post-process is to separate the CPM into many sub-parts for fabrication via CNC milling method before assembling them into a complete prototype. In addition, the end effector needs to be made larger to accommodate for external actuation as shown in Figure 3.8. The optimized mass of the end effector is maintained by making it thinner and several supported ribs are added for rigidity.
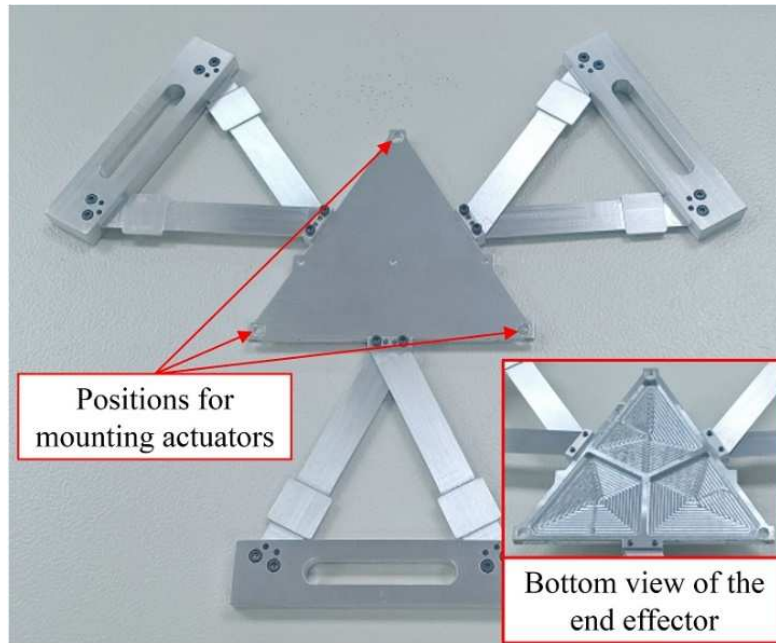
Figure 3.8: Prototype of the synthesized CPM fabricated by milling method.

The experiments are carried out to determine the stiffness characteristics of the prototype over the full workspace of $\pm 4° \times \pm 4° \times \pm 2.75$ mm by measuring the actuating forces and displacements at many different positions and repeated five times.

a) *Translational compliance*

The experimental setup for evaluating the compliance along the Z axis is shown in Figure 3.9. A 10μm-resolution micrometer is used to provide input displacement along the Z axis while a 6-axes force/torque (F/T) sensor (ATI, MINI-40) is attached to the micrometer to measure the actuating force concurrently. Furthermore, a rigid rod with a sharp tip is used to apply the input force on the end effector of the CPM at its center. For the translational compliance, the predicted and FEA values are 2.59×10^{-4} m/N and 2.25×10^{-4} m/N respectively as shown in Figure 3.10.

60
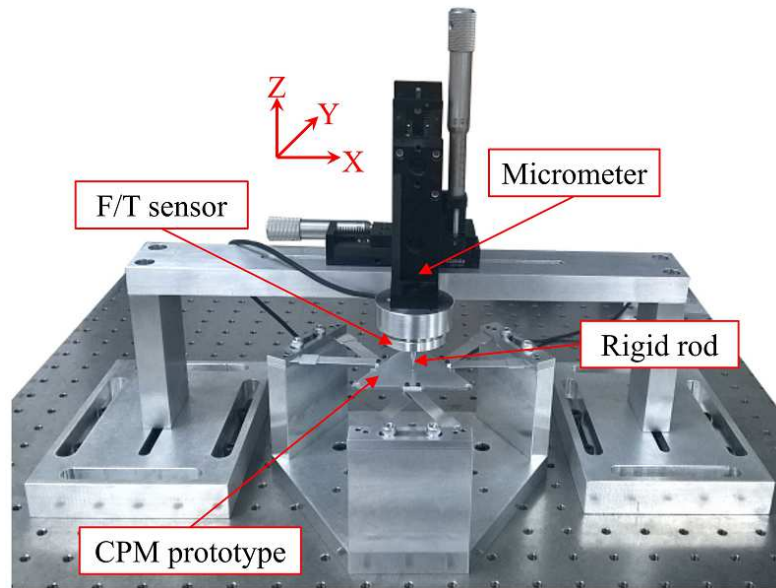
Figure 3.9: Experimental setup for evaluating the compliance along the *Z* axis.
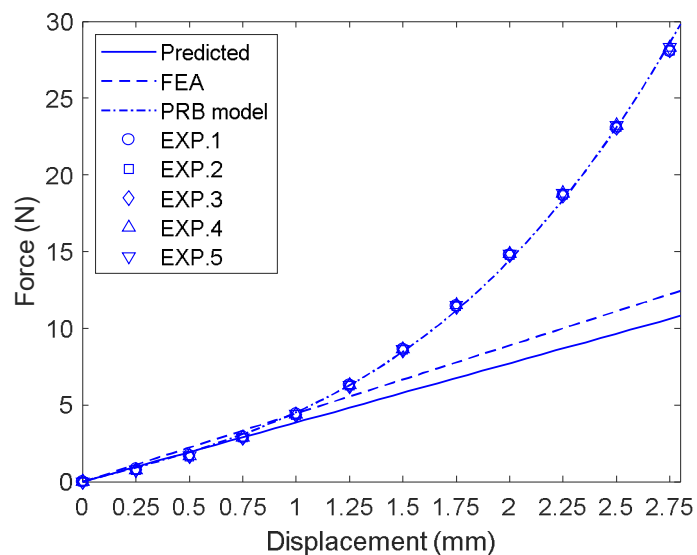
Figure 3.10: Compliance along the *Z* axis with the experimental results plotted against the predicted, FEA and PRB model.

It is observed that the results of the beam-based method and FEA are meant for small displacement. In particular, the deviation between the experiments and the predicted as well as FEA results is small (<10%) within the range from 0 to 1 mm. The experimental compliance from 1 mm onwards becomes nonlinear and the deviation is larger due to the over-constrained structure of the CPM. However, the nonlinear portion agrees well with the equivalent PRB model [11], which is represented in Appendix A , with an average deviation of 4.2%.

Consequently, suitable equivalent models are helpful for predicting the nonlinear compliance behaviors of the over-constrained CPMs over large displacement.

b) *Rotational compliance*

Figure 3.11 shows the experimental setup for evaluating the rotational compliance about the X axis. A two-point support is placed below the moving platform to constrain the unwanted translational motion along the Z axis so that the end-effector can deliver pure rotational motion about the X axis. Similar concept is adopted when evaluating the rotational compliance about the Y axis. The actuating force and displacement are applied and measured at one point respectively to calculate the bending moment as well as the rotation angle. To ensure a pure rotation is produced for each measurement, a digital gauge is used to measure the linear displacement at the opposite position; making sure it is similar to the input displacement from the micrometer. For the rotational compliance about the X and Y axes, the predicted and FEA values are 6.78×10^{-2} rad/Nm and 7.65×10^{-2} rad/Nm respectively as shown in Figure 3.12 and Figure 3.13.
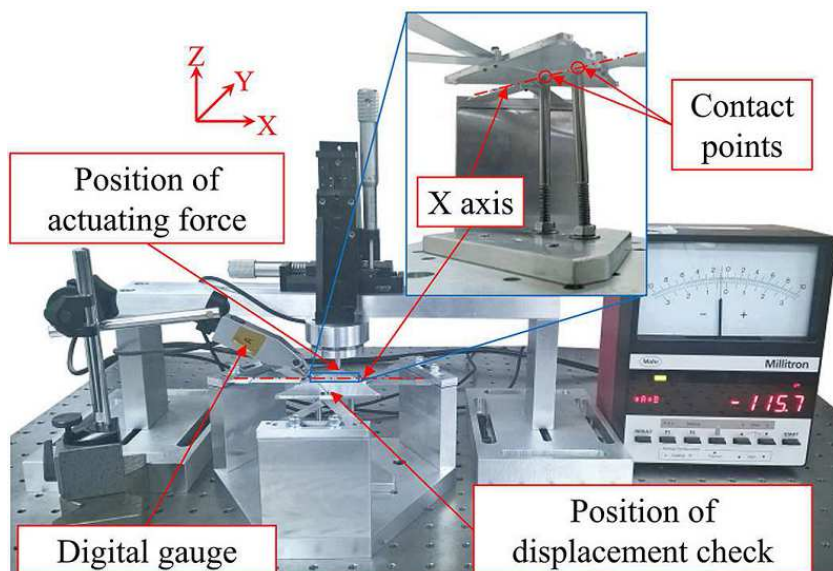
Figure 3.11: Experimental setup for evaluating the compliance about the X axis.
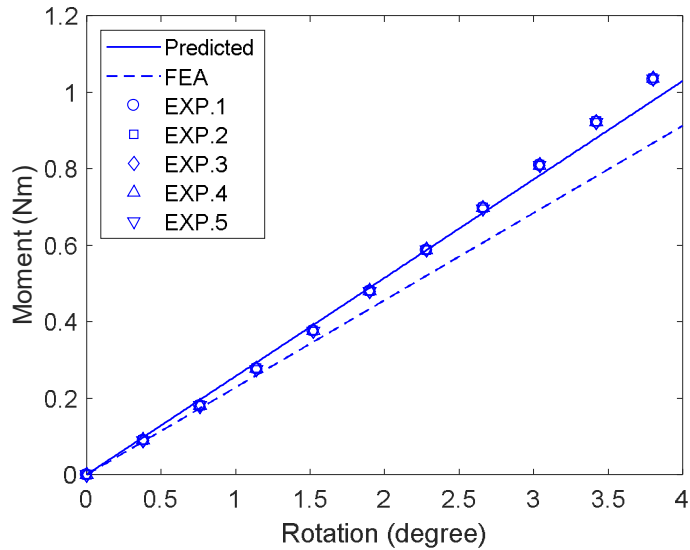
Figure 3.12: Experimental result compared to predicted and FEA compliance about the *X* axis.
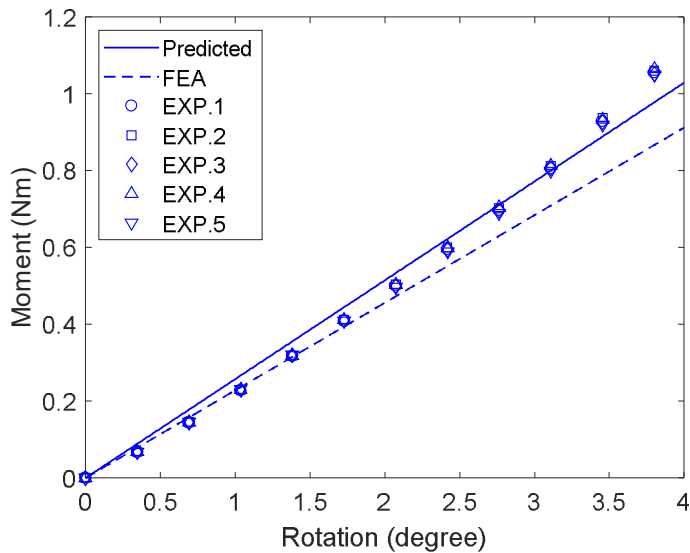
Figure 3.13: Experimental result compared to predicted and FEA compliance about the *Y* axis.

Referring to Figure 3.12 and Figure 3.13, the nonlinear characteristic is less significant for the rotational compliance as compared to the translational compliance, which is significantly affected by the over-constrained design. For the experimental compliance about the *X* and *Y* axes, the average deviations of the measured values compared to the predicted results are 3.9% and 8.2% respectively while the deviations compared to FEA results are 15.7% and 11.9% respectively. It is seen that for all actuating compliance, the deviations between the predicted and experimental results are lower as compared to the deviations between the FEA

63

and experimental results. It is because the FEA results obtained from ANSYS are analyzed via 10-node tetrahedral structural solid elements while the predicted results calculated via Matlab are based on 2-node beam elements. Since the beam-based method synthesizes CPMs based on the novel C-T beams, the FEA using beam elements can well approximate the specific geometry of such beam-type flexures and hence, more accurate results can be achieved.

c) *Dynamic behavior*

The experimental setup for measuring the frequency response of the prototype is shown in Figure 3.14. As the first resonance mode of the CPM is the vibration along the Z axis, a single-axis accelerometer (PCB PIEZOTRONICS 353B15) is attached below the end effector to measure the acceleration along the Z axis while the excitation along the same direction is generated by an impact hammer (PCB PIEZOTRONICS 086C03). The obtained data is then acquired by a signal acquisition module (DATA TRANSLATION DT9837) and analyzed by the Dewe-FRF 6.6 software.
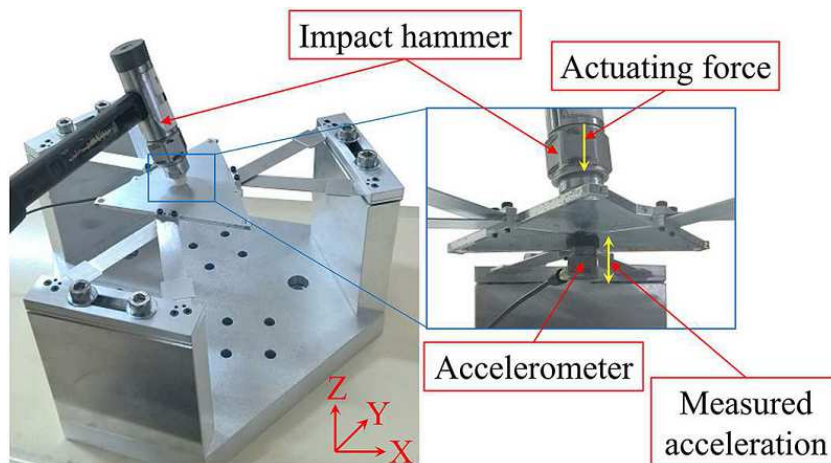
Figure 3.14: Experimental setup for measuring dynamic response of the CPM.

Figure 3.15 demonstrates the dynamic response of the CPM generated by the analysis software. It is observed that the first resonant frequency of the CPM is recorded as 84.4 Hz, which is 15.6% lower than the desired value of 100 Hz. Such variation can be due to the manufacturing/assembly errors. In particular, the parts fabricated by CNC machining have the

manufacturing tolerance of approximately ± 0.02 mm, and some unpredictable errors during the assembly process, e.g., inaccurate positions of parts and the additional masses of screws, also badly affect the actual performance of the prototype. Therefore, the 15.6% variation of the dynamic response is reasonable. Based on the results obtained from the numerical simulation (see Figure 3.7b) and the experimental investigation, the proposed synthesis method has proven to be able to predict the dynamic behavior of the CPM.
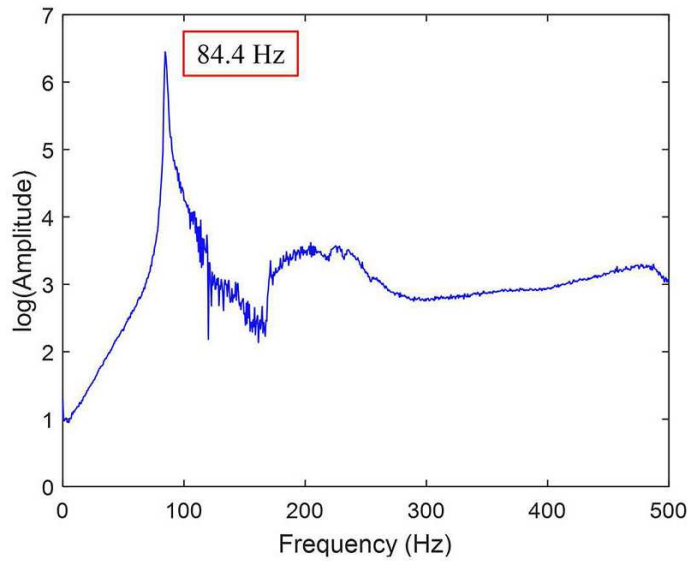
Figure 3.15: Experimental dynamic response of the CPM.

3.5.5 Discussion

Based on the experimental investigation, the synthesized 3-DOF ($\theta_X - \theta_Y - Z$) CPM achieves large motion range of ±4° × ±4° × ±2.75 mm with high dynamic response of 84.4 Hz. By comparing to an existing large-workspace 3-DOF ($\theta_X - \theta_Y - Z$) CPM [129], which demonstrated a motion range of ±2.5° × ±2.5° × ±2.5 mm and a dynamic response of ~15 Hz, the workspace and dynamic behavior of the synthesized CPM are significantly larger. One major challenge of developing CPMs with large workspace is to maintain high stiffness ratios. In another word, it is a challenge to synthesize a large-displacement CPM with high non-actuating stiffness. This is demonstrated by the low stiffness ratios of the 3-DOF ($\theta_X - \theta_Y - Z$)

CPM presented in [129] where the translational and rotational stiffness ratios are only less than 2. On the other hand, the translational and rotational stiffness ratios of the synthesized CPM are expected to reach more than 4000 and 200 respectively. More recently, another large-workspace 3-DOF ($X - Y - \theta_Z$) CPM with high translational stiffness ratio of about 130 has been developed [74]. By comparing against this 3-DOF planar-motion CPM, the synthesized CPM has better stiffness performance with much higher translational stiffness ratios, i.e., >4000. This is also mainly due to the analytical approach presented in Section 3.3 that normalizes the different units of components within the stiffness matrix, i.e., N/m or Nm/rad, to establish a well-defined objective function for the optimization process.

3.6 Summary

This chapter presents a novel method for synthesizing multi-DOF CPMs for positioning applications with optimized stiffness and dynamic properties. Termed as the beam-based structural optimization method, it generalizes a CPM that consists of an end effector with three symmetrical limbs defined by a cubic design space. Within the design space, the compliant limb is constructed by two reflecting novel C-T beams. The structure of the C-T beam will be first optimized via the stiffness optimization process, and the dynamic behavior of the CPM can then be improved to a targeted frequency through the dynamic optimization process. Consequently, the final CPM which is able to produce optimized stiffness property and the desired dynamic behavior can be achieved. Furthermore, a well-defined objective function for synthesizing multi-DOF CPMs is derived to normalize the different units, e.g., N/m or Nm/rad, etc., of components within the stiffness matrix. Importantly, this approach is applicable to any optimization method and it can be applied to derive objective function for any desired DOF.

To evaluate the effectiveness of the proposed method, it is used to synthesize a 3-DOF spatial-motion ($\theta_X - \theta_Y - Z$) CPM that delivers optimized stiffness characteristics with a desired

dynamic response of 100 Hz. The synthesized CPM with straight-and-flat flexures is obtained after the random optimization process based on GA. Starting from the very general and complex structure of the C-T beams, the resulting V-shape flexures are able to provide high stiffness ratios (>200 for rotations and >4000 for translations) as well as the largest workspace of ±4° × ±4° × ±2.75 mm. The obtained results demonstrate a special evolvement of the novel C-T beam due to the selected design example.

A physical prototype is built by CNC milling technology, and the experimental investigations demonstrate that the synthesized CPM is able to achieve the full workspace of ±4° × ±4° × ±2.75 mm and the first resonant mode of 84.4 Hz. Experimental results also show that the beam-based method can be properly used to predict the stiffness property of the CPM with a maximum deviation of less than 9% found between the predicted and measured values. The non-linear characteristic of the translational stiffness over large workspace due to the over-constrained structure can be well predicted by a suitable PRB model with a deviation of 4.2% compared to the experimental result. Lastly, the beam-based method is demonstrated to be able to predict the dynamic behavior of CPMs. The deviation of 15.6% between the actual and predicted natural frequencies is due to the assembly errors. However, the synthesized CPM fails to deliver decoupled motions due to the presence of five non-diagonal components within the stiffness matrix as shown in Eq. (3.19).

CHAPTER 4
INVESTIGATION ON THE MECHANICAL CHARACTERISTICS OF 3D-PRINTED CPM

4.1 3D-Printed Prototype of the Synthesized 3-DOF $(\theta_X - \theta_Y - Z)$ CPM

The performance of the prototype of the 3-DOF $(\theta_X - \theta_Y - Z)$ CPM built based on CNC machining is affected by assembly errors and the additional masses of the mounting parts (screws, nuts, etc.). This has been shown to cause the deviation of 15.6% of the dynamic property in the milled prototype. Therefore, to overcome the drawbacks of traditional machining methods, a 3D-printed prototype of the synthesized CPM is monolithically fabricated by EBM technology with Ti6Al4V material. The detailed printing process is described in Appendix B . Since 3D printing technology has not been popularly used to fabricate compliant devices, the mechanical characteristics of the 3D-printed CPM will be the focus of investigation here. In particular, a manipulator built based on the proposed CPM and its performance are experimentally tested to evaluate the suitability of using 3D-printed compliant mechanisms in precision systems.

The EBM-printed prototype shown in Figure 4.1 has the same design as the milled prototype shown in Figure 3.8. The material of the CPM has a Young's modulus of 111 GPa, Poisson ratio of 0.34, density of 4.5 g/cm^3 and yield limit of 950 MPa. Analytical results show that the 3D-printed prototype is able to obtain the first resonant frequency of 98 Hz and its stiffness matrix is represented by Eq. (4.1). Results from FEA suggest that the CPM can

achieve the workspace of $\pm 3° \times \pm 3° \times \pm 2$ mm. In addition, the 3D-printed CPM also provides similar motion property and high stiffness ratios as the milled prototype.

$$C'^{\text{3-DOF}} = \begin{bmatrix} 3.82e-8 & & & & & \\ 0 & 3.82e-8 & & & SYM & \\ 0 & 0 & 1.67e-4 & & & \\ -4.19e-6 & 8.52e-8 & 0 & 4.38e-2 & & \\ -8.52e-8 & -4.19e-6 & 0 & 0 & 4.82e-2 & \\ 0 & & 4.17e-6 & 0 & 0 & 1.64e-4 \end{bmatrix} \quad (4.1)$$
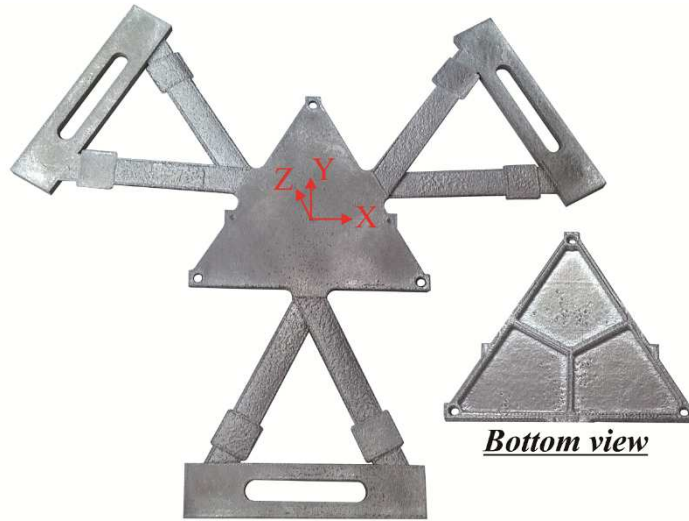
Figure 4.1: EBM-printed prototype of the 3-DOF CPM.

4.2 Effective Thickness of 3D-Printed Flexures

The 3D-printed prototype shown in Figure 4.1 is fabricated by EBM technology with the building direction being parallel to the Z axis of the design. The CPM has a number of thin features so that the dimensional accuracy of the prototype is verified with a caliper. The measured results show that for dimensions of ≥ 1 mm, the accuracy of the 3D-printed prototype is good. For thinner features, the measured thickness is always higher than the designed value, e.g., the measured thickness of the C-T beams is ~0.8 mm while the designed thickness is 0.49 mm.

After some experiments, the actual stiffness of the 3D-printed CPM is found in between the analysis results obtained for the thickness of C-T beams of 0.49 mm and 0.8 mm. This shows that the measured thickness of 0.8 mm is inaccurate due to the surface roughness of the printed prototype. Hence, it is necessary to determine the effective thickness of the 3D-printed C-T beams so that the performance of the CPM prototype can be evaluated accurately. Some preliminary experiments, using a traditional linear spring mechanism as the standard model, are carried out to explore the effective thickness of EBM-printed flexures.

A 0.5mm-thick linear spring mechanism as shown in Figure 4.2 is fabricated by EBM technology with the same material and building direction as the CPM prototype. The stiffness of the EBM-printed linear spring mechanism is then evaluated using the experimental setup shown in Figure 4.3. It is seen that a micrometer is used to create the input displacement and a 6-axes force/torque (F/T) sensor (ATI, MINI-40) is used to measure the actuating force. A force is applied to the flexures through a rod which is rigidly connected to the free end of the linear spring mechanism. Under the actuating force, the free end of the linear spring mechanism would be displaced along the horizontal direction, which is parallel to the input displacement from the micrometer. To ensure the accuracy of the measured force, a linear guide is used to eliminate the parasitic motion perpendicular to the main motion of the linear spring mechanism due to the elastic deformation of two parallel flexures.
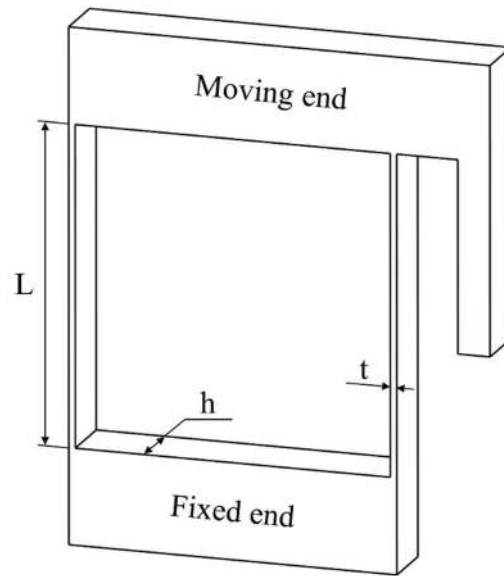
Figure 4.2: Drawing of the linear spring mechanism.
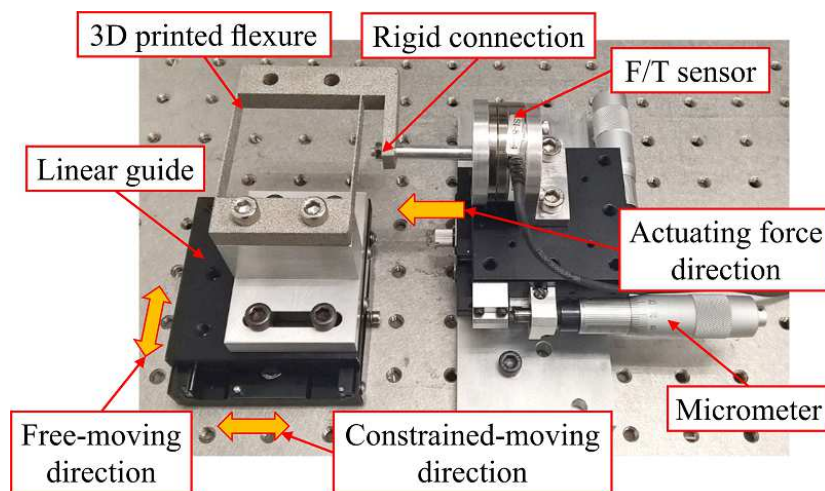
Figure 4.3: Experimental setup for measuring the stiffness of the EBM-printed linear spring mechanism.

The stiffness of the linear spring mechanism is obtained by measuring the actuating force caused by the input displacements from 0 to 2 mm in steps of 0.25 mm. Five measurements are conducted and the results of the measured forces against the input displacement are shown in Figure 4.4. The stiffness of the 3D-printed linear spring mechanism is found to be 4.55 N/mm. In theory, the translational stiffness of a linear spring mechanism is expressed as [33]

$$K_{ls} = \frac{24EI}{L^3} \qquad (4.2)$$

where K_{ls} is the translational stiffness of the linear spring mechanism, E is the Young's modulus of the material and $I = \dfrac{t^3 h}{12}$ is the moment of inertia of the flexure's cross-sectional area. Here, the designed width of the linear spring mechanism (h) is 10 mm, the thickness (t) and length (L) of two flexures are 0.5 mm and 50 mm respectively.
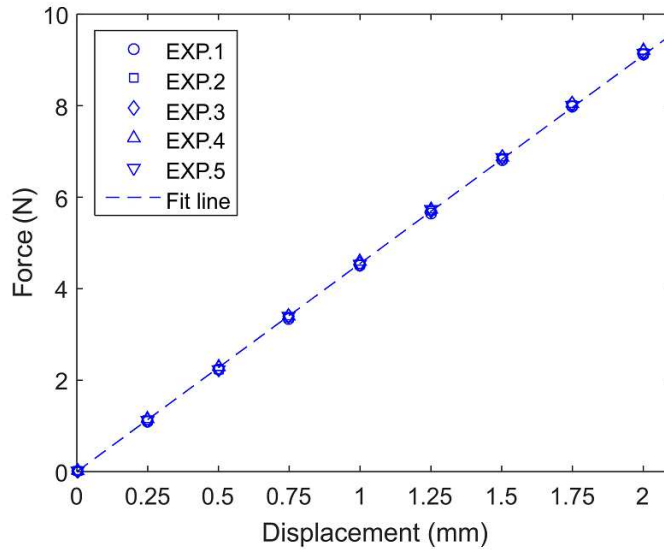
Figure 4.4: Measured stiffness of the EBM-printed linear spring mechanism.

Based on the measured stiffness of 4.55 N/mm and Eq. (4.2), the effective thickness of the 3D-printed flexures is determined to be 0.635 mm. Thus, a coefficient factor, λ, used to define the effective thickness of 3D-printed thin-flexures from the designed thickness can be calculated as

$$\lambda = \frac{t_e}{t_d} = \frac{0.635}{0.5} = 1.27 \qquad (4.3)$$

where t_e and t_d are the effective thickness and designed thickness of the flexures respectively. Note that the length and width of the flexures are assumed constant because their dimensions are much larger than 1 mm.

From the experiment, the effective thickness of 3D-printed flexures with thickness being 0.5 mm is found to be slightly higher than the designed one. In particular, the effective thickness of 0.5mm-thick flexure is 0.635 mm. The measured dimensions could be larger than the effective thickness due to rough surfaces of 3D-printed flexures. With the size of Ti6Al4V powder distributes in a range of 45-105 µm, the difference of ~0.165 mm between the measured and effective thicknesses of the C-T beams could be attributed to the semi-sintered material particles on the boundary surfaces. Note that the proposed value of λ is specific for determining the effective thickness of 0.5mm-thick EBM printed flexures. The factor will vary with different thickness as well as printing directions and manufacturing conditions.

Next, the coefficient factor, $\lambda = 1.27$, is used to calculate the effective thickness of the C-T beams in the 3D-printed CPM. With the designed thickness of 0.49 mm, the effective thickness of the C-T beams is found to be 0.62 mm. This value is applied to reanalyze the 3D-printed CPM, the results show that the first resonance frequency has increased from 98 Hz to 133 Hz and the corresponding compliant matrix, $\overline{C}'^{\text{3-DOF}}$, is written as

$$
\overline{C}'^{\text{3-DOF}} = \begin{bmatrix}
3.21e-8 & & & & & \\
0 & 3.21e-8 & & & SYM & \\
0 & 0 & 8.98e-5 & & & \\
-3.31e-6 & 7.84e-8 & 0 & 3.05e-2 & & \\
-7.84e-8 & -3.31e-6 & 0 & 0 & 3.05e-2 & \\
0 & & 4.28e-6 & 0 & 0 & 1.50e-4
\end{bmatrix}
\tag{4.4}
$$

Note that the stiffness and resonance frequency of the CPM presented in the remaining of this Chapter will be referred to $\overline{C}'^{\text{3-DOF}}$ and 133 Hz instead of $C'^{\text{3-DOF}}$ and 98 Hz respectively.

In addition, the large workspace of ±3° × ±3° × ±2 mm of the 3D-printed prototype could still be achieved.

4.3 Evaluation on the Stiffness and Dynamic Properties of the 3D-Printed CPM

The actuating stiffness of the 3D-printed CPM is evaluated using the same experimental setups as the milled prototype (see Figure 3.9 and Figure 3.11). The experimental results of the compliance along the Z axis, about the X axis and about the Y axis are shown in Figure 4.5, Figure 4.6 and Figure 4.7 respectively.
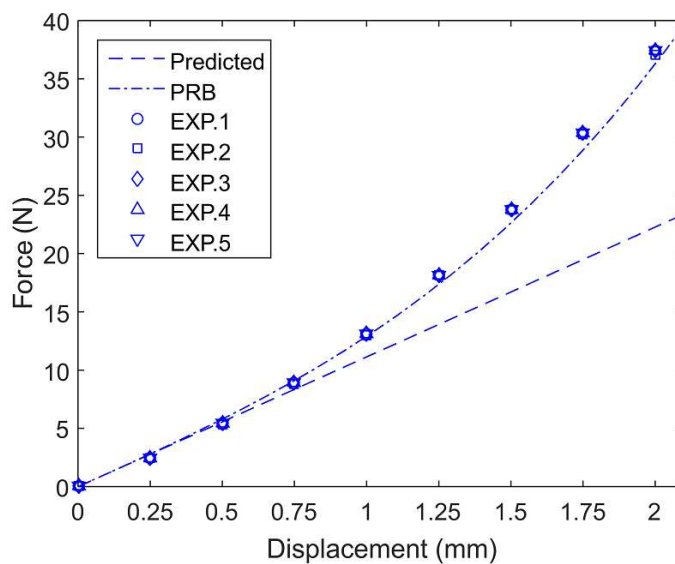
Figure 4.5: Measured compliance of the 3D-printed CPM along the Z axis.

Figure 4.5 shows that for small displacement below 1 mm, the measured force along the Z axis is almost linear and the average deviation between the predicted and measured data is 7.6%. However, for displacement above 1 mm, the difference between the measured forces and the predicted values has increased, causing the average deviation over the full work range to be 26%. This is similar to the experimental result of the milled prototype shown in Figure 3.10, the nonlinear compliance along the Z axis is due to the over-constrained structure of the

CPM. The predicted results obtained via FEA are only applicable for predicting the compliance over the small displacement. The results are not suitable for estimating the nonlinear behavior of the over-constrained CPM over the large work range. Therefore, the PRB model presented in Appendix A is used to estimate the nonlinear compliance of the 3D-printed CPM over the full workspace. Similar to the milled-prototype, the analytical results from the PRB model agree well with the experimental results with an average deviation of 4.3% over the full workspace along the Z axis of the CPM.
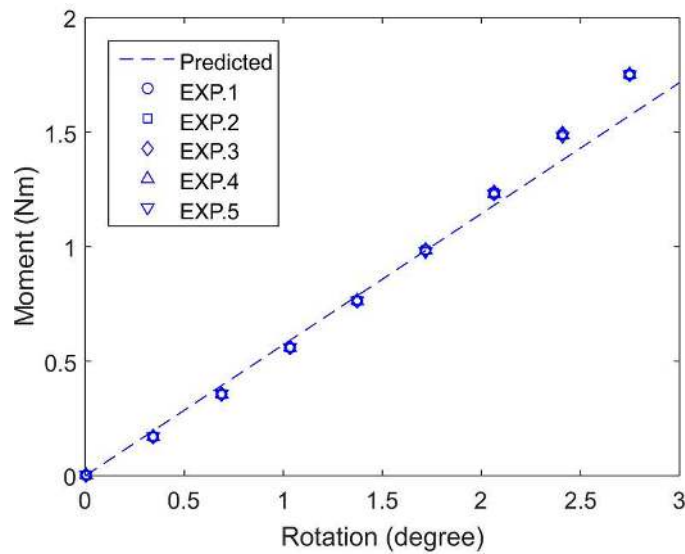
Figure 4.6: Measured compliance of the 3D-printed CPM about the X axis.
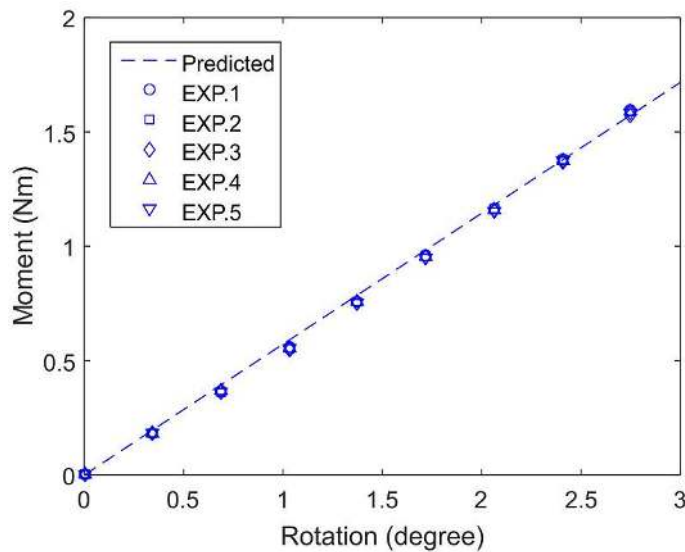
Figure 4.7: Measured compliance of the 3D-printed CPM about the Y axis.

For the rotational compliance shown in Figure 4.6 and Figure 4.7, it is seen that the experimental compliance of the 3D-printed CPM are nearly linear and close to the predicted data with the average deviations of 6.1% and 3.4% about the X and Y axes respectively.

The experimental setup shown in Figure 3.14 is used to measure the dynamic response of the 3D-printed CPM and the obtained result is shown in Figure 4.8. It is observed that the resonance along the Z axis occurs at 119 Hz which is close to the predicted value of 133 Hz, with a deviation of 10.5%. Hence, it can be said that the dynamic behavior of the 3D-printed CPM is significantly better than the milled CPM (which has the deviation of dynamic response up to 15.6%). The improvement of the prediction is due to the monolithic structure of the 3D-printed prototype that eliminates all assembly errors as well as the additional mass of mounting parts. This also goes to show that the predictable dynamic response can be obtained from CPMs fabricated by 3D printing technology.
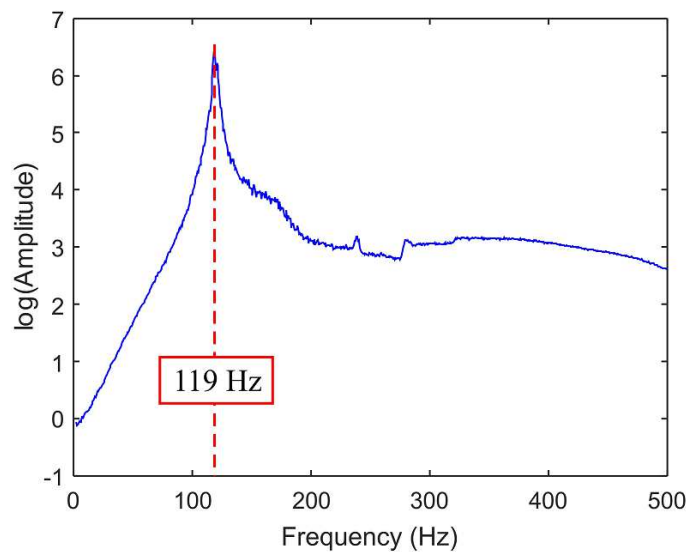
Figure 4.8: Experimental dynamic response of the 3D-printed CPM along the Z axis.

4.4 Precision Manipulator based on 3D-Printed CPM

A 3-DOF manipulator as shown in Figure 4.9 is developed based on the 3D-printed CPM with three voice-coil (VC) motors (Akribis AMV60-25) having stroke of 25 mm,

continuous force and current at 100°C of 26.35 N and 1.55 A respectively. Displacements of the VC motors are measured by three linear encoders (MicroE Systems MII5000 and MII6000 series) with resolution of up to 1.2 nm. Experiments are conducted to show that the manipulator could achieve the desired workspace of ±3° × ±3° × ±2 mm, and the positioning accuracy of three actuating motions will be evaluated to demonstrate that 3D-printed CPMs can be used in precise motion systems.
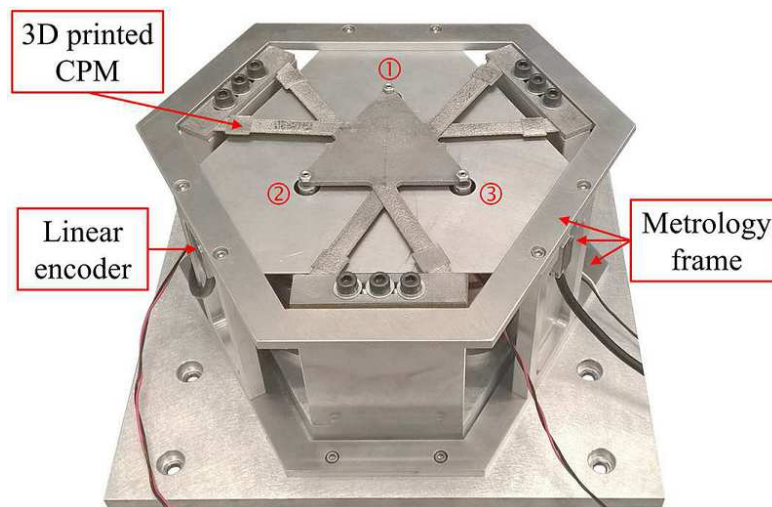
Figure 4.9: 3-DOF manipulator developed based on the 3D-printed CPM.

4.4.1 Workspace evaluation

A linear probe (MILLIMAR 1318 with measuring range of 2 mm, resolution of 0.1 µm and accuracy of 0.9 µm) is used to measure the displacement at the center of the end effector along the Z axis as shown in Figure 4.10. Since the contact measurement technique is used in this experiment, an aluminum plate with flat surface is attached to the end effector to cover the rough surface of the 3D-printed prototype and thus enhance the accuracy of the measurements. The experiment is carried out with an increment of 0.25 mm along the Z axis and repeated five times. The experimental results are shown in Figure 4.11. It is seen that the manipulator is able to operate over the full work range of ±2 mm along the Z axis with good accuracy and repeatability. The maximum positioning error of 6% is found to occur at -1.75 mm position.
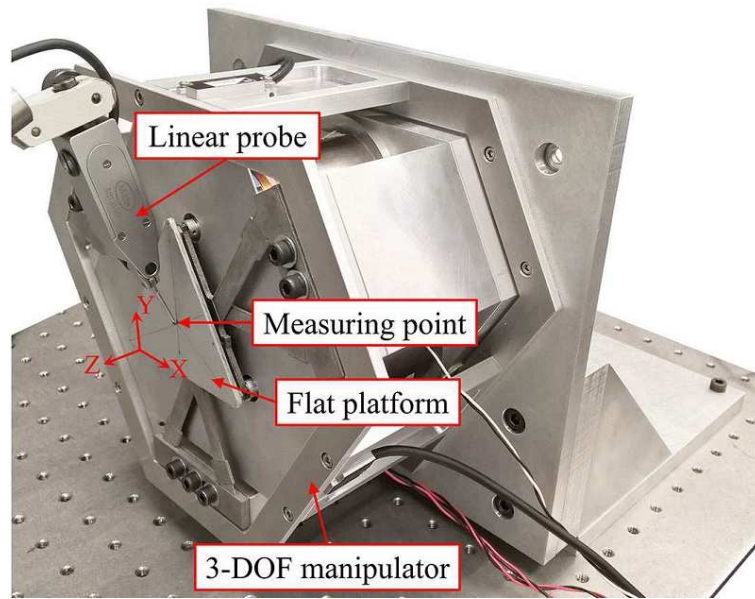
Figure 4.10: Experimental setup for measuring the workspace along the Z axis of the 3-DOF manipulator.
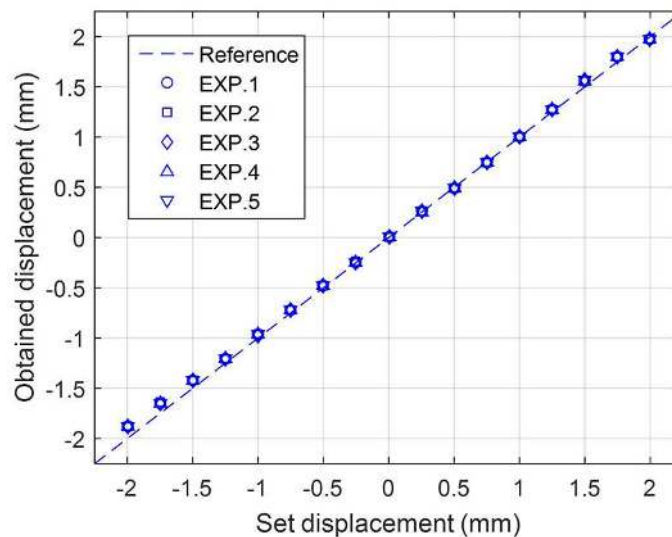
Figure 4.11: Experimental workspace of the 3-DOF manipulator along the Z axis.

For evaluating the workspace of the manipulator about the X and Y axes, two linear probes are used to measure the displacements of the end effector at two opposite points about the rotation axis. The setup used to measure the workspace about the Y axis is shown in Figure 4.12 and a similar setup is adopted to measure the workspace about the X axis. The rotation angles could then be calculated from the obtained measurements and the distance between two

78

measuring points. The experimental results of the workspace about the *X* and *Y* axes are shown in Figure 4.13 and Figure 4.14 respectively.
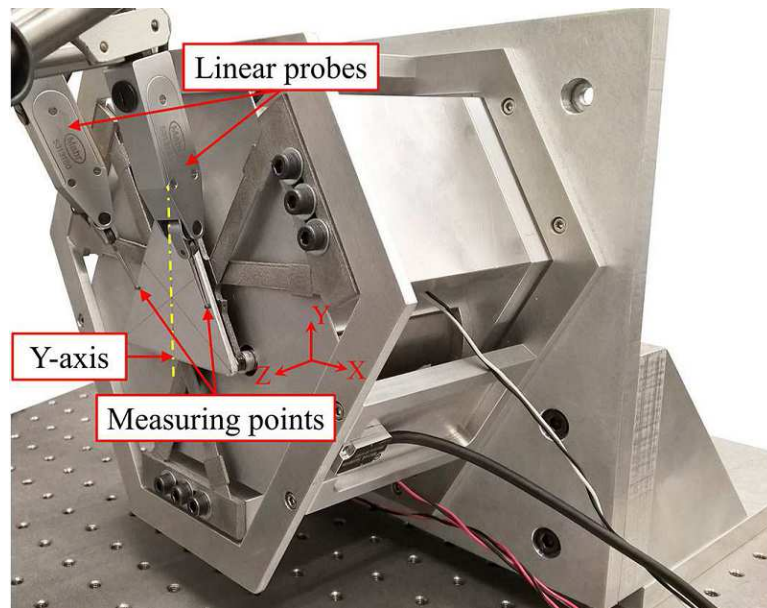
Figure 4.12: Experimental setup for measuring the workspace about the *Y* axis of the 3-DOF manipulator.
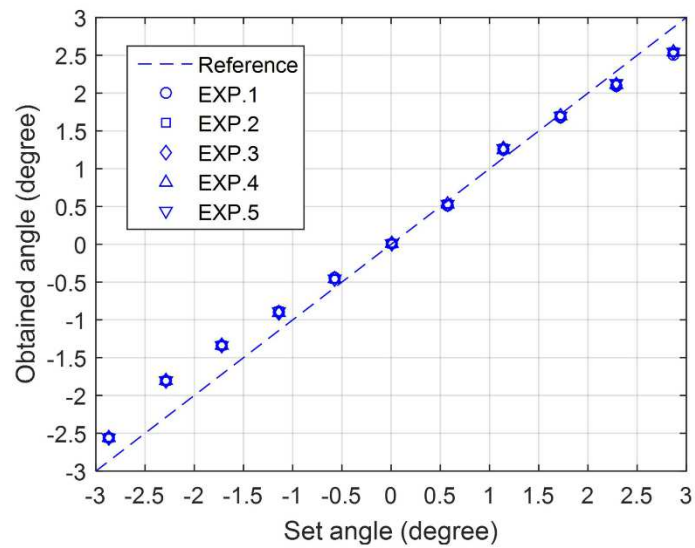
Figure 4.13: Experimental workspace of the 3-DOF manipulator about the *X* axis.
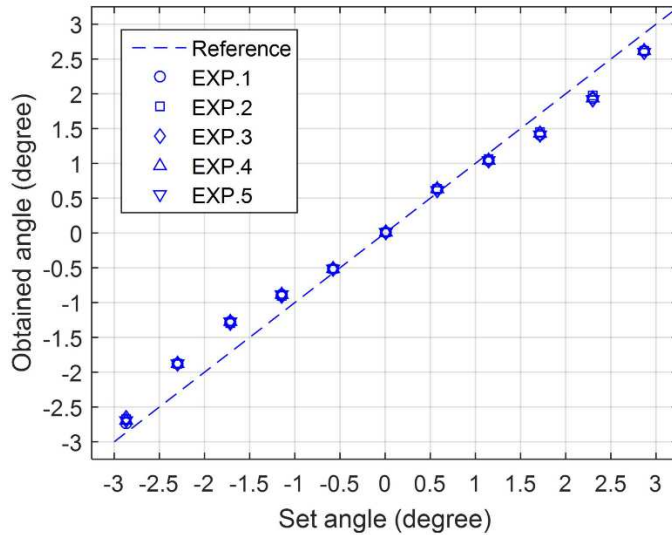
Figure 4.14: Experimental workspace of the 3-DOF manipulator about the *Y* axis.

It is observed that the positioning accuracy of the rotational motions is lower than that of translation, especially for the large angular displacement. For the rotational motions, the maximum positioning errors are found to be 22% at -1.72° about the *X* axis and 25% at 1.72° about the *Y* axis. The large positioning errors can be overcome if a closed-loop control is implemented. From the experimental results, it has been shown that the 3-DOF manipulator could achieve the full workspace of ±3° × ±3° × ±2 mm with good repeatability. Hence it can be said that the 3D-printed CPM is suitable in manipulator systems since it can provide large workspace as well as repeatable motions.

4.4.2 Positioning evaluation

A 3-axes interferometer (SIOS SP 2000 TR) is used to measure the positioning resolution of the 3-DOF manipulator. The laser interferometer is able to measure three out-of-plane motions with the resolution of 0.1 nm for translation and 0.002" for rotation, the angular measuring range is ±1.5'. The experimental setup is shown in Figure 4.15. A metrology mirror is attached to the end effector and the 3-axes interferometer is placed at a specific distance from the manipulator such that it can receive the reflecting beams from the mirror.
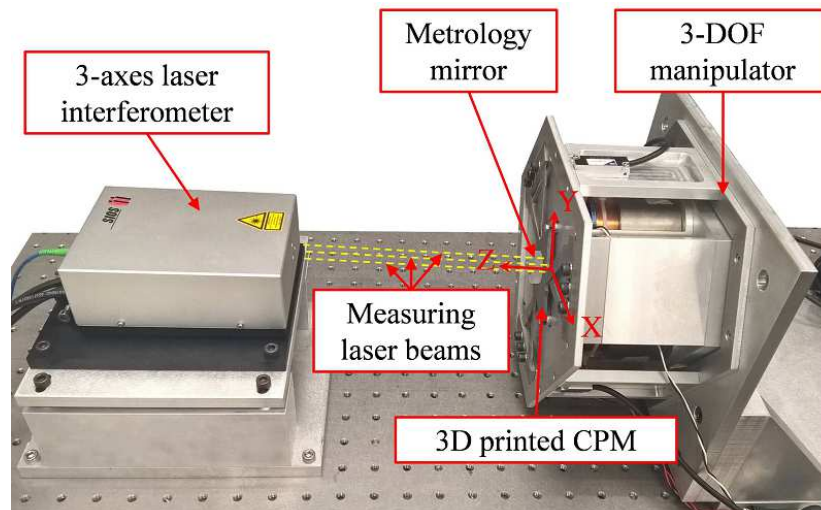
Figure 4.15: Experimental setup for measuring the positioning resolution of the manipulator.

To evaluate the positioning accuracy of the manipulator along the Z axis, a displacement of 20 nm is used as the step resolution for the VC motors since the motor has a maximum positioning noise of ±10 nm. The experiment is conducted by moving the end effector from the neutral position to 80 nm and then back to the initial position in steps of 20 nm. Figure 4.16 shows the translational displacement of the end effector monitored by the laser interferometer. From the graph, it is seen that the manipulator is capable of repeatable motion, with a positioning accuracy of ±10.8 nm and a maximum positioning error of 8.6 nm.
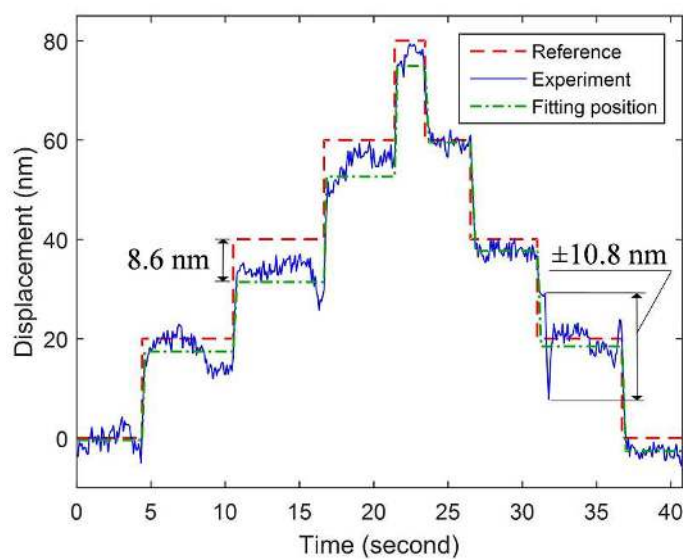
Figure 4.16: Step displacement of the manipulator along the Z axis.

By using 20 nm as the step resolution for the VC motor, the angular resolutions about the X and Y axes of the manipulator are 0.14" and 0.12" respectively. The step angular displacements of the manipulator about the X and Y axes are shown in Figure 4.17 and Figure 4.18 respectively. The results suggest that for the rotational motions, the manipulator is able to achieve an accuracy of ±0.058" and a maximum positioning error of 0.038" about the X axis, as well as an accuracy of ±0.065" and a maximum positioning error of 0.048" about the Y axis.
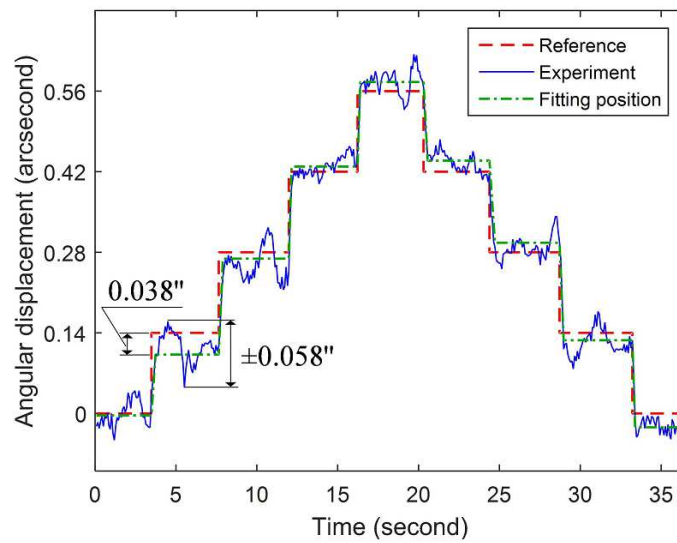
Figure 4.17: Step displacement of the manipulator about the X axis.
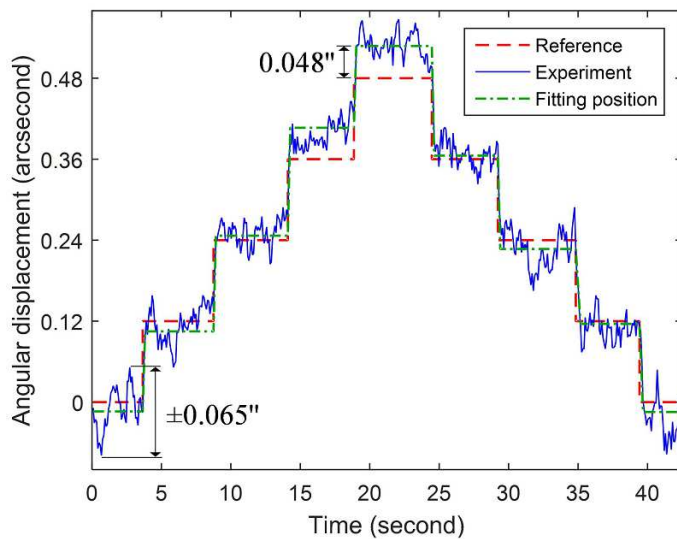
Figure 4.18: Step displacement of the manipulator about the Y axis.

4.5 Summary

This chapter presents the characterization of 3D-printed flexures and the performance of 3D-printed CPM in precise positioning systems. A prototype of the 3-DOF ($\theta_X - \theta_Y - Z$) CPM proposed in Section 3.5 is built by EBM method. The CPM is able to produce a large workspace of $\pm3° \times \pm3° \times \pm2$ mm, fast dynamic response of 119 Hz and high non-actuating stiffness. It is found that there is a significant difference between the measured thickness and the designed thickness for the C-T beams in the CPM. A coefficient factor of 1.27 is proposed to determine the effective thickness for the 3D-printed CPM with 0.5mm-thick flexures. Using the effective thickness, it has been shown that the analytical results agree well with the experimental results on the stiffness and dynamic properties of the CPM with the highest deviation being 10.5%. Thus, the proposed coefficient factor provides a good basis for determining the performance of 3D-printed compliant mechanisms. In order to govern the effective thickness for other compliant structures, numerous coefficient factors for EBM-printed flexures with different designed thickness and building directions have been investigated, and the obtained results are summarized in Appendix C .

In addition, a 3-DOF manipulator is built based on the 3D-printed CPM with three VC motors. From the experimental results, it has been shown that the manipulator can achieve the full workspace of $\pm3° \times \pm3° \times \pm2$ mm with good resolution of 0.14" $\times$ 0.12" $\times$ 20 nm and accuracy of $\pm0.058" \times \pm0.065" \times \pm10.8$ nm. Through this chapter, it is demonstrated that the EBM technology is suitable for fabricating compliant mechanisms in precise manipulation systems.

CHAPTER 5
DESIGN CRITERIA FOR 3-LEGGED CPM WITH FULLY-DECOUPLED MOTION CHARACTERISTICS

In previous Chapters, a 3-DOF ($\theta_X - \theta_Y - Z$) CPM has been synthesized by the novel beam-based method, analysis and experimental results demonstrate that it is able to provide good stiffness and dynamic characteristics and be used in precise manipulation systems. However, the synthesized CPM is not able to deliver decoupled motions that are demonstrated by the existence of five non-diagonal components within the compliance matrix as shown in Eqs. (3.19) and (4.4). This is because the motion property of the CPM has not been taken into account during the synthesis process. Past literatures show that the decoupled-motion property of CPMs has not been clearly discussed, especially for those synthesized by optimization approach. Since motion-decoupling capability is essential for precise motion systems, some insights into the design criteria for synthesizing CPMs with fully-decoupled motions will be presented in this Chapter.

5.1 Background

In general, a CPM consists of three rotational-symmetric limbs where each limb is formed by either one or a series of flexure elements, e.g., thin slender beams or notch hinges etc., connected together. Hence, each limb can be partially-compliant; if a rigid-link is used to connect two flexure elements, or fully compliant; if there is no rigid-link between two flexure elements. Depending on the structure of limb, CPM can be classified into two types, i.e., single

serial flexure chain and double reflecting serial flexure chains in a limb. In an ideal case, the output motions of any CPM have to be fully decoupled, i.e., delivering the desired DOF in the actuating directions and without any parasitic motion in the non-actuating directions. Based on Hooke's Law, the motion property (coupled or decoupled) of a compliant mechanism is governed by a 6 × 6 stiffness matrix where the diagonal components represent the stiffness characteristics of all six possible actuation directions while the non-diagonal components are responsible for the off-axes (or non-actuating) stiffness characteristics.

Based on the derived 6 × 6 stiffness/compliance matrices, only few recent CPMs demonstrate decoupled motions [134] while most CPMs could only deliver coupled motions [129]. The main reason is because the existing CPMs are synthesized with the aim of achieving the desired DOF. As a result, they are able to deliver the motions in the desired actuating directions but also producing undesired parasitic motions in the non-actuating directions. More recent efforts mainly focus on synthesizing CPMs with high stiffness ratios and high non-diagonal stiffness components within the 6 × 6 stiffness matrices [74, 75, 121] so as to keep the undesired parasitic motions to very small percentage as compared to the actuating motions. With motion decoupling being an important performance indicator for any positioning system, this Chapter presents the fundamentals for designing CPMs with fully-decoupled motion characteristics.

5.2 Stiffness Modeling of CPMs Containing a Single Serial Flexure Chain in a Limb

Here, a CPM is represented by a mechanism having three compliant limbs that are distributed symmetrically about the center of the end effector. The limbs are fixed at one end while the free ends are connected with the end effector. Each limb contains a serial chain of flexure elements and rigid links as illustrated in Figure 5.1. Here, the global frame, *XYZ*, is

attached to center of the end effector and the local frame of each limb, $X'Y'Z'$, is attached at the free end of each limb. Note that the $X'Y'$ plane of the local frame of each limb lies on the same plane as the XY plane of the global frame.
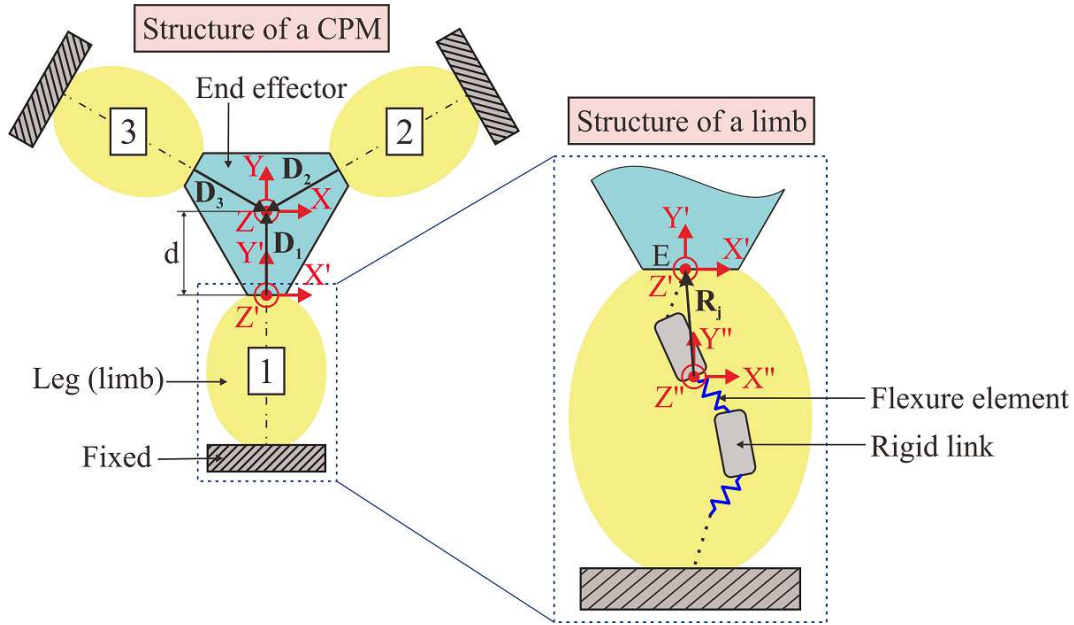
Figure 5.1: Construction of a CPM containing a single serial flexure chain in a limb.

The stiffness property of a CPM is governed by the stiffness of the limbs and the end effector. The stiffness matrix of the limb along the Y axis is represented by K^l with respect to (w.r.t.) the local frame, i.e., at point E as shown in Figure 5.1. With $\mathbf{D}$ being the vector represents the distance between the local frame and the global frame, the stiffness matrix of entire CPM, K^m, is expressed as

$$K^m = \sum_{i=1}^{3} J_i^l R_i^l K^l \left(R_i^l \right)^{-1} \left(J_i^l \right)^T \tag{5.1}$$

where $i = 1, 2, 3$ denotes the three limbs in the CPM, J_i^l is the translation matrix from the local frame of the ith limb to the global frame and R_i^l is the rotation matrix about the Z axis of the ith limb. As three limbs are symmetrical and 120° apart, R_i^l and J_i^l are written as

$$R_i^l = \begin{bmatrix} R_z(\theta_i) & 0 \\ 0 & R_z(\theta_i) \end{bmatrix} \quad \text{where} \quad R_z(\theta_i) = \begin{bmatrix} \cos\theta_i & -\sin\theta_i & 0 \\ \sin\theta_i & \cos\theta_i & 0 \\ 0 & 0 & 1 \end{bmatrix} \tag{5.2}$$

$$J_i^l = \begin{bmatrix} I & 0 \\ T_i^l & I \end{bmatrix} \quad \text{where} \quad T_i^l = \begin{bmatrix} 0 & D_{z_i} & -D_{y_i} \\ -D_{z_i} & 0 & D_{x_i} \\ D_{y_i} & -D_{x_i} & 0 \end{bmatrix} \tag{5.3}$$

Here, the values of θ_1, θ_2, θ_3 are 0°, 120° and 240° respectively and D_{x_i}, D_{y_i}, D_{z_i} are three components of $\mathbf{D_i}$ represent the projections of the distance from each local frame to the global frame onto the X, Y and Z axes respectively. Note that $D_{z_i} = 0$ since the $X'Y'$ plane of the local frames lies on the same plane as the XY plane of the global frame.

Based on Maxwell reciprocity and the theory of a continuum body, K^l is represented as

$$K^l = \begin{bmatrix} k_{11}^l & & & & & \\ k_{21}^l & k_{22}^l & & & SYM & \\ k_{31}^l & k_{32}^l & k_{33}^l & & & \\ k_{41}^l & k_{42}^l & k_{43}^l & k_{44}^l & & \\ k_{51}^l & k_{52}^l & k_{53}^l & k_{54}^l & k_{55}^l & \\ k_{61}^l & k_{62}^l & k_{63}^l & k_{64}^l & k_{65}^l & k_{66}^l \end{bmatrix} \tag{5.4}$$

where the non-diagonal components are symmetrical. By substituting Eqs. (5.2), (5.3) and (5.4) into Eq. (5.1), the general form of the stiffness matrix of a CPM is

$$K^m = \begin{bmatrix} k_{11}^m & & & & & \\ 0 & k_{22}^m & & & SYM & \\ 0 & 0 & k_{33}^m & & & \\ k_{41}^m & k_{42}^m & 0 & k_{44}^m & & \\ k_{51}^m & k_{52}^m & 0 & 0 & k_{55}^m & \\ 0 & 0 & k_{63}^m & 0 & 0 & k_{66}^m \end{bmatrix} \tag{5.5}$$

With d denoting the size of the end effector as illustrated in Figure 5.1, the expressions of the non-zero components within the stiffness matrix written in Eq. (5.5) are expressed as

$$
\begin{aligned}
k_{11}^m &= k_{22}^m = \frac{3}{2}\left(k_{11}^l + k_{22}^l\right) \\
k_{33}^m &= 3k_{33}^l \\
k_{44}^m &= k_{55}^m = \frac{3}{2}\left(d^2 k_{33}^l - 2dk_{43}^l + k_{44}^l + k_{55}^l\right) \\
k_{66}^m &= 3\left(d^2 k_{11}^l + 2dk_{61}^l + k_{66}^l\right) \\
k_{41}^m &= k_{52}^m = -\frac{3}{2}\left(dk_{31}^l - k_{41}^l - k_{52}^l\right) \\
k_{51}^m &= -k_{42}^m = \frac{3}{2}\left(k_{51}^l + dk_{32}^l - k_{42}^l\right) \\
k_{63}^m &= 3\left(dk_{31}^l + k_{63}^l\right)
\end{aligned}
\tag{5.6}
$$

In Eq. (5.6), the five non-diagonal components within K^m (k_{41}^m, k_{42}^m, k_{51}^m, k_{52}^m, k_{63}^m) are represented by seven components within K^l (k_{31}^l, k_{32}^l, k_{41}^l, k_{42}^l, k_{51}^l, k_{52}^l, k_{63}^l). These seven non-diagonal components are also known as dependent variables mathematically. To fulfill the requirements of a fully-decoupled-motion CPM, all non-diagonal components in K^m must be zeros. Here, the 6×6 stiffness matrix of a CPM with fully-decoupled motion characteristic will be termed as a diagonal stiffness matrix as shown in Eq. (5.7) since a square matrix with all non-diagonal components being zeros is also known as a diagonal matrix mathematically.

$$K^m = \begin{bmatrix} k_{11}^m & & & & & \\ 0 & k_{22}^m & & & & \\ 0 & 0 & k_{33}^m & & & \\ 0 & 0 & 0 & k_{44}^m & & \\ 0 & 0 & 0 & 0 & k_{55}^m & \\ 0 & 0 & 0 & 0 & 0 & k_{66}^m \end{bmatrix} \tag{5.7}$$

With $k_{41}^m = k_{52}^m$ and $k_{51}^m = -k_{42}^m$, the relationship between those seven variables expressed in Eq. (5.6) can only be represented by three equations and this condition leads to a multiple-solutions problem. Hence, it is important to note that this work only uses a special case (or solution) to demonstrate how the presented mathematical models can be used to synthesize a CPM with the aim of achieving fully-decoupled motion capability. This special case is to make those seven components within K^l to be zeros as shown below.

$$K^l = \begin{bmatrix} k_{11}^l & & & & & \\ k_{21}^l & k_{22}^l & & & SYM & \\ 0 & 0 & k_{33}^l & & & \\ 0 & 0 & k_{43}^l & k_{44}^l & & \\ 0 & 0 & k_{53}^l & k_{54}^l & k_{55}^l & \\ k_{61}^l & k_{62}^l & 0 & k_{64}^l & k_{65}^l & k_{66}^l \end{bmatrix} \tag{5.8}$$

Next, a typical limb of a CPM is formed by either single flexure element or a serial chain of flexure elements and rigid links. The desired motions are generated by the elastic deformation of various oriented flexure elements while the rigid links only serve as connecting elements for the flexures with defined relative positions. Here, the two popular flexures that are popularly used to synthesize the compliant mechanisms, the beam type and the notch type as shown in Figure 5.2, are used as standard flexure elements for analysis. Both flexure elements have thin features which permit elastic bending in specific direction.
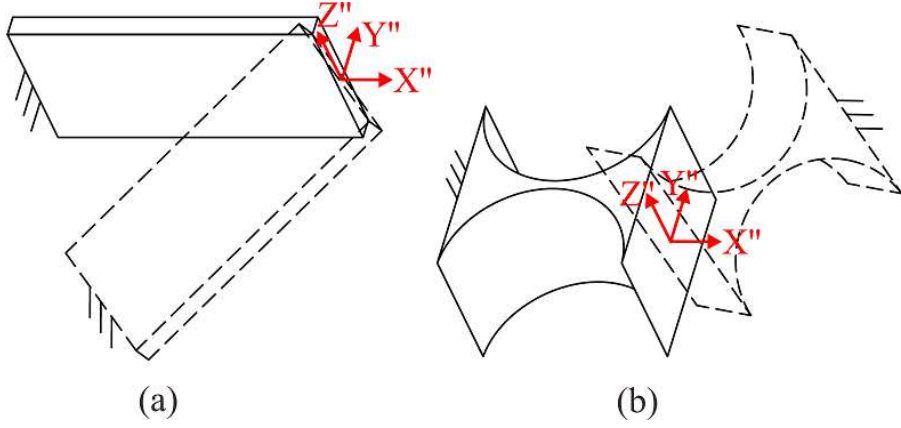
Figure 5.2: Original orientation of the flexure elements (solid lines); (a) beam type and (b) notch type, with the local frames, $X''Y''Z''$, attached at the free ends and the arbitrary orientation of the flexure elements (dotted lines) about these local frames.

Assuming that each limb is formed by a serial chain of flexure elements and rigid links where a rigid link has infinite stiffness (non-compliance) property, the stiffness of each limb is governed by the compliance of each flexure elements, C_j^e, expressed as

$$C^l = \sum_{j=1}^{n} J_j^e R_j^e C_j^e \left(R_j^e \right)^{-1} \left(J_j^e \right)^T \tag{5.9}$$

where n denotes the number of flexure elements, J_j^e and R_j^e are the rotation matrix, and translation matrix of the jth flexure element respectively. Referring to [142], the compliance matrix of each original flexure element, C_j^e, w.r.t. the local frame as illustrated in Figure 5.2 is defined as

$$C_j^e = \begin{bmatrix} c_{11}^e & & & & & \\ 0 & c_{22}^e & & & SYM & \\ 0 & 0 & c_{33}^e & & & \\ 0 & 0 & 0 & c_{44}^e & & \\ 0 & 0 & c_{53}^e & 0 & c_{55}^e & \\ 0 & c_{62}^e & 0 & 0 & 0 & c_{66}^e \end{bmatrix} \tag{5.10}$$

90

Eq. (5.10) is applicable for both the beam-type and notch-type flexure elements [142]. In addition, the geometry of each flexure-element type can vary without changing the form of the compliant matrix. In particular, a beam-type flexure element can have a rectangular, polygon or circular cross-sectional area, etc., while the profile of notch-type flexure element can be a circular arc, parabola, ellipse or hyperbola, etc. Several kinds of other flexure elements which have similar form of compliance matrix are presented in Appendix D . The components within C_j^e can change due to the specific type of flexure element yet the form of the compliance matrix will always remain unchanged. Note that the $X''Y''$ plane of the local frame of each flexure element (Figure 5.2) lies on the parallel plane with the XY plane of the global frame as illustrated in Figure 5.1. In Eq. (5.9), the rotation matrix, R_j^e, is a 6×6 matrix and is defined as the multiplication of the rotation matrices about the X'', Y'' and Z'' axes ($R_{x_j}^e$, $R_{y_j}^e$ and $R_{z_j}^e$ respectively). Hence, it is written as

$$R_j^e = \begin{bmatrix} R_{z_j}^e R_{y_j}^e R_{x_j}^e & 0 \\ 0 & R_{z_j}^e R_{y_j}^e R_{x_j}^e \end{bmatrix} \quad \text{where} \quad R_{z_j}^e = \begin{bmatrix} \cos\gamma_j & -\sin\gamma_j & 0 \\ \sin\gamma_j & \cos\gamma_j & 0 \\ 0 & 0 & 1 \end{bmatrix},$$

$$R_{y_j}^e = \begin{bmatrix} \cos\beta_j & 0 & \sin\beta_j \\ 0 & 1 & 0 \\ -\sin\beta_j & 0 & \cos\beta_j \end{bmatrix}, \qquad (5.11)$$

$$R_{x_j}^e = \begin{bmatrix} 1 & 0 & 0 \\ 0 & \cos\alpha_j & -\sin\alpha_j \\ 0 & \sin\alpha_j & \cos\alpha_j \end{bmatrix}$$

Here, α_j, β_j and γ_j represent the rotation angles about the X'', Y'' and Z'' axes respectively. The geometries of a flexure element before and after orientation are illustrated in Figure 5.2. As for the 6×6 translation matrix, J_j^e, it represents the projected distances onto the three axes

$(r_{x_j}, r_{y_j}, r_{z_j})$ from the jth flexure element to the local frame of the leg which are indicated by vector $\mathbf{R_j}$ as shown in Figure 5.1, written as

$$J_j^e = \begin{bmatrix} I & D_j^e \\ 0 & I \end{bmatrix} \quad \text{where} \quad D_j^e = \begin{bmatrix} 0 & r_{z_j} & -r_{y_j} \\ -r_{z_j} & 0 & r_{x_j} \\ r_{y_j} & -r_{x_j} & 0 \end{bmatrix} \tag{5.12}$$

Using Eqs. (5.9) to (5.12), the compliance matrix of a limb, C^l, can be obtained and the stiffness matrix of each limb is given as $K^l = \left(C^l \right)^{-1}$.

As mentioned earlier, the stiffness matrix of each limb must follow the exact form as shown in Eq. (5.8) and this requirement applies to its corresponding compliance matrix too. The derivation of the compliance matrix of a limb with the aim of achieving that requirement is presented in Appendix E . To summarize the results obtained from Appendix E , one condition, which allows the compliance matrix of a limb to become the exact same form as Eq. (5.8), is that seven components within the compliance matrix of a limb need to be zeros, i.e., $c_{31}^l = c_{32}^l = c_{41}^l = c_{42}^l = c_{51}^l = c_{52}^l = c_{63}^l = 0$. This condition offers simplicity during the design stage and can be used as the standard approach to synthesize CPMs with the aim of achieving fully-decoupled motion capability. However, it also introduces a multiple-solutions problem to solve the corresponding components within the stiffness matrix, K^l. Among a number of possible solutions, $k_{64}^l = k_{65}^l = 0$ is a unique solution that is used to fulfill the condition in this work. By adopting this unique solution, both the stiffness matrix and the compliance matrix of a limb will have the same form as expressed in Eq. (5.13), and the expression of each component within K^l is given in Appendix F . It shows that the compliance matrix of a limb must have nine non-diagonal components equal to zeros to synthesize a CPM with the aim of achieving fully-decoupled motion capability. As the compliance matrix of a limb is governed by flexure

92

elements with various orientations and positions, the rotation and translation matrices of each flexure element must be specified.

$$
\underbrace{\begin{bmatrix}
k_{11}^{l} & & & & & \\
k_{21}^{l} & k_{22}^{l} & & & SYM & \\
0 & 0 & k_{33}^{l} & & & \\
0 & 0 & k_{43}^{l} & k_{44}^{l} & & \\
0 & 0 & k_{53}^{l} & k_{54}^{l} & k_{55}^{l} & \\
k_{61}^{l} & k_{62}^{l} & 0 & 0 & 0 & k_{66}^{l}
\end{bmatrix}}_{K^{l}}
=
\underbrace{\begin{bmatrix}
c_{11}^{l} & & & & & \\
c_{21}^{l} & c_{22}^{l} & & & SYM & \\
0 & 0 & c_{33}^{l} & & & \\
0 & 0 & c_{43}^{l} & c_{44}^{l} & & \\
0 & 0 & c_{53}^{l} & c_{54}^{l} & c_{55}^{l} & \\
c_{61}^{l} & c_{62}^{l} & 0 & 0 & 0 & c_{66}^{l}
\end{bmatrix}^{-1}}_{\left(C^{l}\right)^{-1}}
\tag{5.13}
$$

5.3 Characteristics of Flexure Elements in Decoupled-Motion CPMs

In this Section, the desired rotation angles (α, β, γ) and distances (r_x, r_y, r_z) of flexure elements in a limb to achieve decoupled-motion capability will be analyzed. First, Eq. (5.9) is re-expressed as

$$
K^{l} = \left(C^{l}\right)^{-1} = \left(\sum_{j=1}^{n} J_{j}^{e} R_{j}^{e} C_{j}^{e} \left(R_{j}^{e}\right)^{-1} \left(J_{j}^{e}\right)^{T}\right)^{-1} = \left(\sum_{j=1}^{n} \bar{C}_{j}^{e}\right)^{-1}
\tag{5.14}
$$

where $\bar{C}_{j}^{e}$ indicates the compliance matrix of the jth flexure element referring to the frame $X'Y'Z'$ attached to the free end of the limb as illustrated in Figure 5.1. In order to achieve fully-decoupled motion capability, the nine non-diagonal components (c_{31}^{l}, c_{41}^{l}, c_{51}^{l}, c_{32}^{l}, c_{42}^{l}, c_{52}^{l}, c_{63}^{l}, c_{64}^{l}, c_{65}^{l}) within the compliance matrix, C^{l}, must be zeros as shown in Eq. (5.13). As C^{l} is the sum of n sub-components, $\bar{C}_{j}^{e}$, there could be numerous solutions. In this work, a special case where all $\bar{C}_{j}^{e}$ have the same form ($\bar{C}^{e}$) is considered and yields

$$\bar{C}^e = \begin{bmatrix} \bar{c}_{11}^e & & & & & \\ \bar{c}_{21}^e & \bar{c}_{22}^e & & & SYM & \\ \bar{c}_{31}^e = 0 & \bar{c}_{32}^e = 0 & \bar{c}_{33}^e & & & \\ \bar{c}_{41}^e = 0 & \bar{c}_{42}^e = 0 & \bar{c}_{43}^e & \bar{c}_{44}^e & & \\ \bar{c}_{51}^e = 0 & \bar{c}_{52}^e = 0 & \bar{c}_{53}^e & \bar{c}_{54}^e & \bar{c}_{55}^e & \\ \bar{c}_{61}^e & \bar{c}_{62}^e & \bar{c}_{63}^e = 0 & \bar{c}_{64}^e = 0 & \bar{c}_{65}^e = 0 & \bar{c}_{66}^e \end{bmatrix} \tag{5.15}$$

Note that $\bar{C}^e$ in Eq. (5.15) is different from C^e in Eq. (5.10) since $\bar{C}^e = J^e R^e C^e \left(R^e \right)^{-1} \left(J^e \right)^T$

as expressed in Eq. (5.14). R^e and J^e are similar to Eqs. (5.11) and (5.12) with the subscript, j, being removed.

Eq. (5.15) describes the condition to obtain a CPM with fully-decoupled motions. It contains nine equations that can be obtained based on those nine zero components as written from Eq. (5.16) to Eq. (5.24). Note that there are six unknowns in the proposed nine equations. The unknowns are the rotation angles (α, β, γ) and the distances (r_x, r_y, r_z) measured from the moving end of the flexure element to the free end of the limb.

$$
\begin{aligned}
c_{31}^e =& -c_{11}^e \sin\beta \cos\beta \cos\gamma + c_{44}^e \cos\beta \left(r_y \cos\gamma - r_x \sin\gamma \right)\left(r_y \sin\beta + r_z \cos\beta \sin\gamma \right) - \\
& \cos\beta \sin\alpha \left\{ \cos\gamma \sin\alpha \left(c_{62}^e r_z - c_{22}^e \sin\beta \right) + \cos\alpha \left[c_{62}^e r_y \cos\beta + \left(c_{22}^e - c_{62}^e r_z \sin\beta \right)\sin\gamma \right] \right\} + \\
& \cos\alpha \cos\beta \left\{ \cos\alpha \cos\gamma \left(c_{53}^e r_z + c_{33}^e \sin\beta \right) + \sin\alpha \left[-c_{53}^e r_y \cos\beta + \left(c_{33}^e + c_{53}^e r_z \sin\beta \right)\sin\gamma \right] \right\} + \\
& \left[\sin\alpha \sin\beta \left(r_y \cos\gamma - r_x \sin\gamma \right) - \cos\alpha \left(r_x \cos\gamma + r_y \sin\gamma \right) \right] \cdot \\
& \left\{ \cos\alpha \cos\gamma \left(c_{55}^e r_z + c_{53}^e \sin\beta \right) + \sin\alpha \left[-c_{55}^e r_y \cos\beta + \left(c_{53}^e + c_{55}^e r_z \sin\beta \right)\sin\gamma \right] \right\} + \\
& \left[\cos\gamma \left(r_x \sin\alpha + r_y \cos\alpha \sin\beta \right) + \left(r_y \sin\alpha - r_x \cos\alpha \sin\beta \right)\sin\gamma \right] \cdot \\
& \left\{ \cos\gamma \sin\alpha \left(-c_{66}^e r_z + c_{62}^e \sin\beta \right) - \cos\alpha \left[c_{66}^e r_y \cos\beta + \left(c_{62}^e - c_{66}^e r_z \sin\beta \right)\sin\gamma \right] \right\}
\end{aligned} \tag{5.16}
$$

$$\overline{c}_{41}^{e} = c_{44}^{e}\cos\beta\cos\gamma\left(r_{y}\sin\beta + r_{z}\cos\beta\sin\gamma\right) + \left(\cos\gamma\sin\alpha\sin\beta - \cos\alpha\sin\gamma\right)\cdot$$
$$\left\{\cos\alpha\cos\gamma\left(c_{55}^{e}r_{z} + c_{53}^{e}\sin\beta\right) + \sin\alpha\left[-c_{55}^{e}r_{y}\cos\beta + \left(c_{53}^{e} + c_{55}^{e}r_{z}\sin\beta\right)\sin\gamma\right]\right\} +$$
$$\left(\cos\alpha\cos\gamma\sin\beta + \sin\alpha\sin\gamma\right)\cdot$$
$$\left\{\cos\gamma\sin\alpha\left(-c_{66}^{e}r_{z} + c_{62}^{e}\sin\beta\right) - \cos\alpha\left[c_{66}^{e}r_{y}\cos\beta + \left(c_{62}^{e} - c_{66}^{e}r_{z}\sin\beta\right)\sin\gamma\right]\right\}$$
(5.17)

$$\overline{c}_{51}^{e} = c_{44}^{e}\cos\beta\sin\gamma\left(r_{y}\sin\beta + r_{z}\cos\beta\sin\gamma\right) + \left(\cos\alpha\cos\gamma + \sin\alpha\sin\beta\sin\gamma\right)\cdot$$
$$\left\{\cos\alpha\cos\gamma\left(c_{55}^{e}r_{z} + c_{53}^{e}\sin\beta\right) + \sin\alpha\left[-c_{55}^{e}r_{y}\cos\beta + \left(c_{53}^{e} + c_{55}^{e}r_{z}\sin\beta\right)\sin\gamma\right]\right\} +$$
$$\left(-\cos\gamma\sin\alpha + \cos\alpha\sin\beta\sin\gamma\right)\cdot$$
$$\left\{\cos\gamma\sin\alpha\left(-c_{66}^{e}r_{z} + c_{62}^{e}\sin\beta\right) - \cos\alpha\left[c_{66}^{e}r_{y}\cos\beta + \left(c_{62}^{e} - c_{66}^{e}r_{z}\sin\beta\right)\sin\gamma\right]\right\}$$
(5.18)

$$\overline{c}_{32}^{e} = -c_{11}^{e}\cos\beta\sin\beta\sin\gamma - c_{44}^{e}\cos\beta\left(r_{z}\cos\beta\cos\gamma + r_{x}\sin\beta\right)\left(r_{y}\cos\gamma - r_{x}\sin\gamma\right) +$$
$$\cos\beta\sin\alpha\left\{\cos\alpha\left[c_{62}^{e}r_{x}\cos\beta + \cos\gamma\left(c_{22}^{e} - c_{62}^{e}r_{z}\sin\beta\right)\right] + \sin\alpha\left(-c_{62}^{e}r_{z} + c_{22}^{e}\sin\beta\right)\sin\gamma\right\} +$$
$$\cos\alpha\cos\beta\left[c_{53}^{e}r_{x}\cos\beta\sin\alpha - \cos\gamma\sin\alpha\left(c_{33}^{e} + c_{53}^{e}r_{z}\sin\beta\right) + \cos\alpha\left(c_{53}^{e}r_{z} + c_{33}^{e}\sin\beta\right)\sin\gamma\right] +$$
$$\left\{\cos\alpha\left[c_{66}^{e}r_{x}\cos\beta + \cos\gamma\left(c_{62}^{e} - c_{66}^{e}r_{z}\sin\beta\right)\right] + \sin\alpha\left(-c_{66}^{e}r_{z} + c_{62}^{e}\sin\beta\right)\sin\gamma\right\}\cdot$$
$$\left[\cos\gamma\left(r_{x}\sin\alpha + r_{y}\cos\alpha\sin\beta\right) + \left(r_{y}\sin\alpha - r_{x}\cos\alpha\sin\beta\right)\sin\gamma\right] +$$
$$\left[c_{55}^{e}r_{x}\cos\beta\sin\alpha - \cos\gamma\sin\alpha\left(c_{53}^{e} + c_{55}^{e}r_{z}\sin\beta\right) + \cos\alpha\left(c_{55}^{e}r_{z} + c_{53}^{e}\sin\beta\right)\sin\gamma\right]\cdot$$
$$\left[\sin\alpha\sin\beta\left(r_{y}\cos\gamma - r_{x}\sin\gamma\right) - \cos\alpha\left(r_{x}\cos\gamma + r_{y}\sin\gamma\right)\right]$$
(5.19)

$$\overline{c}_{42}^{e} = -c_{44}^{e}\cos\beta\cos\gamma\left(r_{z}\cos\beta\cos\gamma + r_{x}\sin\beta\right) + \left(\cos\alpha\cos\gamma\sin\beta + \sin\alpha\sin\gamma\right)\cdot$$
$$\left\{\cos\alpha\left[c_{66}^{e}r_{x}\cos\beta + \cos\gamma\left(c_{62}^{e} - c_{66}^{e}r_{z}\sin\beta\right)\right] + \sin\alpha\left(-c_{66}^{e}r_{z} + c_{62}^{e}\sin\beta\right)\sin\gamma\right\} +$$
$$\left(\cos\gamma\sin\alpha\sin\beta - \cos\alpha\sin\gamma\right)\cdot$$
$$\left[c_{55}^{e}r_{x}\cos\beta\sin\alpha - \cos\gamma\sin\alpha\left(c_{53}^{e} + c_{55}^{e}r_{z}\sin\beta\right) + \cos\alpha\left(c_{55}^{e}r_{z} + c_{53}^{e}\sin\beta\right)\sin\gamma\right]$$
(5.20)

$$\overline{c}_{52}^e = -c_{44}^e \cos\beta\left(r_z \cos\beta \cos\gamma + r_x \sin\beta\right)\sin\gamma + \left(-\cos\gamma \sin\alpha + \cos\alpha \sin\beta \sin\gamma\right)\cdot$$
$$\left\{\cos\alpha\left[c_{66}^e r_x \cos\beta + \cos\gamma\left(c_{62}^e - c_{66}^e r_z \sin\beta\right)\right] + \sin\alpha\left(-c_{66}^e r_z + c_{62}^e \sin\beta\right)\sin\gamma\right\} +$$
$$\left(\cos\alpha \cos\gamma + \sin\alpha \sin\beta \sin\gamma\right)\cdot$$
$$\left[c_{55}^e r_x \cos\beta \sin\alpha - \cos\gamma \sin\alpha\left(c_{53}^e + c_{55}^e r_z \sin\beta\right) + \cos\alpha\left(c_{55}^e r_z + c_{53}^e \sin\beta\right)\sin\gamma\right] \tag{5.21}$$

$$\overline{c}_{63}^e = \frac{1}{2}\cos\beta\left\{\left(c_{62}^e + c_{53}^e\right)\cos\beta \sin 2\alpha + \left[2c_{44}^e - c_{55}^e - c_{66}^e + \left(c_{55}^e - c_{66}^e\right)\cos 2\alpha\right]\cdot\right.$$
$$\left.\sin\beta\left(-r_y \cos\gamma + r_x \sin\gamma\right) - \left(c_{55}^e - c_{66}^e\right)\sin 2\alpha\left(r_x \cos\gamma + r_y \sin\gamma\right)\right\} \tag{5.22}$$

$$\overline{c}_{64}^e = \cos\beta\left[\cos\gamma\left(-c_{44}^e + c_{66}^e \cos^2\alpha + c_{55}^e \sin^2\alpha\right)\sin\beta + \left(-c_{55}^e + c_{66}^e\right)\cos\alpha \sin\alpha \sin\gamma\right] \tag{5.23}$$

$$\overline{c}_{65}^e = \cos\beta\left[\left(c_{55}^e - c_{66}^e\right)\cos\alpha \cos\gamma \sin\alpha + c_{66}^e \cos^2\alpha \sin\beta \sin\gamma + \left(-c_{44}^e + c_{55}^e \sin^2\alpha\right)\sin\beta \sin\gamma\right] \tag{5.24}$$

These set of equations can be solved by considering Eq. (5.22) first because β is the only dominant angular variable and the results are given as

$$\overline{c}_{63}^e = 0 \Leftrightarrow \begin{bmatrix} \beta = 90° \\ \alpha = 0° \text{ and } \beta = 0°,\ 180° \quad ; \quad \forall \gamma,\ r_x,\ r_y,\ r_z \\ \alpha = 90° \text{ and } \beta = 0°,\ 180° \end{bmatrix} \tag{5.25}$$

Here, the rotation angle about the X'' axis, α, varies from 0° to 90° because of the symmetrical design of the flexure elements. Eq. (5.25) shows that there are three possible cases for $\overline{c}_{63}^e = 0$ with the four remaining variables (γ, r_x, r_y, r_z) being arbitrary values.

First, the case with $\beta = 90°$ is considered. With every component within the compliance matrix of the flexure element having a specific value as shown in Eq. (5.10), six equations from Eq. (5.16) to Eq. (5.21) are always different from zero with any value of γ, r_x, r_y, and r_z. Hence, $\beta = 90°$ is not a feasible solution.

Next, considering the second case with $\alpha = 0°$ and $\beta = 0°$ or $180°$, the following results can be obtained

$$\bar{c}_{31}^{e} = \pm r_{z} \left\{ \mp c_{55}^{e} r_{x} \cos^{2}\gamma \mp c_{44}^{e} r_{x} \sin^{2}\gamma + \cos\gamma \left[c_{53}^{e} + \left(\pm c_{44}^{e} \mp c_{55}^{e} \right) r_{y} \sin\gamma \right] \right\}$$

$$\bar{c}_{41}^{e} = \left(c_{44}^{e} - c_{55}^{e} \right) r_{z} \cos\gamma \sin\gamma$$

$$\bar{c}_{51}^{e} = r_{z} \left(c_{55}^{e} \cos^{2}\gamma + c_{44}^{e} \sin^{2}\gamma \right)$$

$$\bar{c}_{32}^{e} = \pm r_{z} \left[\mp c_{44}^{e} r_{y} \cos^{2}\gamma + \left(\pm c_{44}^{e} \mp c_{55}^{e} \right) r_{x} \cos\gamma \sin\gamma + \sin\gamma \left(c_{53}^{e} \mp c_{55}^{e} r_{y} \sin\gamma \right) \right] \qquad (5.26)$$

$$\bar{c}_{42}^{e} = -r_{z} \left(c_{44}^{e} \cos^{2}\gamma + c_{55}^{e} \sin^{2}\gamma \right)$$

$$\bar{c}_{52}^{e} = \left(-c_{44}^{e} + c_{55}^{e} \right) r_{z} \cos\gamma \sin\gamma$$

$$\bar{c}_{64}^{e} = \bar{c}_{65}^{e} = 0$$

Note that the upper signs of $\pm$ and $\mp$ in Eq. (5.26) correspond with $\alpha = 0°$, $\beta = 0°$ and the lower signs correspond with $\alpha = 0°$, $\beta = 180°$. Assuming that if $\bar{c}_{51}^{e}$ in Eq. (5.26) is equal to zero, it is observed that only r_{z} needs to be zero with γ being any value. With $r_{z} = 0$, all the remaining equations in Eq. (5.26) will also be equal to zero. Hence, $r_{z} = 0$, $\alpha = 0°$, $\beta = 0°$ or $180°$, is a solution to obtain a CPMs with decoupled motions.

Similarly, for the case with $\alpha = 90°$, $\beta = 0°$ or $180°$, it can be shown that this is also a possible solution. In summary, the two feasible solutions found from Eq. (5.25) with $r_{z} = 0$ are

$$\begin{bmatrix} \alpha = 0° \text{ and } \beta = 0°, \ 180° \\ \alpha = 90° \text{ and } \beta = 0°, \ 180° \end{bmatrix} ; \quad \forall \gamma, \ r_{x}, \ r_{y} \qquad (5.27)$$

Eq. (5.27) provides the design criteria for the orientations and positions of flexure elements that need to be satisfied to design a CPM with fully-decoupled motions. Figure 5.3 illustrates the desired orientation of the flexure elements about the X'' and Y'' axes with various orientations about the Z'' axis. It can be concluded that to achieve fully-decoupled motion capability, two conditions must be met. First, the design of each limb could be formed by either

one or a series of flexure elements with their orientations being similar to those illustrated in Figure 5.3. Second, these flexure elements must be located in the $X'Y'$ plane ($r_z = 0$) while the remaining distance parameters (r_x and r_y) between two neighboring flexure elements can be arbitrary.
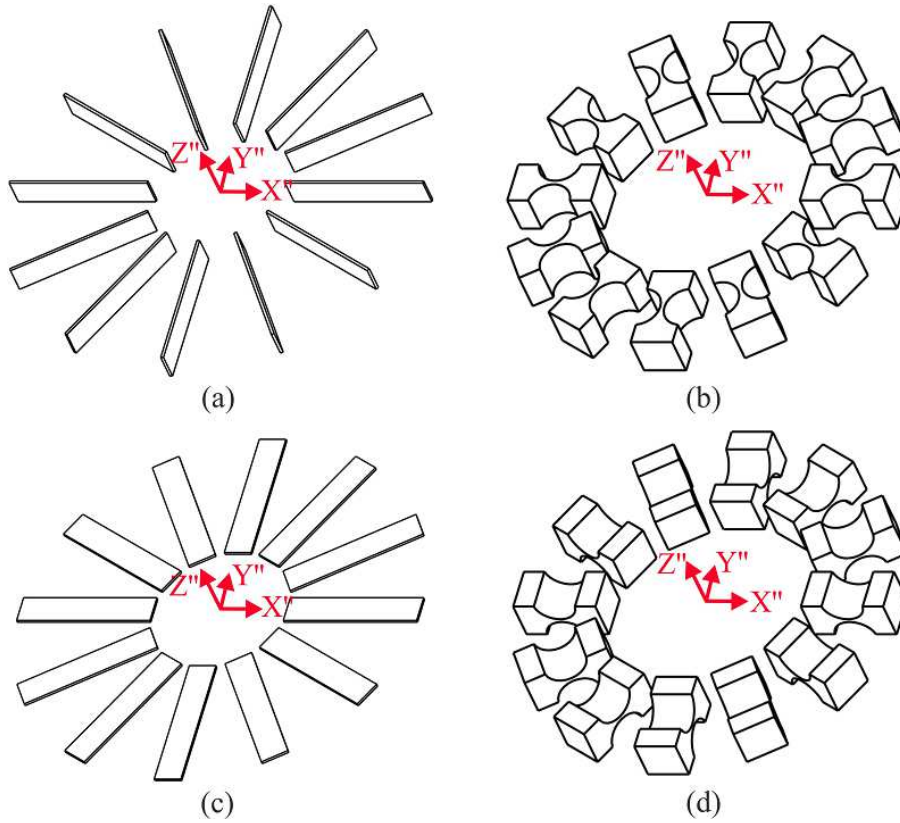
Figure 5.3: Orientations of the flexure elements in fully-decoupled motion CPMs; (a) beam-type and (b) notch-type with $\alpha = 0°$, $\beta = 0°$ or $180°$, $r_z = 0$ respectively. (c) Beam-type and (d) notch-type with $\alpha = 90°$, $\beta = 0°$ or $180°$, $r_z = 0$ respectively.

5.4 Stiffness Modeling of CPMs Containing Two Reflecting Serial Flexure Chains in a Limb

In the previous Section, the stiffness modeling of a popular CPM, with each limb consisting of a single serial flexure chain, is presented. However, there are many CPMs have two reflecting (or symmetrical) serial flexure chains in a limb as shown in Figure 5.4 [49, 74, 75, 121, 135, 136]. This configuration is also used to model CPMs in the proposed beam-based

method. The limb will still possess the stiffness property of the general CPM as presented in Section 5.2 but the motion property will be characterized by the parallel configuration of two flexure chains. In this Section, the analysis of such a limb configuration is presented.
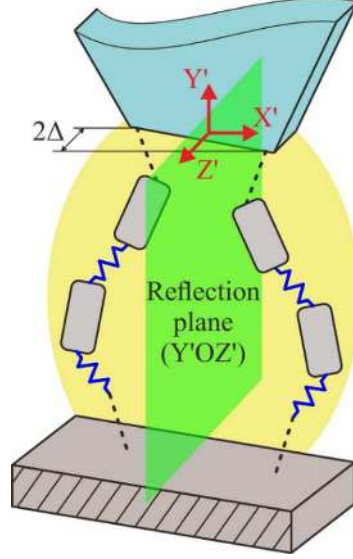
Figure 5.4: Construction of a CPM containing two reflecting serial flexure chains in a limb.

From the literatures, the double flexure chains are either on the same plane or having an offset distance of 2Δ along the Z' axis as shown in Figure 5.4. The stiffness matrix of each limb is expressed as

$$K^l = \left(\sum_{j=1}^{n} J_{(+\Delta)} C^{sc} J_{(+\Delta)}^T \right)^{-1} + \left(\sum_{j=1}^{n} J_{(-\Delta)} H C^{sc} H^T J_{(-\Delta)}^T \right)^{-1} \tag{5.28}$$

where H is the reflection matrix about the $Y'Z'$ plane given in Eq. (5.29), and $J_{(+\Delta)}$ and $J_{(-\Delta)}$ represent the offset matrices used to shift the original flexure chain, and the reflecting flexure chain along the Z' axis distances of $+\Delta$ and $-\Delta$ respectively as given in Eq. (5.30).

$$H = \begin{bmatrix} -1 & 0 & 0 & 0 & 0 & 0 \\ 0 & 1 & 0 & 0 & 0 & 0 \\ 0 & 0 & 1 & 0 & 0 & 0 \\ 0 & 0 & 0 & -1 & 0 & 0 \\ 0 & 0 & 0 & 0 & 1 & 0 \\ 0 & 0 & 0 & 0 & 0 & 1 \end{bmatrix} \qquad (5.29)$$

$$J_{(\pm \Delta)} = \begin{bmatrix} 1 & 0 & 0 & 0 & 0 & 0 \\ 0 & 1 & 0 & 0 & 0 & 0 \\ 0 & 0 & 1 & 0 & 0 & 0 \\ 0 & \pm \Delta & 0 & 1 & 0 & 0 \\ \mp \Delta & 0 & 0 & 0 & 1 & 0 \\ 0 & 0 & 0 & 0 & 0 & 1 \end{bmatrix} \qquad (5.30)$$

Here, C^{sc} is the compliance matrix of a serial flexure chain calculated by Eq. (5.9). The results from Section 5.3 are used to analyze the stiffness property of CPMs having two reflecting flexure chains in a limb. After substituting Eqs. (5.9), (5.29) and (5.30) into Eq. (5.28), the results show that the motion-decoupling capability can only be achieved when the offset distance $2\Delta = 0$. The offset distance can be considered as the translation component along the Z axis of each flexure element (r_{z_j}) that can lead to coupled motions. Most importantly, to achieve fully-decoupled output motions, C^{sc} must be in the following form

$$C^{sc} = \begin{bmatrix} c_{11}^{sc} & & & & & \\ c_{21}^{sc} & c_{22}^{sc} & & & SYM & \\ 0 & 0 & c_{33}^{sc} & & & \\ 0 & 0 & c_{43}^{sc} & c_{44}^{sc} & & \\ 0 & 0 & c_{53}^{sc} & c_{54}^{sc} & c_{55}^{sc} & \\ c_{61}^{sc} & c_{62}^{sc} & 0 & 0 & 0 & c_{66}^{sc} \end{bmatrix} \qquad (5.31)$$

If there is an offset between the flexure chains, then the six components, i.e., k_{31}^{l}, k_{41}^{l}, k_{51}^{l}, k_{32}^{l}, k_{42}^{l} and k_{52}^{l} in K^{l} calculated by Eq. (5.28), will be non-zeros. In this case, the five non-

diagonal components within the stiffness matrix of the CPM as expressed in Eq. (5.5) will be present.

5.5 Case Study

In Chapter 3, a 3-DOF spatial-motion ($\theta_X - \theta_Y - Z$) CPM has been synthesized. However, the C-T beams in each limb are not located in the same plane because they are constrained to have no intersection to simplify the optimization process. The small offset between two mirrored C-T beams is the reason that leads to coupled motions for the CPM as proven in Section 5.4 since it generates a translation along the Z axis. The coupled motions of the synthesized 3-DOF CPM are demonstrated in Eqs. (3.19) and (4.4) where the 6×6 compliance matrix of the entire CPM is a non-diagonal matrix in the form of Eq. (5.5). The five non-diagonal components within the compliance matrix will generate undesired parasitic motions. In this Section, the synthesis of a fully decoupled-motion 3-DOF ($\theta_X - \theta_Y - Z$) CPM will be demonstrated using the formulated design criteria.

a) *Design of the decoupled-motion 3-DOF ($\theta_X - \theta_Y - Z$) CPM*

The design domain is the same as before with the structure of CPM consisting of two reflecting serial flexure chains in each limb. Using the results of Section 5.4, to have fully-decoupled motions, the Bezier center-curves of C-T beams must be located in the $X'Y'$ plane (see Figure 3.2b). In addition, the orientation of the C-T beams must be parallel or perpendicular to the $X'Y'$ plane, corresponding to two possible cases of the twist angles, i.e., $\alpha_A = \alpha_B = 0°$ and $\alpha_A = \alpha_B = 90°$ (see Figure 3.2a). With the defined design constraints for decoupled motions, the stiffness and dynamic optimizations processes are carried out in sequence and the final design of the CPM is shown in Figure 5.5.
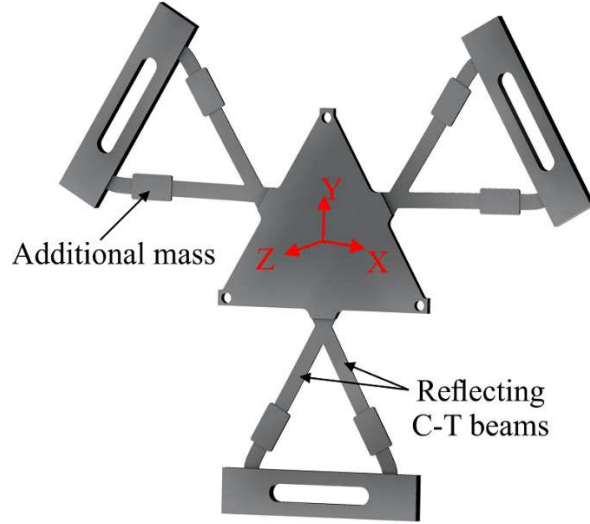
Figure 5.5: Optimized 3-DOF ($\theta_X - \theta_Y - Z$) CPM with decoupled motions.

It is seen that all C-T beams locate in the *XY* plane and two reflecting C-T beams in each limb intersect each other at the free ends and thus creating a flat V-shape flexure that satisfies the criteria for achieving decoupled motions. This CPM is able to produce the targeted dynamic response of 100 Hz as the previous design, and the fully-decoupled output motions are demonstrated by its diagonal compliance matrix, $\hat{C}^{\text{3-DOF}}$, written as

$$
\hat{C}^{\text{3-DOF}} = \begin{bmatrix} 5.53e-8 & & & & & \\ 0 & 5.53e-8 & & & SYM & \\ 0 & 0 & 1.99e-4 & & & \\ 0 & 0 & 0 & 1.32e-1 & & \\ 0 & 0 & 0 & 0 & 1.32e-1 & \\ 0 & 0 & 0 & 0 & 0 & 2.33e-4 \end{bmatrix} \tag{5.32}
$$

b) *Energy of motion*

Here, the decoupled motions are proven based on energy approach where work done is used to represent the energy of a motion. First, Eqs. (3.6) and (3.7) can be rewritten as

$$
W_i = \int_0^{U_i} P_i dU_i = \int_0^{U_i} K_{ii} U_i dU_i = \frac{1}{2} K_{ii} U_i^2 \tag{5.33}
$$

Assuming the non-diagonal components within the stiffness matrix of the CPM exist, Eq. (5.33) can be modified to represent the total energy in the ith direction as

$$W_i = \sum_{j=1}^{6} \frac{1}{2} K_{ij} U_j^2 \qquad (5.34)$$

Referring to Eq. (5.34), W_i is the combination of the energy of the desired motion (determined by K_{ii} and U_i) and the energies of the undesired parasitic motions (determined by K_{ij} and U_j, where $j \neq i$). Here, a motion is considered as decoupled if the energies of the parasitic motions have minor contribution over the total energy.

c) *Experiment*

The decoupled motions of the synthesized CPM are experimentally evaluated to demonstrate the correctness of the proposed design criteria. With the stiffness/compliance matrix of the CPM being symmetrical, only five non-diagonal components possibly exist as shown in Eq. (5.5). For this case study, only the translation along the Z axis is evaluated. In particular, the component k_{63}^m, which represents the parasitic rotation about the Z axis, will be shown to be nearly zero. Moreover, the parasitic motions along the X and Y axes are also experimentally measured to demonstrate that they are very small and have no effect on the desired motion along the Z axis, even they are zeros in theory.

Based on Eq. (5.5), when applying a force along the Z axis, a parasitic rotation about the same axis could be generated. Figure 5.6 shows the experimental setup to measure the parasitic motions when applying an input displacement along the Z axis. A solid block that rigidly mounted to the end effector is used to transmit the motion along the Z axis from the micrometer to the CPM. The parasitic motions along the X and Y axes, and about the Z axis are detected by three individual capacitive sensors respectively. The sensors measure the distances

between their sensing areas to the surfaces of the solid block. The experiment is conducted five

times and Figure 5.7 plots the ratio between the energy of each parasitic motion and the total

energy generated along the *Z* axis.
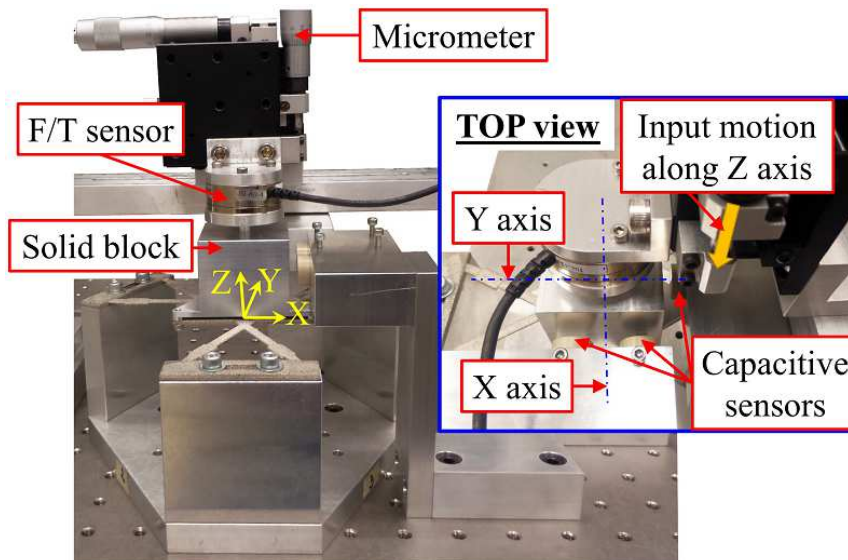
Figure 5.6: Experimental setup for measuring the parasitic motions when applying an input displacement along the *Z* axis.
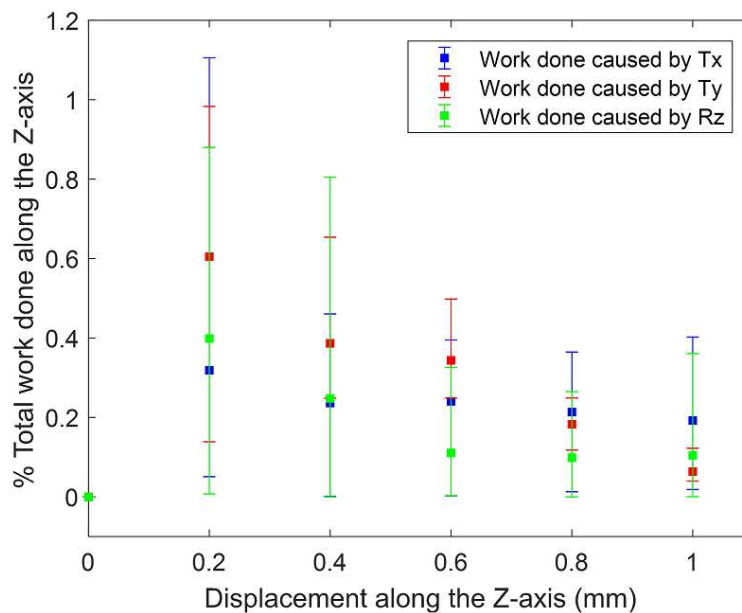
Figure 5.7: The ratios between the energies of parasitic motions over the total energy along the *Z* axis.

From Figure 5.7, it is seen that the highest energy of the parasitic motions only

contributes less than 1% over the total energy along the *Z* axis. The results show that the input

energy (along the Z axis) is mainly used to create the desired motions while the energies that generate the parasitic motions are minimal. The existence of parasitic motions along the X and Y axes could be due to the Abbe error caused by the fabrication tolerances and the assembly imperfection, i.e., the surfaces of the solid block are not ideally perpendicular to the measuring directions of the capacitive sensors. In general, the reading from the sensor, ε, affected by the Abbe error can be estimated based on the slope angle of the surface of the block, ψ , and the input displacement along the Z axis, δ_Z , given as

$$\tan \psi = \frac{\varepsilon}{\delta_Z} \tag{5.35}$$

By assuming that the slope angle of the surface of the target block is ~0.2°, the readings from the sensor that correspond with the input displacements calculated by Eq. (5.35) are listed in Table 5.1. These results show that a slight angular misalignment of 0.2° is enough to cause the capacitive sensors to return the Abbe error as the parasitic motions instead. Hence, it is possible that the Abbe errors have contributed to the readings even though the CPM may not produce any parasitic motion. The experimental results show that the synthesized CPM is capable of providing a decoupled motion along the Z axis.

Table 5.1: Reading of capacitive sensors caused by Abbe error.

Displacement along the Z axis	Sensor's reading
200 μm	0.698 μm
400 μm	1.396 μm
600 μm	2.094 μm
800 μm	2.793 μm
1000 μm	3.491 μm

5.6 Discussion

In order to achieve fully-decoupled motions, a CPM must have a 6 × 6 diagonal stiffness/compliance matrix whereby all non-diagonal components are zero. Due to the property of the parallel architecture, the stiffness matrix of a CPM can be calculated based on the stiffness matrices of its three limbs. However, the stiffness matrix of each limb cannot be derived directly since it can be constructed by one or two serial chains; each formed by a number of flexure elements and rigid links, and thus its characteristic is defined by its compliance. Due to the challenges in converting between the stiffness and compliance matrices, existing CPMs fail to analyze their motion property analytically. To overcome this limitation and most importantly for a CPM to obtain fully-decoupled-motion characteristics, some conditions for the compliance matrix of a general CPM having a single serial flexure chain, i.e., Eq. (5.13), and double serial flexure chains, i.e., Eq. (5.31) in a limb are provided in this Chapter.

The effectiveness of the proposed design criteria has been demonstrated in Section 5.5, an improved designed of the synthesized 3-DOF ($\theta_X - \theta_Y - Z$) CPM presented in Chapter 3 has been developed. The decoupled-motion capability of the new design is verified by experimental investigation. For the CPM synthesized previously with $\Delta \neq 0$, the compliance matrix, $\overline{C}'^{\text{3-DOF}}$, has five non-diagonal components as shown in Figure 5.8a. For the improved CPM with $\Delta = 0$, the compliance matrix, $\hat{C}^{\text{3-DOF}}$, only contains diagonal components as shown in Figure 5.8b. In summary, the motion property of CPMs having two reflecting flexure chains in a limb has been demonstrated. CPMs having an offset distance in the Z axis between two flexure chains will generate coupled motions while the others having both flexure chains located in the same plane will generate decoupled motions.

$$\bar{C}'^{\text{3-DOF}} = \begin{bmatrix} 3.21e-8 & & & & & \\ 0 & 3.21e-8 & & & SYM & \\ 0 & 0 & 8.98e-5 & & & \\ -3.31e-6 & 7.84e-8 & 0 & 3.05e-2 & & \\ -7.84e-8 & -3.31e-6 & 0 & 0 & 3.05e-2 & \\ 0 & & 4.28e-6 & 0 & 0 & 1.50e-4 \end{bmatrix}$$

(a)

$$\hat{C}^{\text{3-DOF}} = \begin{bmatrix} 5.53e-8 & & & & & \\ 0 & 5.53e-8 & & & SYM & \\ 0 & 0 & 1.99e-4 & & & \\ 0 & 0 & 0 & 1.32e-1 & & \\ 0 & 0 & 0 & 0 & 1.32e-1 & \\ 0 & 0 & 0 & 0 & 0 & 2.33e-4 \end{bmatrix}$$
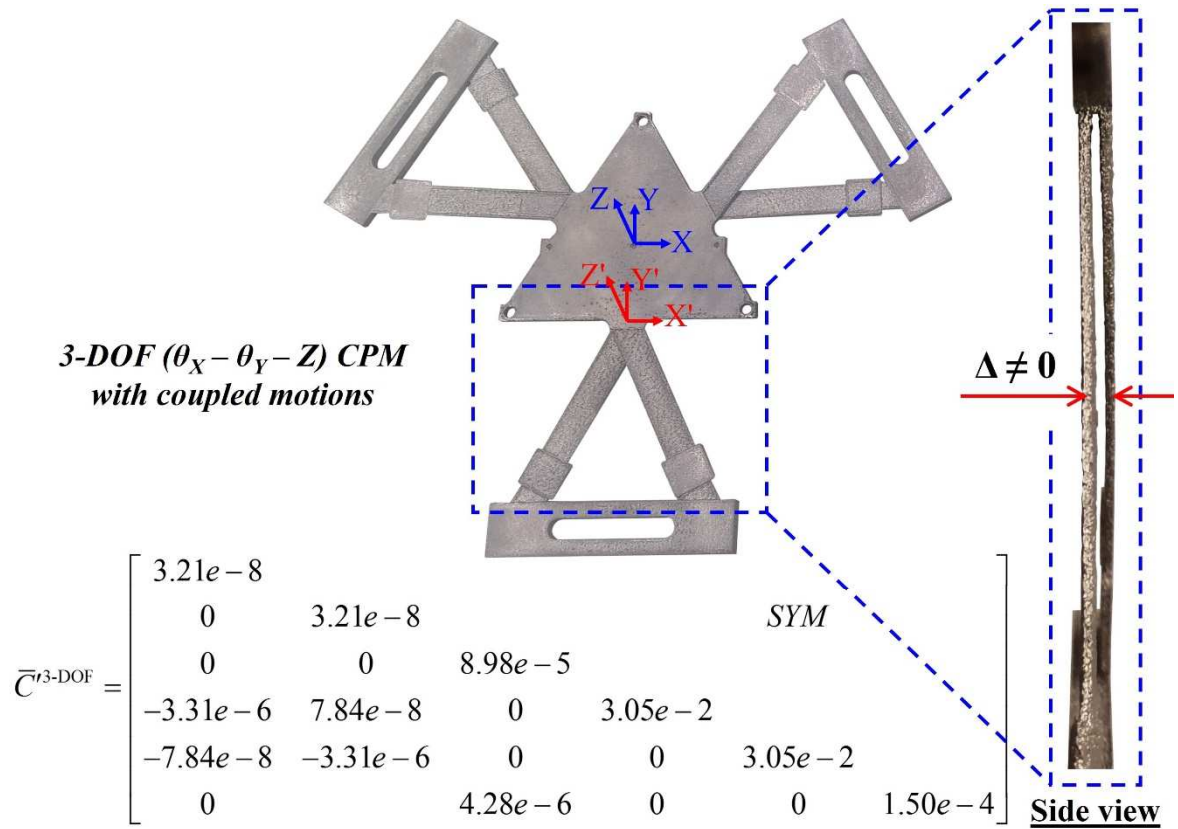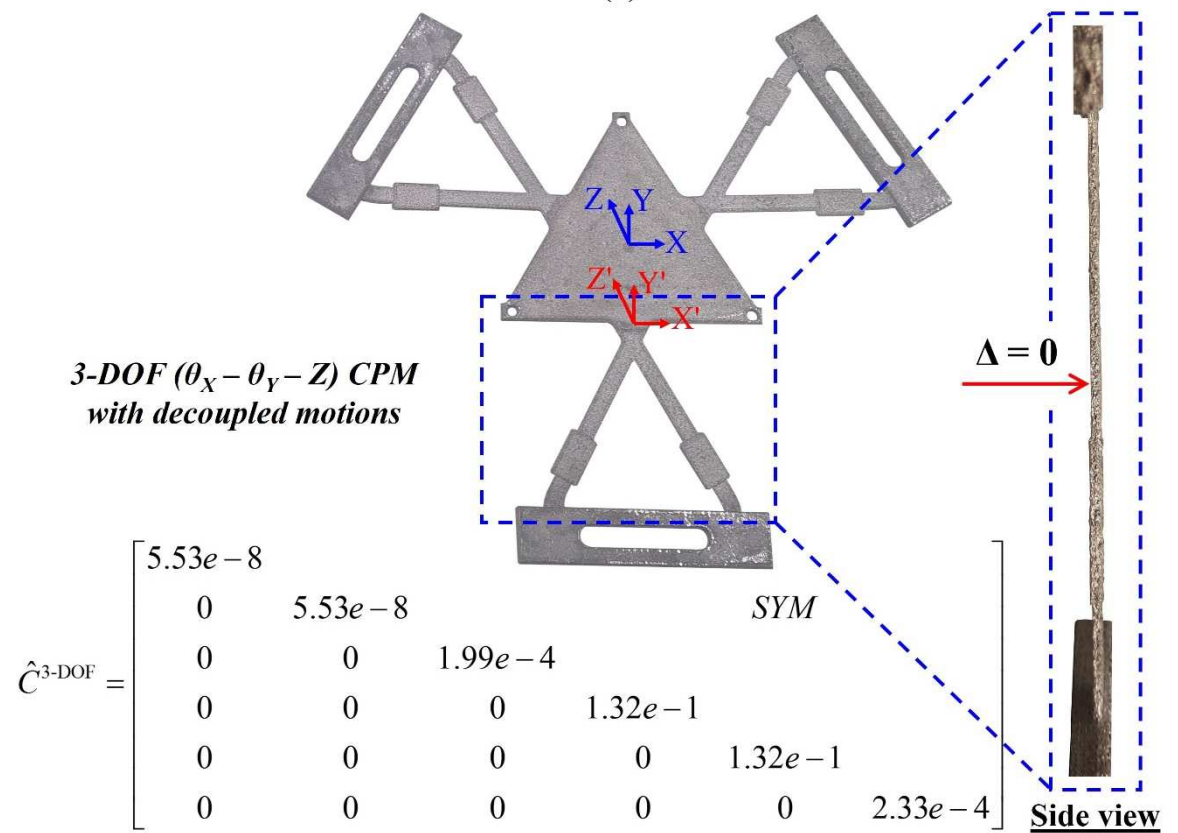
(b)

Figure 5.8: 3-DOF ($\theta_X - \theta_Y - Z$) CPMs synthesized by beam-based method (a) with offset distance and (b) without offset distance between two serial flexure chains in a limb.

107

Additionally, the findings in this Chapter are applicable for any design methodology. Thus, the motion property of existing CPMs synthesized by various approaches, e.g., traditional rigid-body-replacement approach [40-42, 46, 123-126], constraint-based approach [134, 135] and topology/structural optimization approach [74, 75, 121], can be analyzed with the proposed criteria. In particular, developed 3-DOF ($X - Y - \theta_Z$) CPMs [40-42, 46, 74, 75, 99, 121, 123-128] and 6-DOF CPMs [135-137] having planar structures, i.e., all flexure joints are located in the global XY plane with orientation about the X'' axis being 0° or 90°, are able to produce fully-decoupled motions. On the other hand, other designs which flexure elements are not distributed in the same XY plane, such as 3-DOF ($\theta_X - \theta_Y - Z$) CPMs [17, 83, 129-134] and 6-DOF CPMs [48, 49], will generate coupled motions.

5.7 Summary

This Chapter presents the fundamental design criteria for synthesizing CPMs with fully-decoupled-motion capability regardless of the desired DOF. The stiffness characteristics of CPMs have been mathematically modeled and the design criteria are obtained through analytical solutions. A relationship between the stiffness and compliance matrices of the limb has been found to govern the variety structures of each limb in order to obtain fully-decoupled-motion capability. The results suggest that the flexure elements in each limb must be distributed in the same plane with the end effector to fulfill the decoupled-motion requirements. In the case where each limb contains two parallel reflecting (or symmetrical) flexure chains, such requirements are valid if both flexure chains are located in the same plane with no offset distance. To demonstrate and validate the design criteria and conditions, an improved design of 3-DOF ($\theta_X - \theta_Y - Z$) CPM with decoupled motions has been developed and the decoupling-motion capability of the new design is also experimentally investigated. The obtained results

suggest that the CPM can produce decoupled output-motions since nearly all input energy is used to generate the desired motion.

Because the decoupled-motion 3-DOF ($\theta_X - \theta_Y - Z$) CPM is proposed in this Chapter as a case study, only the motion characteristics along the Z axis is evaluated. The design criteria will be further validated in the next Chapter through the experimental investigations on all the possible parasitic motions presented.

CHAPTER 6
SYNTHESIS AND EVALUATION OF A 6-DOF CPM WITH DECOUPLED MOTIONS

In this Chapter, the synthesis process of a novel 6-DOF CPM, the most complex form of CPM, will be presented. The design criteria and beam-based method proposed previously are applied to create a CPM with optimized mechanical properties and fully-decoupled motions. Based on the results from Chapter 5, the center curves of the C-T beams in each limb are pre-defined in the global *XY* plane. The geometry and orientation of the C-T beams will then be optimized.

The 6-DOF CPM is desired to have a large workspace by minimizing the actuating stiffness, the first resonance frequency must be at least 100 Hz and the differences between neighbor modes are required to be large to improve the overall dynamic characteristic. The design space of each limb is assigned as 50×50 mm^2.

6.1 Optimization Processes

In order to generate six motions at the end effector, appropriate geometry of the C-T beams is determined by the stiffness optimization. The main purpose of this step is to minimize the six-primary stiffness of the CPM. As the C-T beams must locate in the *XY* plane to create fully-decoupled motions, ten design variables need to be found during the stiffness optimization process. Eight variables represent the coordinates (*X* and *Y* components) of the four control points defining the C-T beam, and 2 variables represent the orientation of the beam

which can be 0° or 90°. The objective function for the 6-DOF CPM can be derived based on the works done by the six motions and corresponding loads, written as

$$\text{maximize } g = \prod_{i=1}^{6} W_i = \prod_{i=1}^{6} \left(\frac{1}{2} \frac{P_i^2}{K_{ii}} \right) = \kappa \cdot \prod_{i=1}^{6} \frac{1}{K_{ii}},$$
$$\text{where } \kappa = \prod_{i=1}^{6} \frac{P_i^2}{2} \tag{6.1}$$

where W_i represents the work done caused by the load P_i, and K_{ii} denotes the diagonal component within the 6 × 6 stiffness matrix of the CPM that corresponds to P_i. Here, κ is a coefficient factor and has no effect to the optimization result so that it can be eliminated. As a result, Eq. (6.1) can be simplified as

$$\text{minimize } g' = \prod_{i=1}^{6} K_{ii} \tag{6.2}$$

Eq. (6.2) is solved by GA and the obtained optimized geometry of a pair of C-T beams in a limb is illustrated in Figure 6.1.
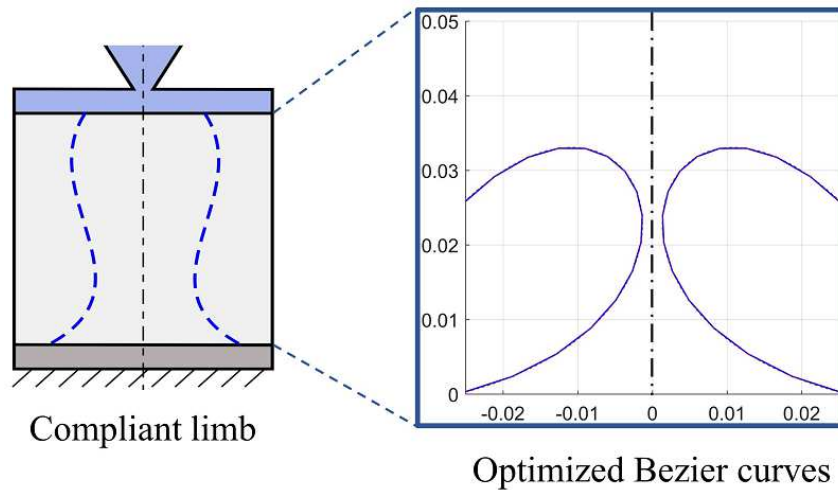
Figure 6.1: Optimized geometry of two reflecting C-T beams in a compliant limb.

The dynamic optimization is then carried out to determine the cross-sectional area of the C-T beams, the size of the end effector as well as the distribution of additional masses at suitable positions. This step can be done by solving the dynamic objective function represented by a set of two equations as shown in Eq. (6.3).

$$
\begin{cases}
\text{minimize} & \left(\left| F_d - F_1 \right| - \sum_{r=1}^{5} \left| F_{r+1} - F_r \right| \right) \\
\text{minimize} & \left(g' \right)
\end{cases}
\tag{6.3}
$$

Here, the first equation is to find the minimum of the difference between two terms, i.e., $\left| F_d - F_1 \right|$ and $\sum_{r=1}^{5} \left| F_{r+1} - F_r \right|$. This equation achieves the smallest value if the first term, $\left| F_d - F_1 \right|$, is minimal while the second term, $\sum_{r=1}^{5} \left| F_{r+1} - F_r \right|$, is maximal. In particular, the first resonance frequency, F_1, of the CPM is enhanced to the desired value ($F_d = 100$ Hz) and the total difference between two neighbor vibration modes represented by $\sum_{r=1}^{5} \left| F_{r+1} - F_r \right|$ is maximal. In addition, the high flexibility of the entire CPM is maintained by the second equation. As a result, the CPM is able to achieve optimal stiffness performance, targeted dynamic behavior with the vibration modes being separated between each other to simplify subsequent control and operation.

The final structure of the entire CPM after the dynamic optimization process is shown in Figure 6.2. Six primary resonance frequencies of the CPM are represented by the frequency vector, $F^{\text{6-DOF}}$, while the stiffness characteristic is represented by the compliance matrix, $C^{\text{6-DOF}}$. The results of $C^{\text{6-DOF}}$ and $F^{\text{6-DOF}}$ are given in Eqs. (6.4) and (6.5) respectively.
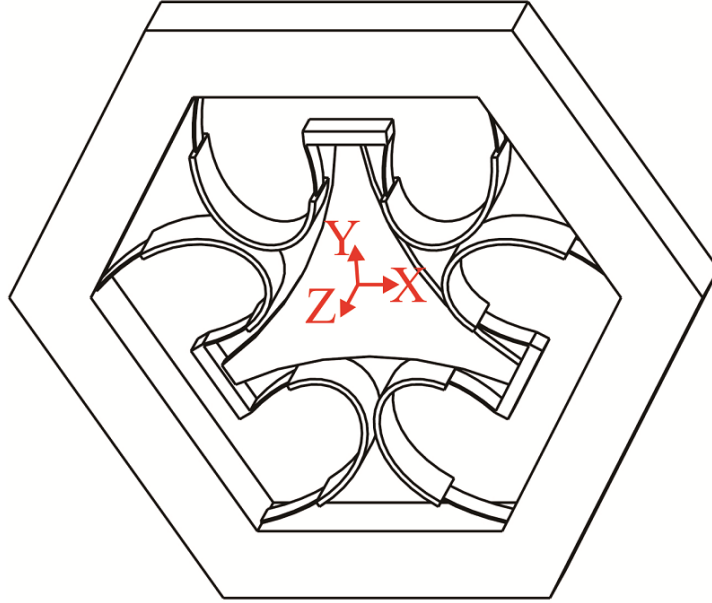
Figure 6.2: Optimized design of the 6-DOF CPM.

$$C^{\text{6-DOF}} = \begin{bmatrix} 3.67e-5 & & & & & \\ 0 & 3.67e-5 & & & SYM & \\ 0 & 0 & 9.70e-5 & & & \\ 0 & 0 & 0 & 3.06e-2 & & \\ 0 & 0 & 0 & 0 & 3.06e-2 & \\ 0 & 0 & 0 & 0 & 0 & 3.47e-2 \end{bmatrix} \qquad (6.4)$$

$$F^{\text{6-DOF}} = \begin{bmatrix} \Delta_Z & \Delta_X & \Delta_Y & R_Z & R_X & R_Y \\ 100 & 148 & 148 & 169 & 340 & 340 \end{bmatrix} \qquad (6.5)$$

It is seen from Eq. (6.4), the synthesized CPM is able to produce fully-decoupled motions since its compliance matrix only contains diagonal components. The six vibration modes correspond to the resonance frequencies of 6-DOF generated by the CPM are represented by the subscripts above the matrix components in Eq. (6.5). With Ti6Al4V being the fabrication material, the FEA results show that the CPM can obtain the large workspace of ± 3 mm $\times \pm 3$ mm $\times \pm 6.5$ mm $\times \pm 6° \times \pm 6° \times \pm 7.5°$.

113

6.2 Improvement of Dynamic Property by Employing Cellular Structure

Due to the conflict between the stiffness and dynamic properties, the first resonance frequency is targeted at 100 Hz to maintain the flexibility of the CPM. As the CPM will later be fabricated by EBM method, the advantages of 3D printing technology are exploited to enhance its dynamic response. In particular, the end effector of the CPM will be printed in cellular structure to reduce its mass and improve the dynamic property of the entire CPM. Figure 6.3 shows the general model of an element in cellular structure that will be used to design the end effector.
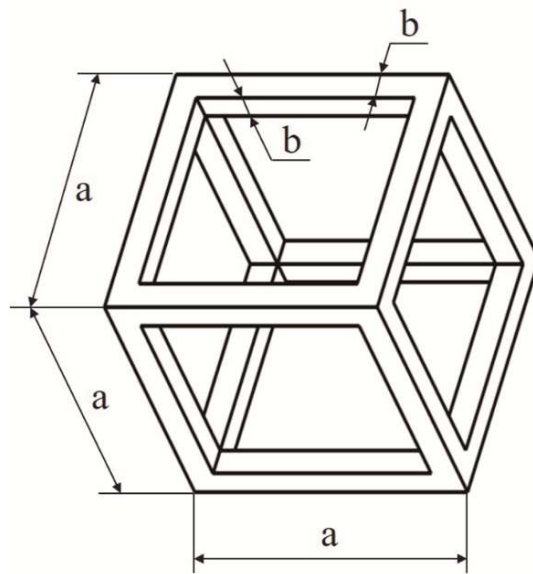
Figure 6.3: General model of the cellular structure.

The cellular element is modeled by a hollow cube which is created by a frame structure with the length and cross-sectional area of each beam being a and b^2 respectively. Note that each beam has a square cross section. The relationship between a and b is given as

$$b = \Delta a, \quad \text{where } 0 < \Delta \le 0.5 \tag{6.6}$$

The volume of the cellular element shown in Figure 6.3, $V_{cellular}$, is expressed as

$$
\begin{aligned}
V_{cellular} &= a^3 - (a - 2b)^3 - 6b(a - 2b)^2 \\
&= a^3 \left(12\Delta^2 - 16\Delta^3 \right)
\end{aligned}
\tag{6.7}
$$

The volume ratio, V_R, represents the ratio between the volumes of cellular structure ($V_{cellular}$) and solid structure (V_{solid}) is

$$
V_R = \frac{V_{cellular}}{V_{solid}} = \frac{a^3 \left(12\Delta^2 - 16\Delta^3 \right)}{a^3} = 12\Delta^2 - 16\Delta^3
\tag{6.8}
$$

Figure 6.4 illustrates the relationship between V_R and Δ. It is observed that the volume of cellular structure is equal to zero when $\Delta = 0$ and equal to solid structure when $\Delta = 0.5$. Although CPM can achieve faster dynamic response with the smaller mass/volume of the end effector, V_R cannot be too small because the beams in cellular structure becomes very thin and that reduces the stiffness of the end effector. With a weak structure, the end effector becomes flexible and can be deformed under external loads. Here, V_R is selected as 0.2 (corresponding to $\Delta = 0.144$) to maintain the high stiffness of the end effector while its mass is reduced up to 80%. The CPM is reanalyzed with the cellular end-effector and the updated frequency vector, $F_{cellular}^{6\text{-DOF}}$, is expressed in Eq. (6.9). Comparing to Eq. (6.5), it is seen that the first resonance frequency has increased 33%, the total difference between neighboring modes has also improved as well.
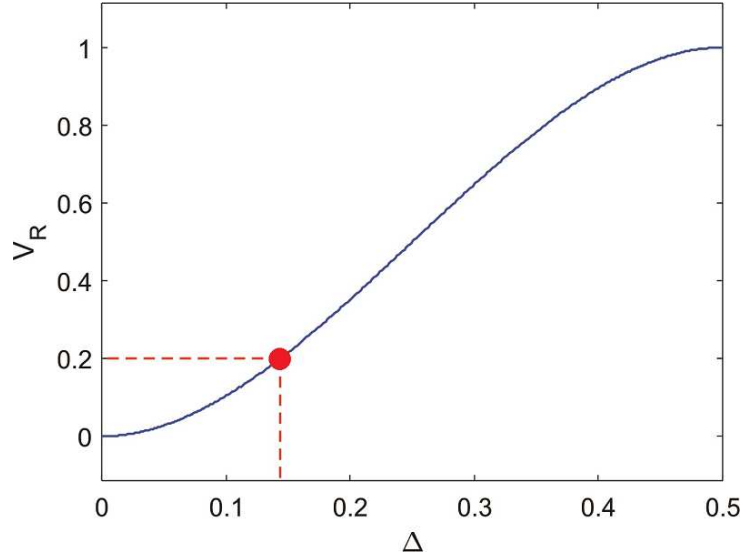
Figure 6.4: Ratio between volumes of cellular structure and solid structure.

$$F_{\text{cellular}}^{\text{6-DOF}} = \begin{bmatrix} \Delta_Z & \Delta_X & \Delta_Y & R_Z & R_X & R_Y \\ 133 & 185 & 185 & 186 & 403 & 403 \end{bmatrix} \quad (6.9)$$

Note that the stiffness property of the CPM is unchanged since the structure of the C-T beams is remained.

6.3 Experimental Investigation and Results

6.3.1 3D-printed prototype

A physical prototype of the synthesized CPM built by EBM technology anh Ti6Al4V material following the process presented in Appendix B is shown in Figure 6.5. It is observed that the end effector is constructed by cellular structure illustrated in Figure 6.3 and it can be well fabricated by EBM method. Here, the Z axis of the prototype is selected as the building direction. Referring to Chapter 4, the actual thickness of 3D-printed C-T beams is different from the designed value so that a coefficient factor is necessary to define the effective thickness, which determines the actual stiffness characteristics. By applying the findings presented in Appendix C , the coefficient factor is found to be 1.29 for the building direction

116

of the proposed prototype, which is along the width of flexures. It suggests that the effective thickness of the C-T beams is 29% higher than the original design. This factor is used to compensate the thickness of thin features in the prototype. The results of the stiffness and dynamic properties after considering the effective thickness are represented by $\overline{C}^{\text{6-DOF}}$ and $\overline{F}^{\text{6-DOF}}$ respectively.
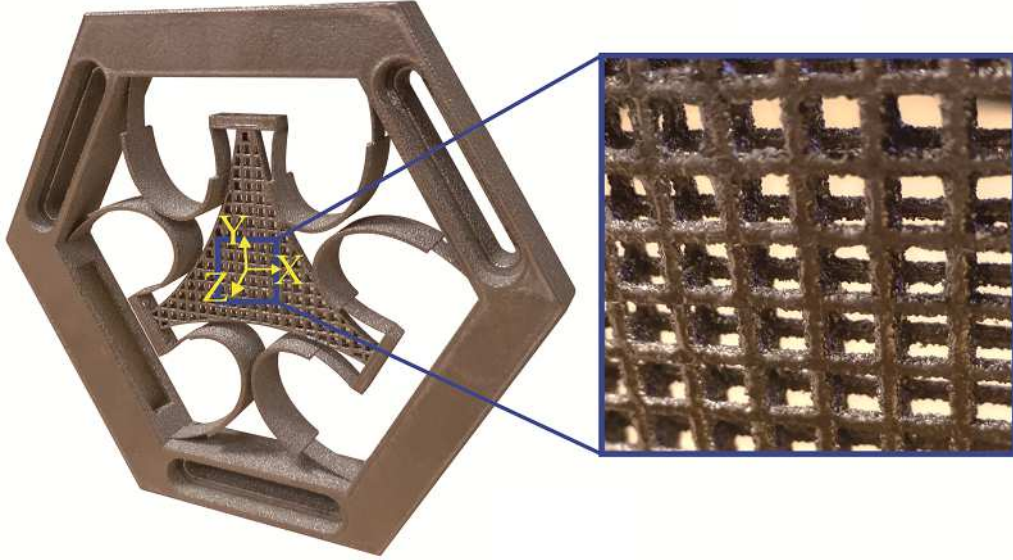
Figure 6.5: 3D-printed prototype built by EBM method with Ti6Al4V material.

$$\overline{C}^{\text{6-DOF}} = \begin{bmatrix} 2.77e-5 & & & & & \\ 0 & 2.77e-5 & & & SYM & \\ 0 & 0 & 5.92e-5 & & & \\ 0 & 0 & 0 & 3.09e-2 & & \\ 0 & 0 & 0 & 0 & 3.09e-2 & \\ 0 & 0 & 0 & 0 & 0 & 2.75e-2 \end{bmatrix} \tag{6.10}$$

$$\overline{F}^{\text{6-DOF}} = \begin{bmatrix} \Delta_Z & \Delta_X & \Delta_Y & R_Z & R_X & R_Y \\ 169 & 218 & 218 & 219 & 398 & 398 \end{bmatrix} \tag{6.11}$$

Note that $\overline{C}^{\text{6-DOF}}$ and $\overline{F}^{\text{6-DOF}}$ will be used to represent the stiffness and dynamic properties of the 3D-printed CPM in the remaining of this Chapter. After the thickness compensation, the workspace of ±3 mm × ±3 mm × ±6.5 mm × ±6° × ±6° × ± 7.5° of the CPM is still remained.

6.3.2 Evaluation of compliance

a) Translational compliance along the X and Y axes

The experimental setup to evaluate the compliance along the X axis is shown in Figure 6.6a. Two micrometers located at two opposite sides of the CPM are used to apply a pure force along the X axis to the end effector. A 6-axes force/torque (F/T) sensor (ATI Mini40) is attached on one micrometer to measure the actuating force. Both micrometers are adjusted with the same displacement to ensure the end effector only displaces along the X axis. At a specific displacement, the reading from the F/T sensor indicates a haft of the total force applied to the CPM. A similar setup is adopted to measure the compliance along the Y axis. The experimental compliance along the X and Y axes are shown in Figure 6.7a and Figure 6.7b respectively.
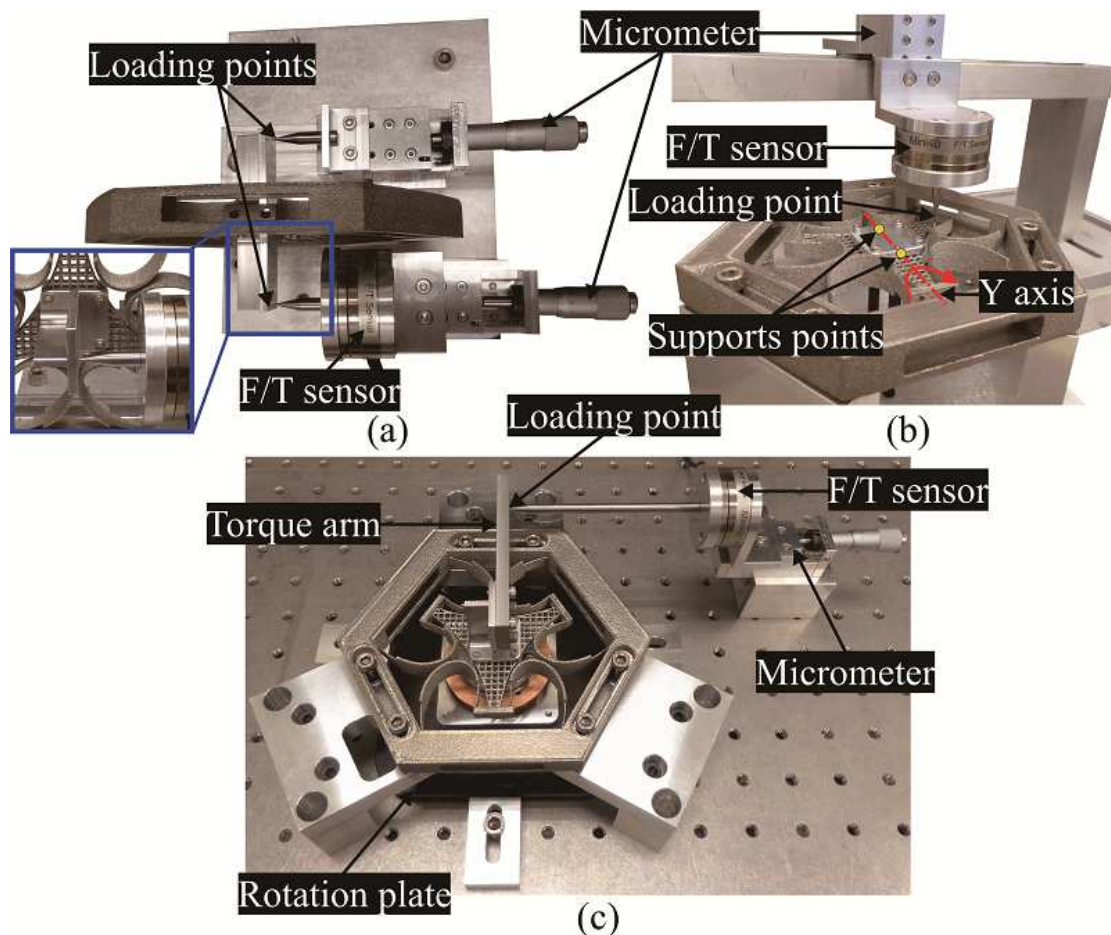
Figure 6.6: Experimental setups for measuring the compliance (a) along the X axis, (b) about the Y axis and (c) about the Z axis.

b) *Rotational compliance about the X and Y axes*

Figure 6.6b shows the experimental setup to measure the compliance about the Y axis of the CPM. Two contact points are installed at the bottom surface of the end effector, the input force along the Z direction from the micrometer is measured by the F/T sensor. The force is applied at a specific distance from the rotation axis, the bending moment and the rotation angle can be calculated based on this distance and the corresponding input force. The similar setup is adopted to evaluate the compliance about the X axis. The experimental compliance about the X and Y axes are shown in Figure 6.7d and Figure 6.7e respectively.
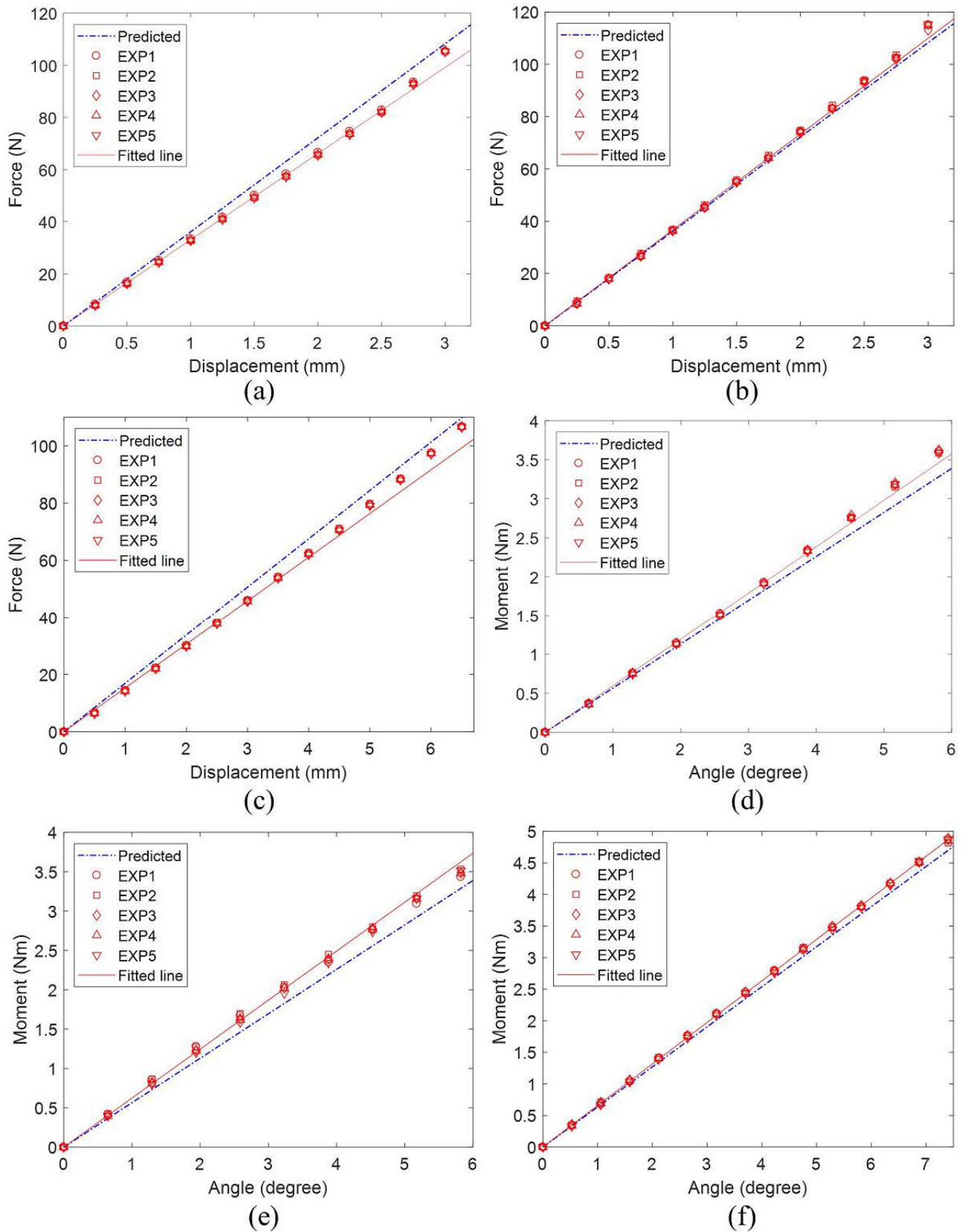
Figure 6.7: Experimental results of the 3D-printed CPM (a), (b), (c) translational compliance along the *X*, *Y* and *Z* axes respectively and (d), (e), (f) rotational compliance about the *X*, *Y* and *Z* axes respectively.

c) Translational compliance along the Z axis

From Figure 6.6b, to measure the compliance along the Z axis, the support points are removed, and the loading point is shifted to the center of the end effector. The obtained result is shown in Figure 6.7c.

d) Rotational compliance about the Z axis

The experimental setup for evaluating the compliance about the Z axis is shown in Figure 6.6c. A micrometer is used to apply a perpendicular force to a torque arm mounted to the end effector. A rotational plate is attached below the end effector to support its motion so that only the rotation about the Z axis is allowed. Based on the force measured by the F/T sensor and the distance between the loading point and the rotation axis, the torque and rotation angle can be determined. The experimental result of the compliance about the Z axis is shown in Figure 6.7f.

e) Summary of results

From Figure 6.7, it is seen that the CPM is able to perform good repeatability and the desired workspace of ± 3 mm $\times$ ± 3 mm $\times$ ± 6.5 mm $\times$ $\pm 6°$ $\times$ $\pm 6°$ $\times$ $\pm 7.5°$ is experimentally achieved. The experimental results together with the predicted values in Eq. (6.10) and their deviations are summarized in Table 6.1.

The data in Table 6.1 demonstrates that the experimental stiffness characteristics of the 3D-printed CPM well agree with the predicted values with the highest deviation of 10.47%. Based on the obtained results, it can be concluded that the proposed coefficient factor is applicable to correct the thickness of compliant mechanisms fabricated by EBM with the building direction being along the width of flexures. In addition, the synthesized CPM is able to perform large work range, predictable stiffness property and repeatable motions.

Table 6.1: Deviations between the experimental compliance compared against the predicted values.

Compliance	Predicted	Experiment	Deviation
along the X axis (m/N)	2.77e-5	3.02e-5	9.03%
along the Y axis (m/N)	2.77e-5	2.73e-5	1.44%
along the Z axis (m/N)	5.92e-5	6.54e-5	10.47%
about the X axis (rad/Nm)	3.09e-2	2.93e-2	5.18%
about the Y axis (rad/Nm)	3.09e-2	2.80e-2	9.39%
about the Z axis (rad/Nm)	2.75e-2	2.65e-2	3.64%

6.3.3 Evaluation of decoupled-motion capability

As decoupled-motion capability is one of the most important characteristics of the synthesized 6-DOF CPM, it will be experimentally demonstrated. Because the stiffness/compliance matrix of the CPM is symmetrical, there are five non-diagonal components need to be measured as shown in Eq. (5.5). Assuming the five non-diagonal components in the stiffness matrix of the CPM exist, the total work done in the ith direction is written as

$$W_i = \sum_{j=1}^{6} \frac{1}{2} \frac{P_j^2}{K_{ij}} \tag{6.12}$$

Here, all external loads that generate parasitic motions will be experimentally measured. Based on Eq. (5.5), when applying a force along the X axis, two parasitic motions are generated, i.e., the rotations about the X and Y axes. The bending moments about the X and Y axes are measured by the F/T sensor using the same setup as shown in Figure 6.6a. The experiment is conducted five times and the plot shows the ratios between the energies of parasitic motions and the total energy along the X axis is illustrated in Figure 6.8a. By using

similar experimental setups as presented previously, the energy ratios along the Y and Z axes are shown in Figure 6.8b and Figure 6.8c respectively.
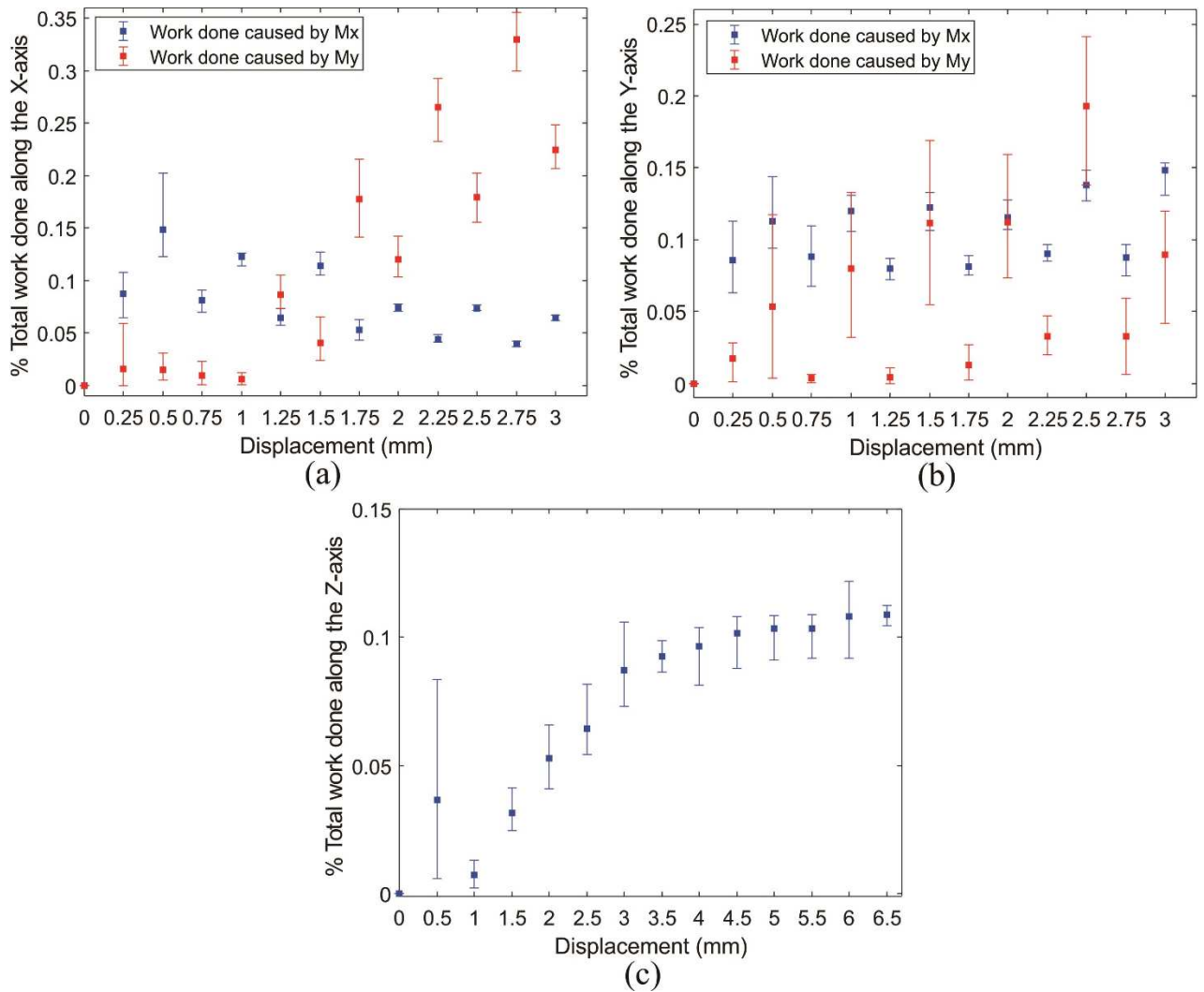
Figure 6.8: Ratios between energies of parasitic motions and energy of desired motion (a) along the X axis, (b) along the Y axis and (c) along the Z axis.

From Figure 6.8, it is seen that the highest energy of parasitic motions only contributes about 0.35%, 0.2% and 0.1% over the total energies along the X, Y and Z axes respectively. The parasitic motions are caused by the non-ideal experimental setups, i.e., the directions of input forces are not ideally parallel to the desired actuating directions. The results suggest that almost all the input energy is used to create the desired motion. The experimental results demonstrate that the synthesized CPM is able to produce decoupled motions.

6.3.4 Evaluation of dynamic behavior

An impact hammer (PCB PIEZOTRONICS 086C3) is used to apply the excitation, a single-axis accelerometer (PCB PIEZOTRONICS 353B15) is used to measure the acceleration, the readings from the hammer and accelerometer are acquired by a signal acquisition device (DATA TRANSLATION DT9837) and then analyzed by the Dewe-FRF 6.6 software.

From Figure 6.9, it is seen that some supporting parts are mounted on the end effector to attach the accelerometer and transmit the input excitations to the CPM. The total mass of the end effector has significantly increased due to the additional masses of supporting parts. Taking into consideration of the additional masses, the compensated frequency vector, $\bar{F}'^{\text{6-DOF}}$, is expressed as

$$\bar{F}'^{\text{6-DOF}} = \begin{bmatrix} \Delta_Z & \Delta_X & \Delta_Y & R_Z & R_X & R_Y \\ 143 & 191 & 191 & 207 & 361 & 361 \end{bmatrix} \tag{6.13}$$

a) *Dynamic response along the Z axis*

Firstly, the evaluation of the first vibration mode along the *Z* axis is carried out. The accelerometer is attached below the end effector to measure the acceleration along the *Z* axis, an excitation in the same direction is applied by the impact hammer as shown in Figure 6.9a. The obtained result is plotted in Figure 6.10a. It is seen that the experimental resonance frequency along the *Z* axis is 138 Hz, which has a small deviation of 3.5% compared to the predicted value of 143 Hz.
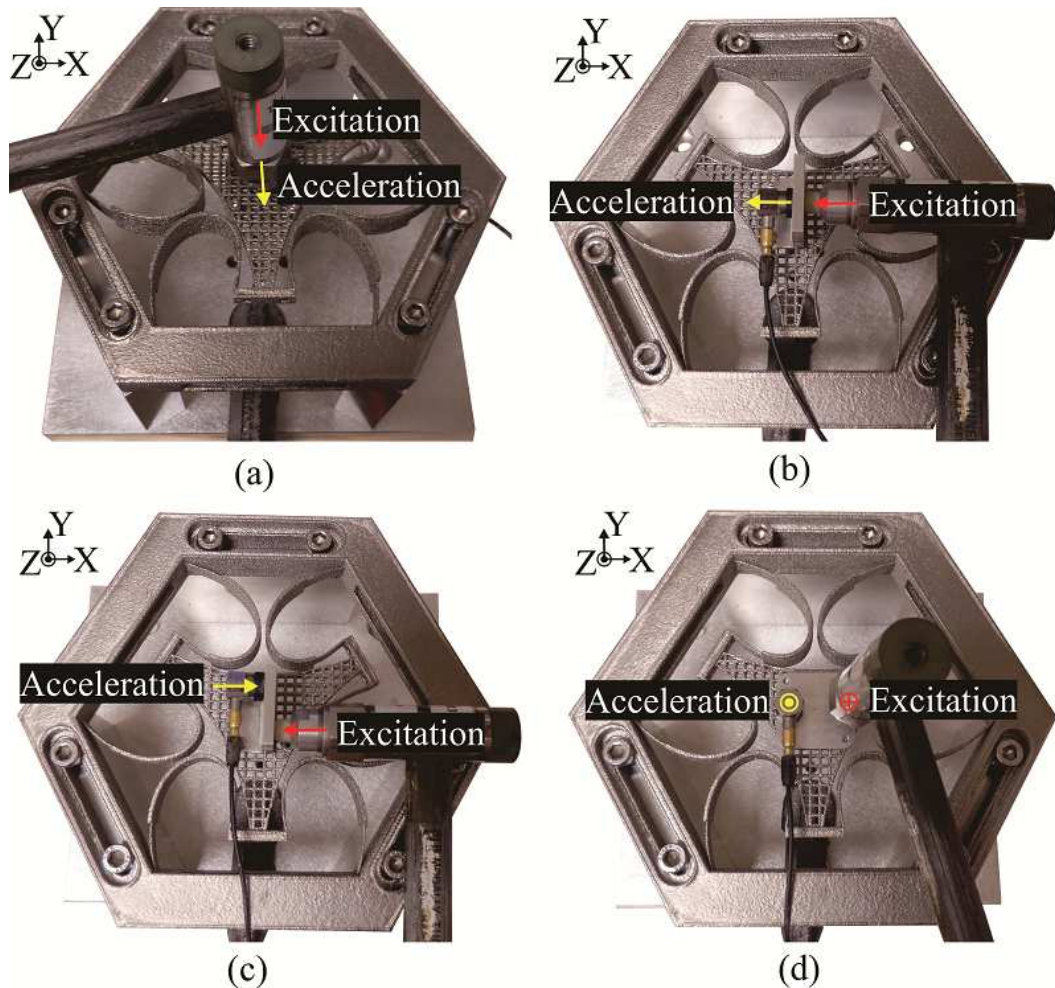
Figure 6.9: Experimental setup to measure the dynamic response (a) along the Z axis, (b) along the X axis, (c) about the Z axis and (d) about the Y axis.

b) *Dynamic responses along the X and Y axes*

Next, the dynamic responses along the X and Y axes are evaluated. Figure 6.9b shows the experimental setup to measure the dynamic response along the X axis. A L-shape supporting part is mounted on the top surface of the end effector. The accelerometer is attached to one side and the excitation is applied at the other side of the supporting part. Note that the directions of the acceleration and excitation are parallel to the X axis. Because the input force is measured at a specific distance along the Z axis from the end effector, a bending moment about the Y axis is also generated and the accelerometer is able to detect the acceleration about the Y axis as well. Hence, the dynamic responses along the X axis and about the Y axis can be measured

simultaneously through this experiment as shown in Figure 6.10b. It is observed that two vibration modes are clearly shown in the plot; the first peak represents the resonance frequency along the X axis while the second peak represents the resonance frequency about the Y axis. The measured dynamic response along the X axis is 175 Hz, which is close to the predicted value of 191 Hz with the deviation of 8.38%. A similar setup is adopted to measure the dynamic responses along the Y axis and the result is plotted in Figure 6.10c.

From Figure 6.10b and Figure 6.10c, it is seen that the dynamic responses of 330 Hz and 334 Hz about the X and Y axes respectively are lower than the predicted value of 361 Hz. The experimental results can be improved by using a better setup as described below.

c) *Dynamic responses about the X and Y axes*

The setup to measure the dynamic response about the Y axis of the CPM is shown in Figure 6.9d. A flat part used to attach the accelerometer is mounted on the end effector. The excitation is applied at a specific distance from the Y axis while the acceleration is measured at the opposite side. Since the directions of the excitation and acceleration are parallel to the Z axis, the first vibration mode along the Z axis can also be detected. The result is shown in Figure 6.10f. It is seen that the first mode nearly coincides with the previous measurement and the sixth mode about the Y axis is 353 Hz which well matches the prediction of 361 Hz with a small deviation of 2.22%. A similar setup is adopted to measure the dynamic response about the X axis and the results is plotted in Figure 6.10e.
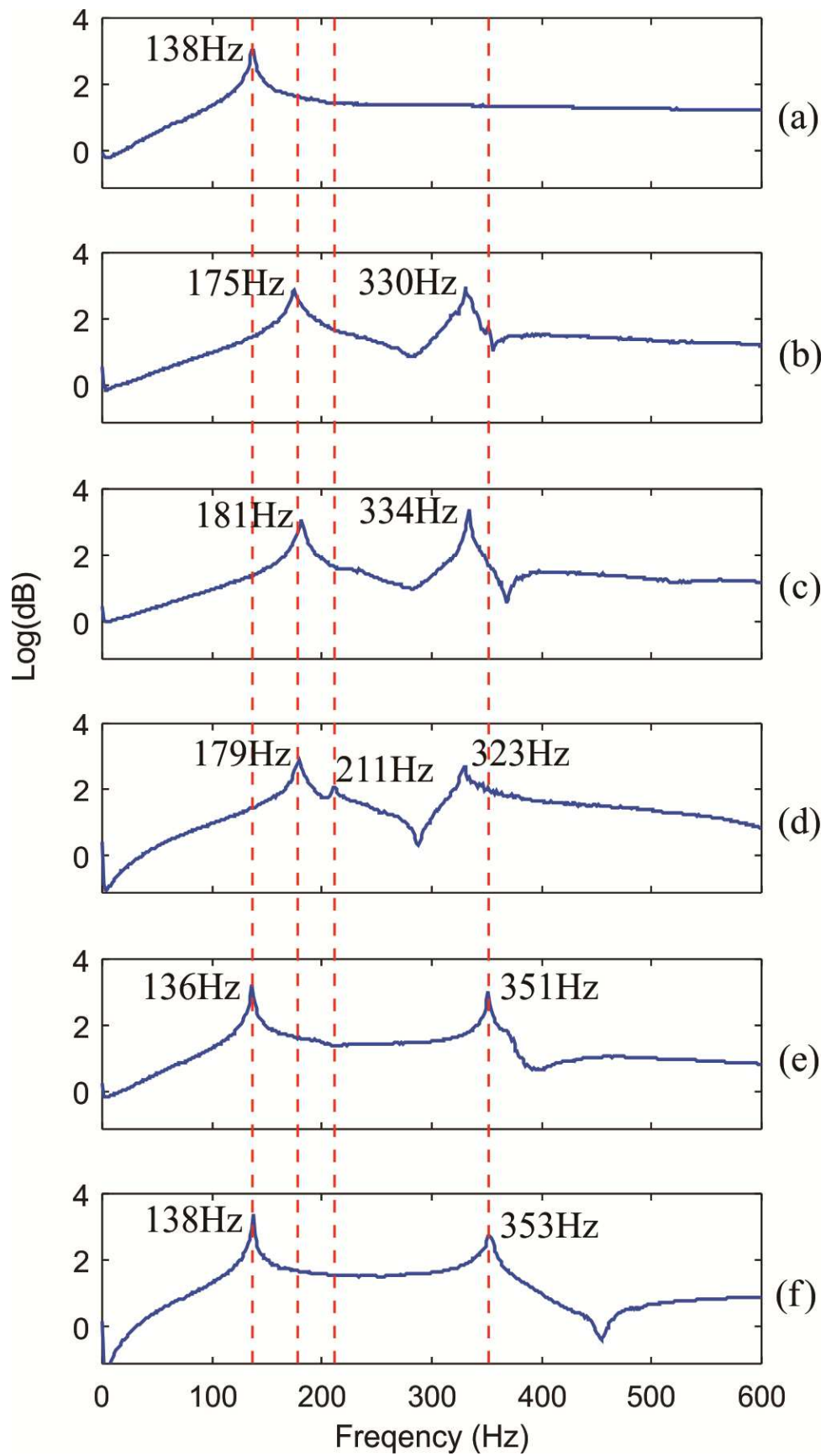
Figure 6.10: Experimental dynamic response of the CPM (a), (b), (c) along the *Z*, *X* and *Y* axes respectively, (d), (e), (f) about the *Z*, *X* and *Y* axes respectively.

d) *Dynamic response about the Z axis*

Lastly, the fourth vibration mode about the Z axis of the CPM is evaluated by the setup shown in Figure 6.9c. It is similar to the setup for measuring the response along the X axis, but the accelerometer and impact position are shifted to two opposite sides of the support part. With this setup, three dynamic responses, i.e., along the X axis, about the Z and Y axes, can be simultaneously measured and the obtained results are plotted in Figure 6.10d.

e) *Summary of results*

The experimental dynamic responses together with the deviations compared to the predicted values in Eq. (6.13) are summarized in Table 6.2. The highest deviation of the experimental results is found to be less than 9%; this demonstrates the predictable dynamic property of the synthesized CPM with a cellular end-effector.

Table 6.2: Deviations between the experimental dynamic responses compared against the predicted values.

Mode	Resonance frequency	Predicted	Experiment	Deviation
1	Translation along the Z axis	143 Hz	138 Hz	3.50%
2	Translation along the X axis	191 Hz	175 Hz	8.38%
3	Translation along the Y axis	191 Hz	181 Hz	5.24%
4	Rotation about the Z axis	207 Hz	211 Hz	1.93%
5	Rotation about the X axis	361 Hz	351 Hz	2.77%
6	Rotation about the Y axis	361 Hz	353 Hz	2.22%

6.4 Summary

This Chapter presents a novel design of 6-DOF CPM synthesized by the beam-based method and the design criteria for achieving decoupled motions. The advantage of 3D printing technology, i.e., the ability to fabricate cellular structures, is exploited to improve the dynamic property of the CPM by reducing the mass of the end effector. As a result, the first resonance frequency of the CPM can reach 133 Hz, which is 33% higher than the design using the solid end effector. In addition, the synthesized CPM is able to produce large workspace of more than 6 mm for the translations and 12° for the rotations.

Some experiments are carried out to evaluate the actual performance of the EBM-printed prototype. As the effective thickness of the C-T beams are accurately estimated by the coefficient factor, the 3D-printed prototype of the CPM can provide predictable behaviors. The experimental results show that the mechanical characteristics of the prototype well agree with the predicted data with the highest deviations of 10.47% and 8.38% for the stiffness and dynamic properties respectively. Moreover, the CPM is able to achieve full workspace and the measured six vibration modes well match the prediction. The decoupled motions of the CPM are also experimentally demonstrated, the obtained results suggest that the energies caused by parasitic motions only contribute less than 0.5% over the total input energies generating the desired motions.

CHAPTER 7
CONCLUSION AND FUTURE WORKS

This Chapter concludes the results obtained from this work. In addition, the main contributions are summarized, and some future works are also outlined.

7.1 Conclusion

a) *Beam-based structural optimization method*

In this research, a novel design methodology, termed as beam-based structural optimization method, has been developed for synthesizing multi-DOF CPMs with optimized stiffness and dynamic properties for precise positioning systems. The desired motions of CPMs can be achieved by optimizing the geometry of two reflecting C-T beams within each compliant limb. Moreover, an analytical approach that normalizes different units of components within the stiffness matrix has been proposed to derive an objective function with well-defined unit for the optimization process.

b) *Synthesis of a 3-DOF spatial-motion ($\theta_X - \theta_Y - Z$) CPM*

A novel 3-DOF spatial-motion ($\theta_X - \theta_Y - Z$) CPM has been synthesized using the beam-based method. The analytical results show that the CPM is able to produce good stiffness property through the high stiffness ratios of more than 4000 and 200 for translational and rotational motions respectively, large workspace of $\pm 4° \times \pm 4° \times \pm 2.75$ mm and fast dynamic response with the first resonance frequency of 100 Hz. Experiments are conducted to evaluate the performance of the synthesized CPM. The effectiveness of the proposed beam-based method has been demonstrated since the experimental results well agree with the prediction.

c) Investigation on mechanical properties of 3D-printed CPM

EBM technology has been used to monolithically fabricate a prototype of the synthesized 3-DOF ($\theta_X - \theta_Y - Z$) CPM with Ti6Al4V material. A coefficient factor of 1.27 has been proposed to compensate the difference between the designed thickness and effective thickness of EBM-printed flexures caused by the surface roughness. With the application of effective thickness for the C-T beams, the 3D-printed CPM has performed predictable stiffness and dynamic properties through the small deviations between analysis and measured data. Furthermore, a 3-DOF manipulator built by the 3D-printed CPM has been developed and experimentally evaluated. The measurements show that the 3D-printed manipulator can achieve a full workspace of $\pm 3° \times \pm 3° \times \pm 2$ mm, high resolution and good positioning accuracy of 0.14" $\times$ 0.12" $\times$ 20 nm and ± 0.058" $\times \pm 0.065$" $\times \pm 10.8$ nm respectively. These results demonstrate that EBM technology can be used to fabricate CPMs for high-precision systems.

d) Design criteria for CPMs with fully-decoupled motions

As CPMs are preferred in positioning applications, design criteria for synthesizing CPMs with fully-decoupled motions have been analytically derived. The findings provide some conditions for position and orientation of each flexible element/compliant joint in each limb. The derived criteria are applied to synthesize an improved 3-DOF ($\theta_X - \theta_Y - Z$) CPM. The motion property of the new CPM has been verified experimentally and compared to the previous design to demonstrate the correctness of the proposed criteria. Most importantly, those criteria are applicable to any design method and can be applied to determine the motion property of any CPM.

e) Synthesis of a 6-DOF CPM

A novel 6-DOF CPM has been synthesized using the proposed beam-based method and design criteria. The advantage of 3D printing technology in fabricating cellular/lattice

structures is also exploited to enhance the dynamic behavior for the CPM. By using the end effector fabricated by cellular structure, dynamic response of the 3D-printed CPM can be improved up to 33%. Beside the predictable stiffness and dynamic characteristics, the experimental investigations also show that the CPM can produce large workspace of more than 6 mm and 12° for the translations and rotations respectively. Additionally, the decoupled-motion capability of the CPM has been evaluated. The measured results suggest that the parasitic displacements are nearly zero since more than 99.5% of input energy is used to create the desired motion for the CPM.

7.2 Contributions

The main contributions of this research are summarized as follows:

- A novel beam-based structural optimization method is developed. The method is able to synthesize multi-DOF CPMs for positioning applications with optimized stiffness property and targeted dynamic behavior. Using the method, novel 3-DOF ($\theta_X - \theta_Y - Z$) and 6-DOF CPMs are synthesized with optimized mechanical characteristics and large workspace.

- A new objective function for the stiffness optimization of CPMs is derived to address limitation of existing functions in governing the different units of components within the stiffness matrix. The proposed objective function with well-defined unit can be used to optimize any CPM with single- or multi-DOF.

- Several criteria for synthesizing CPMs with fully-decoupled motions are analytically derived. The criteria can be applied to synthesize or analyze the motion property of any CPM regardless of its DOF. The derived criteria are verified by the syntheses of decoupled-motion 3-DOF ($\theta_X - \theta_Y - Z$) and 6-DOF CPMs.

- Some insights into the mechanical properties of 3D-printed CPMs using EBM method are investigated. In particular, a coefficient factor is proposed to determine the effective thickness of EBM-printed flexures, enabling the mechanical properties of 3D-printed CPMs to be predictable.

7.3 Future Works

Several aspects of the current research need to be further investigated and the suggested research directions are as follows:

- Although the beam-based method can accurately predict six primary vibration modes of CPMs, only the first resonance mode is successfully optimized to the targeted frequency. In order to develop compliant devices for advanced positioning applications, all six vibration modes of CPMs need to be optimized during the synthesis process. Additionally, the truly global-optimal result can be obtained only when the stiffness and dynamic optimization processes are done together. Thus, it is necessary to develop a new objective function that can govern the stiffness property and six vibration modes of the CPMs.

- The proposed beam-based method is able to synthesize CPMs for positioning applications, but the actuation has not been taken into account. To actuate a CPM synthesized by beam-based method, actuators and compliant supports need to be selected and allocated into the CPM. As a result, behaviors of the entire system would be different from the original prediction which only considers the CPM. Hence, the implementation of actuation in the synthesis process is essential.

- In this research, several criteria for synthesizing decoupled-motion CPMs have been derived and verified by the designs of a 3-DOF ($\theta_X - \theta_Y - Z$) CPM and a 6-DOF CPM with fully-decoupled motions. The proposed criteria are achieved by solving some

special cases of governing equations. There are still many possible cases to be investigated and more general design criteria can be obtained.

- This research suggests that EBM technology is applicable to fabricate compliant devices for motion systems. It is seen that by defining the effective thickness of flexures based on the proposed coefficient factor, the mechanical properties of EBM-printed CPM can be predicted. However, some preliminary investigations (see Appendix C) show that the coefficient factor varies with the building directions as well as the designed thickness of flexures. Further research needs to be conducted to determine a general model and formulation that can accurately represent the effective thickness with regard to building direction, geometry and designed thickness of flexures as well as printing parameters.

List of Author's Publications

- ## *Journal Publications*

1. **M. T. Pham**, T. J. Teo, S. H. Yeo, P. Wang, and M. L. S. Nai, "A 3D-printed Ti-6Al-4V 3-DOF compliant parallel mechanism for high precision manipulation," *IEEE/ASME Transactions on Mechatronics*, vol. 22, pp. 2359-2368, 2017.

2. **M. T. Pham**, T. J. Teo, S. H. Yeo, "Synthesis of multiple degrees-of-freedom spatial-motion compliant parallel mechanisms with desired stiffness and dynamics characteristics," *Precision Engineering*, vol. 47, pp. 131-139, 2017.

3. **M. T. Pham**, T. J. Teo, S. H. Yeo, P. Wang, and M. L. S. Nai, "A novel 3-DOF fully decoupled-motion compliant parallel mechanism with optimized stiffness and dynamic characteristics," *Journal of Mechanical Design* (preparing for submission).

4. **M. T. Pham**, S. H. Yeo, T. J. Teo, "Three-legged compliant parallel mechanisms: fundamental design criteria to achieve fully-decoupled motion characteristics and a state-of-the-art review," *Precision Engineering* (preparing for submission).

- ## *Conference Publications*

1. **M. T. Pham**, T. J. Teo, S. H. Yeo, P. Wang, and M. L. S. Nai, "Synthesis and evaluation of a high precision 3D-printed Ti6Al4V compliant parallel manipulator," *in IOP Conference Series: Material Science and Engineering*, (Ho Chi Minh City, Vietnam), vol. 280, p. 012040, November 2017.

2. **M. T. Pham**, T. J. Teo, and S. H. Yeo, "Investigation of the mechanical properties of 3D printed compliant mechanisms," *in 2nd International Conference on Progress in Additive Manufacturing*, (Singapore), pp. 109-115, May 2016.

References

[1] L. L. Howell, S. P. Magleby, and B. M. Olsen, *Handbook of compliant mechanisms*: John Wiley & Sons, 2013.

[2] A. Yamaguchi, K. Takemura, S. Yokota, and K. Edamura, "A robot hand using electro-conjugate fluid: Grasping experiment with balloon actuators inducing a palm motion of robot hand," *Sensors and Actuators A: Physical,* vol. 174, pp. 181-188, 2012.

[3] A. G. Zisimatos, M. V. Liarokapis, C. I. Mavrogiannis, and K. J. Kyriakopoulos, "Open-source, affordable, modular, light-weight, underactuated robot hands," in *IEEE/RSJ International Conference on Intelligent Robots and Systems (IROS)*, 2014, pp. 3207 - 3212.

[4] P. Qi, C. Qiu, H. Liu, J. S. Dai, L. D. Seneviratne, and K. Althoefer, "A Novel Continuum Manipulator Design Using Serially Connected Double-Layer Planar Springs," *IEEE/ASME Transactions on Mechatronics,* vol. 21, pp. 1281-1292, 2016.

[5] M. Grossard, C. Rotinat-Libersa, N. Chaillet, and M. Boukallel, "Mechanical and Control-Oriented Design of a Monolithic Piezoelectric Microgripper Using a New Topological Optimization Method," *IEEE/ASME Transactions on Mechatronics,* vol. 14, pp. 32-45, 2009.

[6] D. H. Wang, Q. Yang, and H. M. Dong, "A Monolithic Compliant Piezoelectric-Driven Microgripper: Design, Modeling, and Testing," *IEEE/ASME Transactions on Mechatronics,* vol. 18, pp. 138-147, 2013.

[7] F. Wang, C. Liang, Y. Tian, X. Zhao, and D. Zhang, "Design of a Piezoelectric-Actuated Microgripper With a Three-Stage Flexure-Based Amplification," *IEEE/ASME Transactions on Mechatronics,* vol. 20, pp. 2205-2213, 2015.

[8] M. G. Song, H. W. Baek, N. C. Park, K. S. Park, T. Yoon, Y. P. Park*, et al.*, "Development of Small Sized Actuator With Compliant Mechanism for Optical Image Stabilization," *IEEE Transactions on Magnetics,* vol. 46, pp. 2369-2372, 2010.

[9] T. J. Teo, V. P. Bui, G. Yang, and I. M. Chen, "Millimeters-Stroke Nanopositioning Actuator With High Positioning and Thermal Stability," *IEEE/ASME Transactions on Mechatronics,* vol. 20, pp. 2813-2823, 2015.

[10] T. J. Teo, G. Yang, and I. M. Chen, "A flexure-based electromagnetic nanopositioning actuator with predictable and re-configurable open-loop positioning resolution," *Precision Engineering,* vol. 40, pp. 249-260, 2015.

[11] T. J. Teo, I. M. Chen, G. Yang, and W. Lin, "A Novel Actuator for High-Precision Alignment in a Nano-Imprint Multi-Layers-Interconnection Fabrication," in *IEEE International Conference on Robotics and Automation*, 2007, pp. 1419-1424.

[12] G. Hao and X. He, "Designing a monolithic tip-tilt-piston flexure manipulator," *Archives of Civil and Mechanical Engineering,* vol. 17, pp. 871-879, 2017.

[13] W. Dan and F. Rui, "Design and nonlinear analysis of a 6-DOF compliant parallel manipulator with spatial beam flexure hinges," *Precision Engineering,* vol. 45, pp. 365-373, 2016.

[14] N. F. Wang and K. Tai, "Design of 2-DOF Compliant Mechanisms to Form Grip-and-Move Manipulators for 2D Workspace," *Journal of Mechanical Design,* vol. 132, p. 031007, 2010.

[15] L. Yangmin and X. Qingsong, "Design and Analysis of a Totally Decoupled Flexure-Based XY Parallel Micromanipulator," *IEEE Transactions on Robotics,* vol. 25, pp. 645-657, 2009.

[16] C. Wenjie, L. Wei, and Y. Guilin, "A flexure-based 4-DOF coaxial alignment system: Design and application," in *2010 11th International Conference on Control Automation Robotics & Vision*, 2010, pp. 1755-1759.

[17] G. Yang, T. J. Teo, I. M. Chen, and W. Lin, "Analysis and design of a 3-DOF flexure-based zero-torsion parallel manipulator for nano-alignment applications," in *IEEE International Conference on Robotics and Automation (ICRA)*, 2011, pp. 2751-2756.

[18] J. Qu, W. Chen, J. Zhang, and W. Chen, "A large-range compliant micropositioning stage with remote-center-of-motion characteristic for parallel alignment," *Microsystem Technologies,* vol. 22, pp. 777-789, 2016.

[19] Q. Lu and Y. Zhang, "Design of Micro-positioning Stage with Large Stroke Based on Novel Compliant Parallel Mechanism," in *Mechanism and Machine Science: Proceedings of ASIAN MMS 2016 & CCMMS 2016*, ed: Springer Singapore, 2017, pp. 709-721.

[20] S. Wan and Q. Xu, "Design and analysis of a new compliant XY micropositioning stage based on Roberts mechanism," *Mechanism and Machine Theory,* vol. 95, pp. 125-139, 2016.

[21] C. Lee, C. K. Stepanick, S.-K. Lee, and J. A. Tarbutton, "Cross-coupling effect of large range XY nanopositioning stage fabricated by stereolithography process," *Precision Engineering,* vol. 46, pp. 81-87, 2016.

[22] K. Cai, Y. Tian, F. Wang, D. Zhang, and B. Shirinzadeh, "Development of a piezo-driven 3-DOF stage with T-shape flexible hinge mechanism," *Robotics and Computer-Integrated Manufacturing,* vol. 37, pp. 125-138, 2016.

[23] A. Alaa, H. Omer Faris, N. Marwan, and A. Mohamed Sultan Mohamed, "Design and fabrication of a novel XY θ z monolithic micro-positioning stage driven by NiTi shape-memory-alloy actuators," *Smart Materials and Structures,* vol. 25, p. 105004, 2016.

[24] Q. Xu, "Design of a Large-Range Compliant Rotary Micropositioning Stage With Angle and Torque Sensing," *IEEE Sensors Journal,* vol. 15, pp. 2419-2430, 2015.

[25] S. Xiao and Y. Li, "Optimal Design, Fabrication, and Control of an XY Micropositioning Stage Driven by Electromagnetic Actuators," *IEEE Transactions on Industrial Electronics,* vol. 60, pp. 4613-4626, 2013.

[26] Y. Qin, B. Shirinzadeh, Y. Tian, and D. Zhang, "Design issues in a decoupled XY stage: Static and dynamics modeling, hysteresis compensation, and tracking control," *Sensors and Actuators A: Physical,* vol. 194, pp. 95-105, 2013.

[27] Y. Li and Q. Xu, "Design and Robust Repetitive Control of a New Parallel-Kinematic XY Piezostage for Micro/Nanomanipulation," *IEEE/ASME Transactions on Mechatronics,* vol. 17, pp. 1120-1132, 2012.

[28]   Y. Li, J. Huang, and H. Tang, "A Compliant Parallel XY Micromotion Stage With Complete Kinematic Decoupling," *IEEE Transactions on Automation Science and Engineering,* vol. 9, pp. 538-553, 2012.

[29]   L.-J. Lai, G.-Y. Gu, and L.-M. Zhu, "Design and control of a decoupled two degree of freedom translational parallel micro-positioning stage," *Review of Scientific Instruments,* vol. 83, p. 045105, 2012.

[30]   D. Ahn, Y.-M. Choi, and J. Jeong, "Design of a four-degree-of-freedom nano positioner utilizing electromagnetic actuators and flexure mechanisms," *Review of Scientific Instruments,* vol. 86, p. 035101, 2015.

[31]   P. Liu, P. Yan, and Z. Zhang, "Design and analysis of an X–Y parallel nanopositioner supporting large-stroke servomechanism," *Proceedings of the Institution of Mechanical Engineers, Part C: Journal of Mechanical Engineering Science,* vol. 229, pp. 364-376, 2015.

[32]   M. Y. Chen, H. H. Huang, and S. K. Hung, "A New Design of a Submicropositioner Utilizing Electromagnetic Actuators and Flexure Mechanism," *IEEE Transactions on Industrial Electronics,* vol. 57, pp. 96-106, 2010.

[33]   T. J. Teo, G. Yang, and I. M. Chen, "Compliant Manipulators," in *Handbook of Manufacturing Engineering and Technology*, ed: Springer London, 2014, pp. 2229-2300.

[34]   T. Hui, L. Yangmin, and X. Xiao, "Development and assessment of a novel hydraulic displacement amplifier for piezo-actuated large stroke precision positioning," in *IEEE International Conference on Robotics and Automation (ICRA)*, 2013, pp. 1409-1414.

[35]   H.-W. Ma, S.-M. Yao, L.-Q. Wang, and Z. Zhong, "Analysis of the displacement amplification ratio of bridge-type flexure hinge," *Sensors and Actuators A: Physical,* vol. 132, pp. 730-736, 2006.

[36]   X. Li, Y. Tian, Y. Qin, F. Wang, W. Gao, D. Zhang*, et al.*, "Design, Identification and Control of a 2-Degree of Freedom Flexure-Based Mechanism for Micro/Nano Manipulation," *Nanoscience and Nanotechnology Letters,* vol. 5, pp. 960-967, 2013.

[37]   T. Hui and L. Yangmin, "Design, Analysis, and Test of a Novel 2-DOF Nanopositioning System Driven by Dual Mode," *IEEE Transactions on Robotics,* vol. 29, pp. 650-662, 2013.

[38]   G. Folkersma, S. Boer, D. Brouwer, and J. L. Herder, "A large-stroke planar 2-DOF flexure-based positioning stage for vacuum environments," in *IDECT ASME*, 2012, pp. 1-8.

[39]   Y. K. Yong, S. S. Aphale, and S. O. R. Moheimani, "Design, Identification, and Control of a Flexure-Based XY Stage for Fast Nanoscale Positioning," *IEEE Transactions on Nanotechnology,* vol. 8, pp. 46-54, 2009.

[40]   H. Wang and X. Zhang, "Input coupling analysis and optimal design of a 3-DOF compliant micro-positioning stage," *Mechanism and Machine Theory,* vol. 43, pp. 400-410, 2008.

[41]   H.-Y. Kim, D.-H. Ahn, and D.-G. Gweon, "Development of a novel 3-degrees of freedom flexure based positioning system," *Review of Scientific Instruments,* vol. 83, p. 055114, 2012.

[42] Y. K. Yong and T.-F. Lu, "Kinetostatic modeling of 3-RRR compliant micro-motion stages with flexure hinges," *Mechanism and Machine Theory,* vol. 44, pp. 1156-1175, 2009.

[43] Q. Yao, J. Dong, and P. M. Ferreira, "A novel parallel-kinematics mechanisms for integrated, multi-axis nanopositioning: Part 1. Kinematics and design for fabrication," *Precision Engineering,* vol. 32, pp. 7-19, 2008.

[44] T. Xueyan and I. M. Chen, "A Large-Displacement 3-DOF Flexure Parallel Mechanism with Decoupled Kinematics Structure," in *IEEE/RSJ International Conference on Intelligent Robots and Systems*, 2006, pp. 1668-1673.

[45] H.-H. Pham, H.-C. Yeh, and I.-M. Chen, "Micromanipulation system design based on selective actuation mechanisms," *The International Journal of Robotics Research,* vol. 25, pp. 171-186, 2006.

[46] T.-F. Lu, D. C. Handley, Y. K. Yong, and C. Eales, "A three-DOF compliant micromotion stage with flexure hinges," *Industrial Robot: An International Journal,* vol. 31, pp. 355-361, 2004.

[47] D. Zhang and Z. Gao, "Performance analysis and optimization of a five-degrees-of-freedom compliant hybrid parallel micromanipulator," *Robotics and Computer-Integrated Manufacturing,* vol. 34, pp. 20-29, 2015.

[48] Q. Liang, D. Zhang, Z. Chi, Q. Song, Y. Ge, and Y. Ge, "Six-DOF micro-manipulator based on compliant parallel mechanism with integrated force sensor," *Robotics and Computer-Integrated Manufacturing,* vol. 27, pp. 124-134, 2011.

[49] T. L. Wu, J. H. Chen, and S. H. Chang, "A six-DOF prismatic-spherical-spherical parallel compliant nanopositioner," *IEEE Transactions on Ultrasonics, Ferroelectrics, and Frequency Control,* vol. 55, pp. 2544-2551, 2008.

[50] J. B. Hopkins and R. M. Panas, "Design of flexure-based precision transmission mechanisms using screw theory," *Precision Engineering,* vol. 37, pp. 299-307, 2013.

[51] J. B. Hopkins, J. J. Vericella, and C. D. Harvey, "Modeling and generating parallel flexure elements," *Precision Engineering,* vol. 38, pp. 525-537, 2014.

[52] J. B. Hopkins and D. McCalib, "Synthesizing multi-axis flexure systems with decoupled actuators," *Precision Engineering,* vol. 46, pp. 206-220, 2016.

[53] G. Hao and J. Yu, "Design, modelling and analysis of a completely-decoupled XY compliant parallel manipulator," *Mechanism and Machine Theory,* vol. 102, pp. 179-195, 2016.

[54] H. Li and G. Hao, "Constraint-force-based approach of modelling compliant mechanisms: Principle and application," *Precision Engineering,* vol. 47, pp. 158-181, 2017.

[55] K.-J. Lu and S. Kota, "Topology and Dimensional Synthesis of Compliant Mechanisms Using Discrete Optimization," *Journal of Mechanical Design,* vol. 128, pp. 1080-1091, 2005.

[56] A. Krishnakumar and K. Suresh, "Hinge-Free Compliant Mechanism Design Via the Topological Level-Set," *Journal of Mechanical Design,* vol. 137, p. 031406, 2015.

[57] Y. Li, X. Huang, Y. M. Xie, and S. W. Zhou, "Evolutionary topology optimization of hinge-free compliant mechanisms," *International Journal of Mechanical Sciences,* vol. 86, pp. 69-75, 2014.

[58]   E. Lee and H. C. Gea, "A strain based topology optimization method for compliant mechanism design," *Structural and Multidisciplinary Optimization,* vol. 49, pp. 199-207, 2014.

[59]   X. Huang, Y. Li, S. W. Zhou, and Y. M. Xie, "Topology optimization of compliant mechanisms with desired structural stiffness," *Engineering Structures,* vol. 79, pp. 13-21, 2014.

[60]   B. Zhu, X. Zhang, and N. Wang, "Topology optimization of hinge-free compliant mechanisms with multiple outputs using level set method," *Structural and Multidisciplinary Optimization,* vol. 47, pp. 659-672, 2013.

[61]   B. Zhu and X. Zhang, "A new level set method for topology optimization of distributed compliant mechanisms," *International Journal for Numerical Methods in Engineering,* vol. 91, pp. 843-871, 2012.

[62]   N. T. Kaminakis and G. E. Stavroulakis, "Topology optimization for compliant mechanisms, using evolutionary-hybrid algorithms and application to the design of auxetic materials," *Composites Part B: Engineering,* vol. 43, pp. 2655-2668, 2012.

[63]   D. Ramrakhyani, M. Frecker, and G. Lesieutre, "Hinged beam elements for the topology design of compliant mechanisms using the ground structure approach," *Structural and Multidisciplinary Optimization,* vol. 37, pp. 557-567, 2009.

[64]   Z. Luo, L. Tong, M. Y. Wang, and S. Wang, "Shape and topology optimization of compliant mechanisms using a parameterization level set method," *Journal of Computational Physics,* vol. 227, pp. 680-705, 2007.

[65]   S. Chen and M. Y. Wang, "Designing distributed compliant mechanisms with characteristic stiffness," in *ASME International Design Engineering Technical Conferences and Computers and Information in Engineering Conference*, 2007, pp. 33-45.

[66]   R. Ansola, E. Veguería, J. Canales, and J. A. Tárrago, "A simple evolutionary topology optimization procedure for compliant mechanism design," *Finite Elements in Analysis and Design,* vol. 44, pp. 53-62, 2007.

[67]   M. Y. Wang, S. Chen, X. Wang, and Y. Mei, "Design of Multimaterial Compliant Mechanisms Using Level-Set Methods," *Journal of Mechanical Design,* vol. 127, pp. 941-956, 2005.

[68]   A. Saxena, "Topology design of large displacement compliant mechanisms with multiple materials and multiple output ports," *Structural and Multidisciplinary Optimization,* vol. 30, pp. 477-490, 2005.

[69]   S. Rahmatalla and C. C. Swan, "Sparse monolithic compliant mechanisms using continuum structural topology optimization," *International Journal for Numerical Methods in Engineering,* vol. 62, pp. 1579-1605, 2005.

[70]   Z. Luo, L. Chen, J. Yang, Y. Zhang, and K. Abdel-Malek, "Compliant mechanism design using multi-objective topology optimization scheme of continuum structures," *Structural and Multidisciplinary Optimization,* vol. 30, pp. 142-154, 2005.

[71]   K. Tai, G. Y. Cui, and T. Ray, "Design Synthesis of Path Generating Compliant Mechanisms by Evolutionary Optimization of Topology and Shape," *Journal of Mechanical Design,* vol. 124, pp. 492-500, 2002.

[72] K. Tai and T. H. Chee, "Design of Structures and Compliant Mechanisms by Evolutionary Optimization of Morphological Representations of Topology," *Journal of Mechanical Design,* vol. 122, pp. 560-566, 1998.

[73] S. Nishiwaki, M. I. Frecker, S. Min, and N. Kikuchi, "Topology optimization of compliant mechanisms using the homogenization method," *International Journal for Numerical Methods in Engineering,* vol. 42, pp. 535-559, 1998.

[74] G. Z. Lum, T. J. Teo, S. H. Yeo, G. Yang, and M. Sitti, "Structural optimization for flexure-based parallel mechanisms – Towards achieving optimal dynamic and stiffness properties," *Precision Engineering,* vol. 42, pp. 195-207, 2015.

[75] G. Z. Lum, T. J. Teo, G. Yang, S. H. Yeo, and M. Sitti, "Integrating mechanism synthesis and topological optimization technique for stiffness-oriented design of a three degrees-of-freedom flexure-based parallel mechanism," *Precision Engineering,* vol. 39, pp. 125-133, 2014.

[76] S. R. Deepak, M. Dinesh, D. K. Sahu, and G. K. Ananthasuresh, "A Comparative Study of the Formulations and Benchmark Problems for the Topology Optimization of Compliant Mechanisms," *Journal of Mechanisms and Robotics,* vol. 1, p. 011003, 2008.

[77] B. P. Trease, Y.-M. Moon, and S. Kota, "Design of Large-Displacement Compliant Joints," *Journal of Mechanical Design,* vol. 127, pp. 788-798, 2004.

[78] P. Wang, X. Tan, M. L. S. Nai, S. B. Tor, and J. Wei, "Spatial and geometrical-based characterization of microstructure and microhardness for an electron beam melted Ti–6Al–4V component," *Materials & Design,* vol. 95, pp. 287-295, 2016.

[79] E. Merriam, J. Jones, S. Magleby, and L. Howell, "Monolithic 2 DOF fully compliant space pointing mechanism," *Mechanical Sciences,* vol. 4, pp. 384-390, 2013.

[80] E. G. Merriam, J. E. Jones, and L. L. Howell, "Design of 3D-Printed Titanium Compliant Mechanisms," in *Proceedings of the 42nd Aerospace Mechanisms Symposium*, 2014, pp. 169-173.

[81] E. G. Merriam, K. A. Tolman, and L. L. Howell, "Integration of advanced stiffness-reduction techniques demonstrated in a 3D-printable joint," *Mechanism and Machine Theory,* vol. 105, pp. 260-271, 2016.

[82] X. Pei and J. Yu, "ADLIF: a new large-displacement beam-based flexure joint," *Mechanical Sciences,* vol. 2, pp. 183-188, 2011.

[83] T. J. Teo, G. Yang, and I. M. Chen, "A large deflection and high payload flexure-based parallel manipulator for UV nanoimprint lithography: Part I. Modeling and analyses," *Precision Engineering,* vol. 38, pp. 861-871, 2014.

[84] J. B. Hopkins and M. L. Culpepper, "Synthesis of multi-degree of freedom, parallel flexure system concepts via Freedom and Constraint Topology (FACT) – Part I: Principles," *Precision Engineering,* vol. 34, pp. 259-270, 2010.

[85] J. B. Hopkins and M. L. Culpepper, "Synthesis of multi-degree of freedom, parallel flexure system concepts via freedom and constraint topology (FACT). Part II: Practice," *Precision Engineering,* vol. 34, pp. 271-278, 2010.

[86] J. B. Hopkins and M. L. Culpepper, "Synthesis of precision serial flexure systems using freedom and constraint topologies (FACT)," *Precision Engineering,* vol. 35, pp. 638-649, 2011.

[87] M. P. Bendsøe and N. Kikuchi, "Generating optimal topologies in structural design using a homogenization method," *Computer Methods in Applied Mechanics and Engineering,* vol. 71, pp. 197-224, 1988.

[88] M. I. Frecker, G. K. Ananthasuresh, S. Nishiwaki, N. Kikuchi, and S. Kota, "Topological Synthesis of Compliant Mechanisms Using Multi-Criteria Optimization," *Journal of Mechanical Design,* vol. 119, pp. 238-245, 1997.

[89] M. P. Bendsoe and O. Sigmund, *Topology Optimization: Theory, Methods, and Applications*: Springer Science & Business Media, 2003.

[90] O. Sigmund, "A 99 line topology optimization code written in Matlab," *Structural and Multidisciplinary Optimization,* vol. 21, pp. 120-127, 2001.

[91] E. Andreassen, A. Clausen, M. Schevenels, B. Lazarov, and O. Sigmund, "Efficient topology optimization in MATLAB using 88 lines of code," *Structural and Multidisciplinary Optimization,* vol. 43, pp. 1-16, 2011.

[92] G. I. N. Rozvany, "Aims, scope, methods, history and unified terminology of computer-aided topology optimization in structural mechanics," *Structural and Multidisciplinary Optimization,* vol. 21, pp. 90-108, 2001.

[93] T. E. Bruns, "A reevaluation of the SIMP method with filtering and an alternative formulation for solid–void topology optimization," *Structural and Multidisciplinary Optimization,* vol. 30, pp. 428-436, 2005.

[94] O. Sigmund, "On the design of compliant mechanisms using topology optimization*," *Journal of Structural Mechanics,* vol. 25, pp. 493-524, 1997.

[95] O. Sigmund, "Design of Material Structures using Topology Optimization," *Diss. Technical University of Denmark,* 1994.

[96] M. Bruggi and P. Duysinx, "Topology optimization for minimum weight with compliance and stress constraints," *Structural and Multidisciplinary Optimization,* vol. 46, pp. 369-384, 2012.

[97] C. B. Pedersen, T. Buhl, and O. Sigmund, "Topology synthesis of large-displacement compliant mechanisms," *International Journal for numerical methods in engineering,* vol. 50, pp. 2683-2705, 2001.

[98] G. K. Lau, H. Du, and M. K. Lim, "Use of functional specifications as objective functions in topological optimization of compliant mechanism," *Computer Methods in Applied Mechanics and Engineering,* vol. 190, pp. 4421-4433, 2001.

[99] M. Jin and X. Zhang, "A new topology optimization method for planar compliant parallel mechanisms," *Mechanism and Machine Theory,* vol. 95, pp. 42-58, 2016.

[100] Y. M. Xie and G. P. Steven, "A simple evolutionary procedure for structural optimization," *Computers & Structures,* vol. 49, pp. 885-896, 1993.

[101] O. M. Querin, G. P. Steven, and Y. M. Xie, "Evolutionary structural optimisation (ESO) using a bidirectional algorithm," *Engineering Computations,* vol. 15, pp. 1031-1048, 1998.

[102] M. Zhou, B. S. Lazarov, F. Wang, and O. Sigmund, "Minimum length scale in topology optimization by geometric constraints," *Computer Methods in Applied Mechanics and Engineering,* vol. 293, pp. 266-282, 2015.

[103] Y. Wang, Z. Luo, J. Wu, and N. Zhang, "Topology optimization of compliant mechanisms using element-free Galerkin method," *Advances in Engineering Software,* vol. 85, pp. 61-72, 2015.

[104] R. Ansola, E. Veguería, A. Maturana, and J. Canales, "3D compliant mechanisms synthesis by a finite element addition procedure," *Finite Elements in Analysis and Design,* vol. 46, pp. 760-769, 2010.

[105] S. Osher and J. A. Sethian, "Fronts propagating with curvature-dependent speed: Algorithms based on Hamilton-Jacobi formulations," *Journal of Computational Physics,* vol. 79, pp. 12-49, 1988.

[106] M. Y. Wang, X. Wang, and D. Guo, "A level set method for structural topology optimization," *Computer Methods in Applied Mechanics and Engineering,* vol. 192, pp. 227-246, 2003.

[107] T. Yamada, K. Izui, S. Nishiwaki, and A. Takezawa, "A topology optimization method based on the level set method incorporating a fictitious interface energy," *Computer Methods in Applied Mechanics and Engineering,* vol. 199, pp. 2876-2891, 2010.

[108] J. A. Sethian and A. Wiegmann, "Structural Boundary Design via Level Set and Immersed Interface Methods," *Journal of Computational Physics,* vol. 163, pp. 489-528, 2000.

[109] N. P. van Dijk, K. Maute, M. Langelaar, and F. van Keulen, "Level-set methods for structural topology optimization: a review," *Structural and Multidisciplinary Optimization,* vol. 48, pp. 437-472, 2013.

[110] M. Y. Wang and S. Chen, "Compliant Mechanism Optimization: Analysis and Design with Intrinsic Characteristic Stiffness," *Mechanics Based Design of Structures and Machines,* vol. 37, pp. 183-200, 2009.

[111] M. Y. Wang, "A Kinetoelastic Formulation of Compliant Mechanism Optimization," *Journal of Mechanisms and Robotics,* vol. 1, p. 021011, 2009.

[112] M. Frecker, N. Kikuchi, and S. Kota, "Topology optimization of compliant mechanisms with multiple outputs," *Structural optimization,* vol. 17, pp. 269-278, 1999.

[113] N. D. Mankame and G. K. Ananthasuresh, "Synthesis of contact-aided compliant mechanisms for non-smooth path generation," *International Journal for Numerical Methods in Engineering,* vol. 69, pp. 2564-2605, 2007.

[114] A. Saxena, "Synthesis of compliant mechanisms for path generation using genetic algorithm," *Journal of Mechanical Design,* vol. 127, pp. 745-752, 2005.

[115] N. D. Mankame and G. K. Ananthasuresh, "Topology optimization for synthesis of contact-aided compliant mechanisms using regularized contact modeling," *Computers & Structures,* vol. 82, pp. 1267-1290, 2004.

[116] A. Saxena and G. Ananthasuresh, "Topology synthesis of compliant mechanisms for nonlinear force-deflection and curved path specifications," *Journal of Mechanical Design,* vol. 123, pp. 33-42, 2001.

[117] S. Canfield and M. Frecker, "Topology optimization of compliant mechanical amplifiers for piezoelectric actuators," *Structural and Multidisciplinary Optimization,* vol. 20, pp. 269-279, 2000.

[118] N. F. Wang and K. Tai, "Design of Grip-and-Move Manipulators Using Symmetric Path Generating Compliant Mechanisms," *Journal of Mechanical Design,* vol. 130, p. 112305, 2008.

[119] N. F. Wang and K. Tai, "Target matching problems and an adaptive constraint strategy for multiobjective design optimization using genetic algorithms," *Computers & Structures,* vol. 88, pp. 1064-1076, 2010.

[120] L. Guo Zhan, T. Tat Joo, Y. Guilin, Y. Song Huat, and M. Sitti, "A hybrid topological and structural optimization method to design a 3-DOF planar motion compliant mechanism," in *IEEE/ASME International Conference on Advanced Intelligent Mechatronics (AIM)*, 2013, pp. 247-254.

[121] G. Z. Lum, M. T. Pham, T. J. Teo, G. Yang, S. H. Yeo, and M. Sitti, "An XY&thetaZ flexure mechanism with optimal stiffness properties," in *2017 IEEE International Conference on Advanced Intelligent Mechatronics (AIM)*, 2017, pp. 1103-1110.

[122] J. A. Hetrick and S. Kota, "An Energy Formulation for Parametric Size and Shape Optimization of Compliant Mechanisms," *Journal of Mechanical Design,* vol. 121, pp. 229-234, 1999.

[123] Y. Byung-Ju, C. Goo Bong, N. Heung Yeol, K. Whee Kuk, and S. Il Hong, "Design and experiment of a 3-DOF parallel micromechanism utilizing flexure hinges," *IEEE Transactions on Robotics and Automation,* vol. 19, pp. 604-612, 2003.

[124] H.-H. Pham, I.-M. Chen, and H.-C. Yeh, "Micro-motion selective-actuation XYZ flexure parallel mechanism: design and modeling," *Journal of Micromechatronics,* vol. 3, pp. 51-73, 2003.

[125] H.-H. Pham and I. M. Chen, "Stiffness modeling of flexure parallel mechanism," *Precision Engineering,* vol. 29, pp. 467-478, 2005.

[126] R. Wang and X. Zhang, "A planar 3-DOF nanopositioning platform with large magnification," *Precision Engineering,* vol. 46, pp. 221-231, 2016.

[127] B. R. d. Jong, D. M. Brouwer, M. J. d. Boer, H. V. Jansen, H. M. J. R. Soemers, and G. J. M. Krijnen, "Design and Fabrication of a Planar Three-DOFs MEMS-Based Manipulator," *Journal of Microelectromechanical Systems,* vol. 19, pp. 1116-1130, 2010.

[128] D. Mukhopadhyay, J. Dong, E. Pengwang, and P. Ferreira, "A SOI-MEMS-based 3-DOF planar parallel-kinematics nanopositioning stage," *Sensors and Actuators A: Physical,* vol. 147, pp. 340-351, 2008.

[129] T. J. Teo, I. M. Chen, and G. Yang, "A large deflection and high payload flexure-based parallel manipulator for UV nanoimprint lithography: Part II. Stiffness modeling and performance evaluation," *Precision Engineering,* vol. 38, pp. 872-884, 2014.

[130] K. M. Lee and S. Arjunan, "A three-degrees-of-freedom micromotion in-parallel actuated manipulator," *IEEE Transactions on Robotics and Automation,* vol. 7, pp. 634-641, 1991.

[131] T. Tanikawa, T. Arai, and N. Koyachi, "Development of small-sized 3 DOF finger module in micro hand for micro manipulation," in *IEEE/RSJ International Conference on Intelligent Robots and Systems*, 1999, pp. 876-881 vol.2.

[132] Y. Koseki, T. Tanikawa, N. Koyachi, and T. Arai, "Kinematic analysis of a translational 3-d.o.f. micro-parallel mechanism using the matrix method," *Advanced Robotics,* vol. 16, pp. 251-264, 2002.

[133] T. Tanikawa, M. Ukiana, K. Morita, Y. Koseki, K. Ohba, K. Fujii*, et al.*, "Design of 3-DOF parallel mechanism with thin plate for micro finger module in micro manipulation," in *IEEE/RSJ International Conference on Intelligent Robots and Systems*, 2002, pp. 1778-1783 vol.2.

[134] G. Hao, "Design and analysis of symmetric and compact 2R1T (in-plane 3-DOC) flexure parallel mechanisms," *Mechanical Sciences,* vol. 8, pp. 1-9, 2017.

[135] M. L. Culpepper and G. Anderson, "Design of a low-cost nano-manipulator which utilizes a monolithic, spatial compliant mechanism," *Precision Engineering,* vol. 28, pp. 469-482, 2004.

[136] S.-C. Chen and M. L. Culpepper, "Design of a six-axis micro-scale nanopositioner—µHexFlex," *Precision Engineering,* vol. 30, pp. 314-324, 2006.

[137] S. Akbari and T. Pirbodaghi, "Precision positioning using a novel six axes compliant nano-manipulator," *Microsystem Technologies,* vol. 23, pp. 1-9, 2016.

[138] H. S. Fiaz, C. R. Settle, and K. Hoshino, "Metal additive manufacturing for microelectromechanical systems: Titanium alloy (Ti-6Al-4V)-based nanopositioning flexure fabricated by electron beam melting," *Sensors and Actuators A: Physical,* vol. 249, pp. 284-293, 2016.

[139] E. G. Merriam and L. L. Howell, "Lattice flexures: Geometries for stiffness reduction of blade flexures," *Precision Engineering,* vol. 45, pp. 160-167, 2016.

[140] C. Beyer and D. Figueroa, "Design and Analysis of Lattice Structures for Additive Manufacturing," *Journal of Manufacturing Science and Engineering,* p. 121014, 2016.

[141] E. Hernández-Nava, C. J. Smith, F. Derguti, S. Tammas-Williams, F. Leonard, P. J. Withers*, et al.*, "The effect of defects on the mechanical response of Ti-6Al-4V cubic lattice structures fabricated by electron beam melting," *Acta Materialia,* vol. 108, pp. 279-292, 2016.

[142] N. Lobontiu, *Compliant mechanisms: design of flexure hinges*: CRC press, 2010.

[143] T. J. Teo, I. M. Chen, G. Yang, and W. Lin, "A generic approximation model for analyzing large nonlinear deflection of beam-based flexure joints," *Precision Engineering,* vol. 34, pp. 607-618, 2010.

[144] I. Gibson, D. W. Rosen, and B. Stucker, *Additive manufacturing technologies*: Springer, 2010.

APPENDICES

Appendix A   The Equivalent PRB Model for Over-Constrained CPMs

The compliance along the Z axis which exhibits the nonlinear characteristics as shown in Figure 3.10 and Figure 4.5 is caused by the large deformation of the over-constrained three-limb CPM. In this case, each limb can be considered as a fixed-clamped beam as illustrated in Figure A.1. The equivalent fixed-clamped beam can be represented by some key parameters as follows

- The equivalent length, l, is the distance from the fixed end to the loading point.

- The equivalent axial force per unit strain, EA, and bending flexural rigidity, EI, are derived respectively based on the first and the third components along the diagonal of the stiffness matrix of the compliant limb.
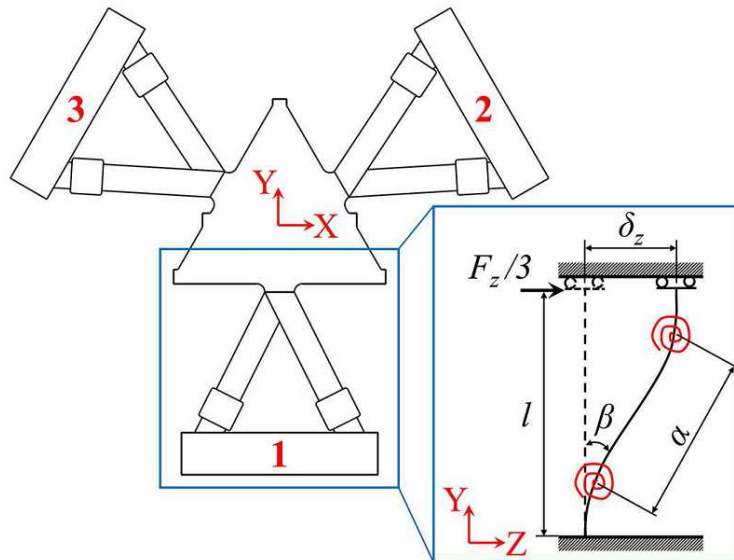
Figure A.1: Equivalent PRB model of a compliant limb.

The PRB model for large deformation of the linear spring is used to analyze the nonlinear stiffness characteristics of the over-constrained CPM. The S-shape of the deformed

equivalent beam can be modeled by two torsion springs at both ends connected by a linear spring as illustrated in Figure A.1. Then, the force (F_z) – displacement (δ_z) relationship along the Z axis can be expressed as [11]

$$F_z = 3\left[K_A \Delta l \sin\beta + 4K_T \frac{\beta}{\gamma l \cos\beta} \right],$$

where

$$\Delta l = \frac{\gamma l}{\cos\beta} - \gamma l,$$

$$K_T = \frac{\gamma}{l} K_\theta (EI),$$

$$K_A = \frac{(EA)}{\gamma l + \Delta l},$$

$$\beta = \tan^{-1}\left(\frac{\delta_z}{\gamma l} \right)$$

(A.1)

where α represents the length change in between two torsional springs, i.e., $\gamma l + \Delta l$, and β represents the deflection angle of the deformed beam. K_T represents the stiffness of the torsion spring and K_A represents the stiffness of the linear spring. Based on past literatures, the spring constant, K_θ, is selected as 2 [1] and γ is derived as 2/3 [143].

Appendix B   EBM Printing Process

In this work, the Arcam A2X electron beam system as shown in Figure B.1, which has a build envelope of 200 × 200 × 380 mm3, is used to fabricate all the 3D-printed prototypes. The fabrication material is Ti6Al4V supplied by Arcam AB.

Figure B.1: Arcam A2X system *(Source: www.arcam.com)*.

In EBM technique, materials from the powder hoppers is first spread over a build platform to create a thin layer. The electron beam from its source is focused and positioned by the corresponding coils. This high-energy electron beam is then scanned through the defined cross-section, causing the material in the scanning area to be melted and joined together to form the desired cross-sectional pattern. A new layer is subsequently spread on the printed layer and the scanning process repeats until the desired structure is formed.

To achieve high quality printed parts as well as to protect human from the gamma rays produced by the electron beam, the EBM printing process must be done in a vacuum chamber as illustrated in Figure B.2.
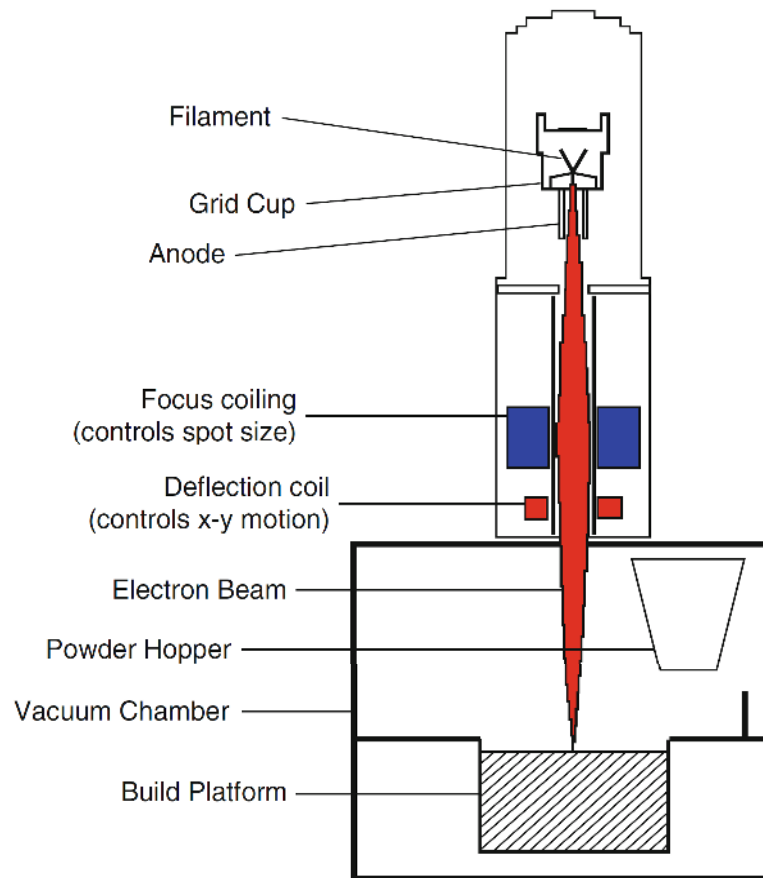
Figure B.2: Concept of the EBM method [144].

The standard build theme from Arcam AB for Ti6Al4V alloy is applied to all building processes in this work. In particular, the accelerating voltage, layer thickness and line offset are set as 60,000 V, 50 μm and 0.1mm respectively. The size of the material powder distributes within a range from 45 μm to 105 μm with the average particle diameter of ~70 μm [78]. A 10 mm-thick start plate made from stainless steel is heated before printing. Once the temperature of the start plate achieves 730 °C, the building process begins. The building process is done under a vacuum of ~2 × 10-3 mBar controlled by using high purity helium as a regulating gas to prevent powder charging. Both the preheating and melting processes are

achieved based on the high-energy of electron beam. For each layer, the melting process is first carried out at the boundary and the area at the center is then melted. This process repeats layer by layer until the part is fully built. The completed prototype can be removed when the temperature reduces to below 100 °C. The semi-sintered powder around the fabricated part is removed and recycled for the next printing job by a powder recovery system.

Appendix C   Effective Thickness of EBM-Printed Flexures Regarding to Different Designed Thickness and Building Directions

As the importance of the effective thickness of EBM-printed flexures has been demonstrated in Chapter 4, it is explored more in terms of different designed thicknesses and building directions. The linear spring mechanism, which is used as testing model, is fabricated by Ti6Al4V material along three main building directions, i.e., along the flexure's length, width and thickness directions, as shown in Figure C.1. For each building direction, a set of prototypes are printed with the designed thickness varies from 0.3 mm to 1 mm, which are the common dimensions popularly used to synthesize compliant mechanisms.
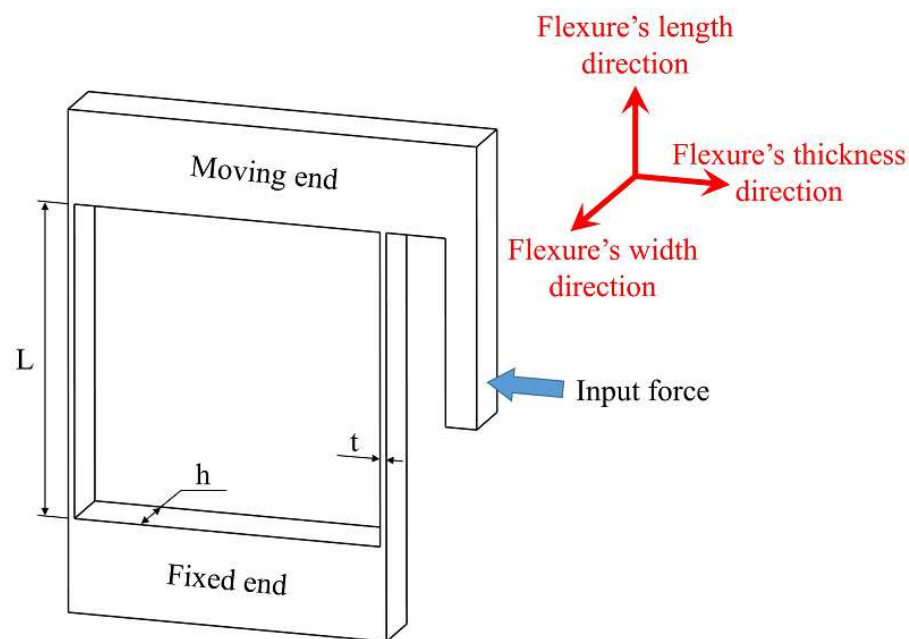
Figure C.1: Model of linear spring mechanism with three main building directions.

The similar experiment as presented in Section 4.2 is used to measure the stiffness of each sample. The corresponding effective thickness and coefficient factor are calculated by Eqs. (4.2) and (4.3) respectively. Based on the experimental results, the plot illustrates the

relation of designed thicknesses and coefficient factors of EBM-printed flexures regarding to the three building directions is shown in Figure C.2.
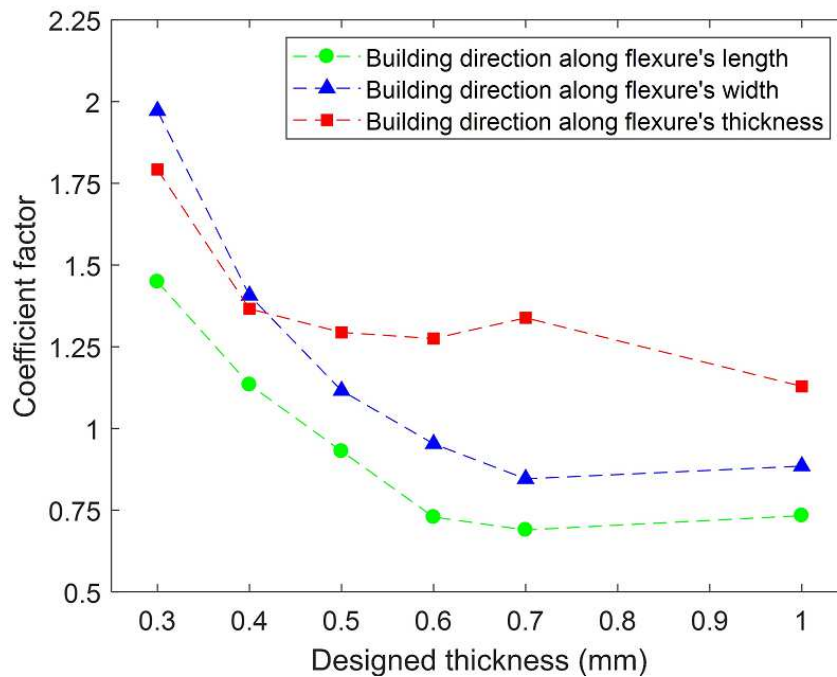
Figure C.2: Coefficient factors of EBM-printed flexures with different design thickness and building directions.

From Figure C.2, the change of coefficient factor with respect to the designed thicknesses and building directions are demonstrated. By using these results, mechanical property of any EBM-printed flexure having thickness of less than 1 mm can be defined by determining the appropriate coefficient factor based on its designed thickness and building direction.

Appendix D   Stiffness Characteristics of Some Popular Flexure Elements

Referring to [125, 142], some popular flexure elements have the same compliance matrix form as expressed in Eq. (5.10) are shown in Figure D.1. They can be revolute hinge, thin beam as illustrated in Figure 5.2, and also can be some other forms such as spherical joint (Figure D.1a) or prismatic joint (linear spring) as shown in Figure D.1b. The notch of spherical joint can have circular or square cross-sectional area while the linear spring can be constructed by four notch hinges or a pair of cantilever beams.
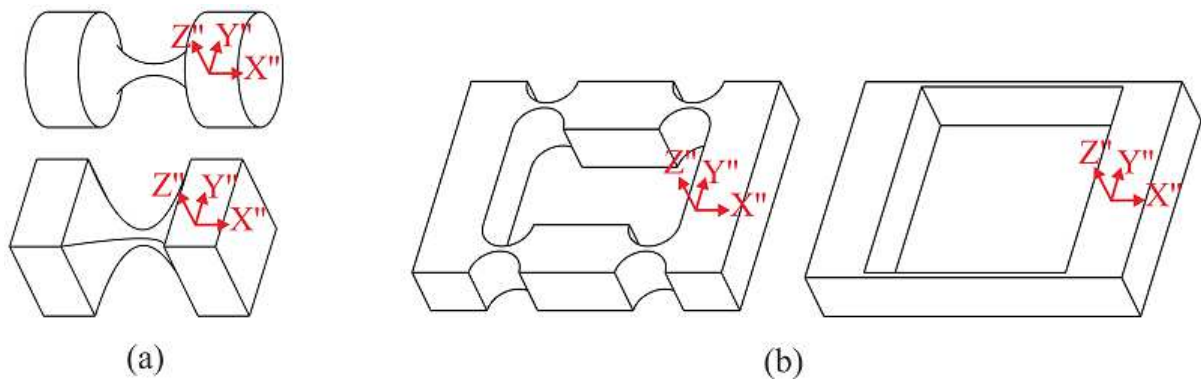
Figure D.1: Flexure elements (a) spherical joint, (b) linear spring.

Appendix E   Conditions of the Compliance Matrix of a Limb for Achieving Decoupled-Motion CPM

Results of the inversion of Eq. (5.8) is written as

$$
\underbrace{\begin{bmatrix}
k_{11}^l & & & & & \\
k_{21}^l & k_{22}^l & & & SYM & \\
0 & 0 & k_{33}^l & & & \\
0 & 0 & k_{43}^l & k_{44}^l & & \\
0 & 0 & k_{53}^l & k_{54}^l & k_{55}^l & \\
k_{61}^l & k_{62}^l & 0 & k_{64}^l & k_{65}^l & k_{66}^l
\end{bmatrix}}_{\left(K^l\right)^{-1}}^{-1}
=
\underbrace{\begin{bmatrix}
c_{11}^l & & & & & \\
c_{21}^l & c_{22}^l & & & SYM & \\
c_{31}^l & c_{32}^l & c_{33}^l & & & \\
c_{41}^l & c_{42}^l & c_{43}^l & c_{44}^l & & \\
c_{51}^l & c_{52}^l & c_{53}^l & c_{54}^l & c_{55}^l & \\
c_{61}^l & c_{62}^l & c_{63}^l & c_{64}^l & c_{65}^l & c_{66}^l
\end{bmatrix}}_{C^l}
\tag{E.1}
$$

The expression of each component in C^l are given as

$$
c_{31}^l = \frac{1}{\Delta}\left(k_{22}^l k_{61}^l - k_{21}^l k_{62}^l\right)\left[k_{64}^l\left(k_{53}^l k_{54}^l - k_{43}^l k_{55}^l\right) + k_{65}^l\left(-k_{44}^l k_{53}^l + k_{43}^l k_{54}^l\right)\right]
\tag{E.2}
$$

$$
c_{41}^l = -\frac{1}{\Delta}\left(k_{22}^l k_{61}^l - k_{21}^l k_{62}^l\right)\left[k_{64}^l\left(\left(k_{53}^l\right)^2 - k_{33}^l k_{55}^l\right) + k_{65}^l\left(-k_{43}^l k_{53}^l + k_{33}^l k_{54}^l\right)\right]
\tag{E.3}
$$

$$
c_{51}^l = -\frac{1}{\Delta}\left(k_{22}^l k_{61}^l - k_{21}^l k_{62}^l\right)\left[k_{64}^l\left(-k_{43}^l k_{53}^l + k_{33}^l k_{54}^l\right) + k_{65}^l\left(\left(k_{43}^l\right)^2 - k_{33}^l k_{44}^l\right)\right]
\tag{E.4}
$$

$$
c_{32}^l = -\frac{1}{\Delta}\left(k_{21}^l k_{61}^l - k_{11}^l k_{62}^l\right)\left[k_{64}^l\left(k_{53}^l k_{54}^l - k_{43}^l k_{55}^l\right) + k_{65}^l\left(-k_{44}^l k_{53}^l + k_{43}^l k_{54}^l\right)\right]
\tag{E.5}
$$

$$
c_{42}^l = \frac{1}{\Delta}\left(k_{21}^l k_{61}^l - k_{11}^l k_{62}^l\right)\left[k_{64}^l\left(\left(k_{53}^l\right)^2 - k_{33}^l k_{55}^l\right) + k_{65}^l\left(-k_{43}^l k_{53}^l + k_{33}^l k_{54}^l\right)\right]
\tag{E.6}
$$

$$
c_{52}^l = \frac{1}{\Delta}\left(k_{21}^l k_{61}^l - k_{11}^l k_{62}^l\right)\left[k_{64}^l\left(-k_{43}^l k_{53}^l + k_{33}^l k_{54}^l\right) + k_{65}^l\left(\left(k_{43}^l\right)^2 - k_{33}^l k_{44}^l\right)\right]
\tag{E.7}
$$

$$c_{63}^l = \frac{1}{\Delta}\left(\left(k_{21}^l\right)^2 - k_{11}^l k_{22}^l\right)\left[k_{64}^l\left(k_{53}^l k_{54}^l - k_{43}^l k_{55}^l\right) + k_{65}^l\left(-k_{44}^l k_{53}^l + k_{43}^l k_{54}^l\right)\right] \tag{E.8}$$

$$c_{64}^l = -\frac{1}{\Delta}\left(\left(k_{21}^l\right)^2 - k_{11}^l k_{22}^l\right)\left[k_{64}^l\left(\left(k_{53}^l\right)^2 - k_{33}^l k_{55}^l\right) + k_{65}^l\left(-k_{43}^l k_{53}^l + k_{33}^l k_{54}^l\right)\right] \tag{E.9}$$

$$c_{65}^l = -\frac{1}{\Delta}\left(\left(k_{21}^l\right)^2 - k_{11}^l k_{22}^l\right)\left[k_{64}^l\left(-k_{43}^l k_{53}^l + k_{33}^l k_{54}^l\right) + k_{65}^l\left(\left(k_{43}^l\right)^2 - k_{33}^l k_{44}^l\right)\right] \tag{E.10}$$

$$
\begin{aligned}
c_{21}^l = \frac{1}{\Delta}\Bigg\{ &-k_{21}^l\left(k_{53}^l\right)^2\left(k_{64}^l\right)^2 + 2k_{43}^l k_{53}^l\left(k_{54}^l k_{61}^l k_{62}^l + k_{21}^l k_{64}^l k_{65}^l - k_{21}^l k_{54}^l k_{66}^l\right) - \\
&\left(k_{43}^l\right)^2\left(k_{55}^l k_{61}^l k_{62}^l + k_{21}^l\left(k_{65}^l\right)^2 - k_{21}^l k_{55}^l k_{66}^l\right) + \\
&k_{33}^l\left[k_{21}^l k_{55}^l\left(k_{64}^l\right)^2 + k_{54}^l\left(-k_{54}^l k_{61}^l k_{62}^l - k_{21}^l k_{64}^l k_{65}^l + k_{21}^l k_{54}^l k_{66}^l\right)\right] + \\
&k_{44}^l\left[\left(k_{53}^l\right)^2\left(-k_{61}^l k_{62}^l + k_{21}^l k_{66}^l\right) + k_{33}^l\left(k_{55}^l k_{61}^l k_{62}^l + k_{21}^l\left(k_{65}^l\right)^2 - k_{21}^l k_{55}^l k_{66}^l\right)\right]\Bigg\}
\end{aligned} \tag{E.11}
$$

$$c_{61}^l = \frac{1}{\Delta}\left\{\left[-2k_{43}^l k_{53}^l k_{54}^l + k_{33}^l\left(k_{54}^l\right)^2 + \left(k_{43}^l\right)^2 k_{55}^l + k_{44}^l\left(\left(k_{53}^l\right)^2 - k_{33}^l k_{55}^l\right)\right]\left(k_{22}^l k_{61}^l - k_{21}^l k_{62}^l\right)\right\} \tag{E.12}$$

$$c_{62}^l = -\frac{1}{\Delta}\left\{\left[-2k_{43}^l k_{53}^l k_{54}^l + k_{33}^l\left(k_{54}^l\right)^2 + \left(k_{43}^l\right)^2 k_{55}^l + k_{44}^l\left(\left(k_{53}^l\right)^2 - k_{33}^l k_{55}^l\right)\right]\left(k_{21}^l k_{61}^l - k_{11}^l k_{62}^l\right)\right\} \tag{E.13}$$

$$
\begin{aligned}
c_{43}^l = \frac{1}{\Delta}\Bigg\{ &2k_{21}^l\left(k_{53}^l k_{54}^l - k_{43}^l k_{55}^l\right)k_{61}^l k_{62}^l + k_{11}^l\left(-k_{53}^l k_{54}^l - k_{43}^l k_{55}^l\right)\left(k_{62}^l\right)^2 + \\
&\left(k_{21}^l\right)^2\left(k_{53}^l k_{64}^l k_{65}^l - k_{43}^l\left(k_{65}^l\right)^2 - k_{53}^l k_{54}^l k_{66}^l + k_{43}^l k_{55}^l k_{66}^l\right) + \\
&k_{22}^l\left[-k_{53}^l\left(k_{54}^l\left(k_{61}^l\right)^2 + k_{11}^l k_{64}^l k_{65}^l - k_{11}^l k_{54}^l k_{66}^l\right) + \\
&k_{43}^l\left(k_{55}^l\left(k_{61}^l\right)^2 + k_{11}^l\left(k_{65}^l\right)^2 - k_{11}^l k_{55}^l k_{66}^l\right)\right]\Bigg\}
\end{aligned} \tag{E.14}
$$

155

$$c_{53}^l = \frac{1}{\Delta}\left\{ 2k_{21}^l\left(k_{43}^l k_{53}^l - k_{33}^l k_{54}^l\right)k_{61}^l k_{62}^l + k_{11}^l\left(-k_{43}^l k_{53}^l + k_{33}^l k_{54}^l\right)\left(k_{62}^l\right)^2 - \right.$$
$$\left(k_{21}^l\right)^2\left(k_{33}^l k_{64}^l k_{65}^l + k_{43}^l k_{53}^l k_{66}^l - k_{33}^l k_{54}^l k_{66}^l\right) +$$
$$\left. k_{22}^l\left[k_{43}^l k_{53}^l\left(-\left(k_{61}^l\right)^2 + k_{11}^l k_{66}^l\right) + k_{33}^l\left(k_{54}^l\left(k_{61}^l\right)^2 + k_{11}^l k_{64}^l k_{65}^l - k_{11}^l k_{54}^l k_{66}^l\right)\right]\right\} \tag{E.15}$$

where

$$\Delta = -2k_{21}^l\left\{-2k_{43}^l k_{53}^l k_{54}^l + k_{33}^l\left(k_{54}^l\right)^2 + \left(k_{43}^l\right)^2 k_{55}^l + k_{44}^l\left[\left(k_{53}^l\right)^2 - k_{33}^l k_{55}^l\right]\right\}k_{61}^l k_{62}^l +$$
$$k_{11}^l\left\{-2k_{43}^l k_{53}^l k_{54}^l + k_{33}^l\left(k_{54}^l\right)^2 + \left(k_{43}^l\right)^2 k_{55}^l + k_{44}^l\left[\left(k_{53}^l\right)^2 - k_{33}^l k_{55}^l\right]\right\}\left(k_{62}^l\right)^2 +$$
$$\left(k_{21}^l\right)^2\left\{\left(k_{53}^l\right)^2\left[-\left(k_{64}^l\right)^2 + k_{44}^l k_{66}^l\right] + 2k_{43}^l k_{53}^l\left(k_{64}^l k_{65}^l - k_{54}^l k_{66}^l\right) + \left(k_{43}^l\right)^2\left[-\left(k_{65}^l\right)^2 + k_{55}^l k_{66}^l\right] +\right.$$
$$\left. k_{33}^l\left[k_{55}^l\left(k_{64}^l\right)^2 - 2k_{54}^l k_{64}^l k_{65}^l + k_{44}^l\left(k_{65}^l\right)^2 + \left(k_{54}^l\right)^2 k_{66}^l - k_{44}^l k_{55}^l k_{66}^l\right]\right\} +$$
$$k_{22}^l\left\{ k_{11}^l\left(k_{53}^l\right)^2\left(k_{64}^l\right)^2 - 2k_{43}^l k_{53}^l\left[k_{54}^l\left(k_{61}^l\right)^2 + k_{11}^l k_{64}^l k_{65}^l - k_{11}^l k_{54}^l k_{66}^l\right] + \right. \tag{E.16}$$
$$\left(k_{43}^l\right)^2\left[k_{55}^l\left(k_{61}^l\right)^2 + k_{11}^l\left(k_{65}^l\right)^2 - k_{11}^l k_{55}^l k_{66}^l\right] +$$
$$k_{33}^l\left[-k_{11}^l k_{55}^l\left(k_{64}^l\right)^2 + k_{54}^l\left(k_{54}^l\left(k_{61}^l\right)^2 + 2k_{11}^l k_{64}^l k_{65}^l - k_{11}^l k_{54}^l k_{66}^l\right)\right] +$$
$$\left. k_{44}^l\left[\left(k_{53}^l\right)^2\left(\left(k_{61}^l\right)^2 - k_{11}^l k_{66}^l\right) - k_{33}^l\left(k_{55}^l\left(k_{61}^l\right)^2 + k_{11}^l\left(k_{65}^l\right)^2 - k_{11}^l k_{55}^l k_{66}^l\right)\right]\right\}$$

The form of C^l needs to be specified as a standard for the design process of decoupled-motion CPMs. It is seen that the expressions of seven compliance components corresponding to the seven zero-components in the stiffness matrix have similar forms. Here, these seven compliance components are required to be zeros so that the form of the limb's compliance matrix will be the same with its stiffness matrix. This special form offers the simplicity during the design process and can be used as the standard to define the decoupled-motion capability of CPMs. The requirements to make the seven compliance components equal to zeros are written as follows

$$\begin{cases} k_{22}^l k_{61}^l - k_{21}^l k_{62}^l = 0 \\ k_{21}^l k_{61}^l - k_{11}^l k_{62}^l = 0 \\ \left(k_{21}^l\right)^2 - k_{11}^l k_{22}^l = 0 \end{cases} \quad \text{or} \quad \begin{cases} k_{64}^l \left(k_{53}^l k_{54}^l - k_{43}^l k_{55}^l\right) + k_{65}^l \left(-k_{44}^l k_{53}^l + k_{43}^l k_{54}^l\right) = 0 \\ k_{64}^l \left(\left(k_{53}^l\right)^2 - k_{33}^l k_{55}^l\right) + k_{65}^l \left(-k_{43}^l k_{53}^l + k_{33}^l k_{54}^l\right) = 0 \\ k_{64}^l \left(-k_{43}^l k_{53}^l + k_{33}^l k_{44}^l\right) + k_{65}^l \left(\left(k_{43}^l\right)^2 - k_{33}^l k_{44}^l\right) = 0 \end{cases} \tag{E.17}$$

As the diagonal components in the stiffness matrix are always non-zeros while the non-diagonal components can be zeros or non-zeros, the non-diagonal components are considered as unknowns and the diagonal ones are parameters. In the first set of equations, one of the first two equations can be redundant. The answers of the first set of equations are

$$\begin{cases} k_{21}^l = \pm\sqrt{k_{11}^l k_{22}^l} \\ k_{61}^l = \pm\sqrt{\dfrac{k_{11}^l}{k_{22}^l}} k_{62}^l \end{cases} \tag{E.18}$$

The second set of equations contain three equations with five unknowns so that there could be many solutions. Here, two simple solutions are proposed, and their answers are given as

$$\begin{cases} k_{64}^l = 0 \\ k_{65}^l = 0 \end{cases} \quad \text{or} \quad \begin{cases} k_{53}^l k_{54}^l - k_{43}^l k_{55}^l = 0 \\ -k_{44}^l k_{53}^l + k_{43}^l k_{54}^l = 0 \\ \left(k_{53}^l\right)^2 - k_{33}^l k_{55}^l = 0 \\ -k_{43}^l k_{53}^l + k_{33}^l k_{54}^l = 0 \\ \left(k_{43}^l\right)^2 - k_{33}^l k_{44}^l = 0 \end{cases} \tag{E.19}$$

$$\Leftrightarrow \begin{cases} k_{64}^l = 0 \\ k_{65}^l = 0 \end{cases} \quad \text{or} \quad \begin{cases} k_{43}^l = \pm\sqrt{k_{33}^l k_{44}^l} \\ k_{53}^l = \pm\sqrt{k_{33}^l k_{55}^l} \\ k_{54}^l = \pm\sqrt{k_{44}^l k_{55}^l} \end{cases}$$

Appendix F   Inversion of the Compliance Matrix of a Limb in a Decoupled-Motion CPM

$$k_{11}^l = \frac{\left(c_{62}^l\right)^2 - c_{22}^l c_{66}^l}{c_{22}^l \left(c_{61}^l\right)^2 - 2c_{21}^l c_{61}^l c_{62}^l + c_{11}^l \left(c_{62}^l\right)^2 + \left(c_{21}^l\right)^2 c_{66}^l - c_{11}^l c_{22}^l c_{66}^l} \tag{F.1}$$

$$k_{21}^l = \frac{-c_{61}^l c_{62}^l + c_{21}^l c_{66}^l}{-2c_{21}^l c_{61}^l c_{62}^l + c_{11}^l \left(c_{62}^l\right)^2 + \left(c_{21}^l\right)^2 c_{66}^l + c_{22}^l \left[\left(c_{61}^l\right)^2 - c_{11}^l c_{66}^l\right]} \tag{F.2}$$

$$k_{61}^l = \frac{c_{22}^l c_{61}^l - c_{21}^l c_{62}^l}{c_{22}^l \left(c_{61}^l\right)^2 - 2c_{21}^l c_{61}^l c_{62}^l + c_{11}^l \left(c_{62}^l\right)^2 + \left(c_{21}^l\right)^2 c_{66}^l - c_{11}^l c_{22}^l c_{66}^l} \tag{F.3}$$

$$k_{22}^l = \frac{\left(c_{61}^l\right)^2 - c_{11}^l c_{66}^l}{c_{22}^l \left(c_{61}^l\right)^2 - 2c_{21}^l c_{61}^l c_{62}^l + c_{11}^l \left(c_{62}^l\right)^2 + \left(c_{21}^l\right)^2 c_{66}^l - c_{11}^l c_{22}^l c_{66}^l} \tag{F.4}$$

$$k_{62}^l = \frac{-c_{21}^l c_{61}^l + c_{11}^l c_{62}^l}{-2c_{21}^l c_{61}^l c_{62}^l + c_{11}^l \left(c_{62}^l\right)^2 + \left(c_{21}^l\right)^2 c_{66}^l + c_{22}^l \left[\left(c_{61}^l\right)^2 - c_{11}^l c_{66}^l\right]} \tag{F.5}$$

$$k_{33}^l = \frac{\left(c_{54}^l\right)^2 - c_{44}^l c_{55}^l}{c_{44}^l \left(c_{53}^l\right)^2 - 2c_{43}^l c_{53}^l c_{54}^l + c_{33}^l \left(c_{54}^l\right)^2 + \left(c_{43}^l\right)^2 c_{55}^l - c_{33}^l c_{44}^l c_{55}^l} \tag{F.6}$$

$$k_{43}^l = \frac{-c_{53}^l c_{54}^l + c_{43}^l c_{55}^l}{-2c_{43}^l c_{53}^l c_{54}^l + c_{33}^l \left(c_{54}^l\right)^2 + \left(c_{43}^l\right)^2 c_{55}^l + c_{44}^l \left[\left(c_{53}^l\right)^2 - c_{33}^l c_{55}^l\right]} \tag{F.7}$$

$$k_{53}^l = \frac{c_{44}^l c_{53}^l - c_{43}^l c_{54}^l}{c_{44}^l \left(c_{53}^l\right)^2 - 2c_{43}^l c_{53}^l c_{54}^l + c_{33}^l \left(c_{54}^l\right)^2 + \left(c_{43}^l\right)^2 c_{55}^l - c_{33}^l c_{44}^l c_{55}^l} \tag{F.8}$$

$$k_{44}^l = \frac{\left(c_{53}^l\right)^2 - c_{33}^l c_{55}^l}{c_{44}^l \left(c_{53}^l\right)^2 - 2c_{43}^l c_{53}^l c_{54}^l + c_{33}^l \left(c_{54}^l\right)^2 + \left(c_{43}^l\right)^2 c_{55}^l - c_{33}^l c_{44}^l c_{55}^l} \tag{F.9}$$

$$k_{54}^l = \frac{-c_{43}^l c_{53}^l + c_{33}^l c_{54}^l}{-2c_{43}^l c_{53}^l c_{54}^l + c_{33}^l \left(c_{54}^l\right)^2 + \left(c_{43}^l\right)^2 c_{55}^l + c_{44}^l \left[\left(c_{53}^l\right)^2 - c_{33}^l c_{55}^l\right]} \tag{F.10}$$

$$k_{55}^l = \frac{\left(c_{43}^l\right)^2 - c_{33}^l c_{44}^l}{c_{44}^l \left(c_{53}^l\right)^2 - 2c_{43}^l c_{53}^l c_{54}^l + c_{33}^l \left(c_{54}^l\right)^2 + \left(c_{43}^l\right)^2 c_{55}^l - c_{33}^l c_{44}^l c_{55}^l} \tag{F.11}$$

$$k_{66}^l = \frac{\left(c_{21}^l\right)^2 - c_{11}^l c_{22}^l}{c_{22}^l \left(c_{61}^l\right)^2 - 2c_{21}^l c_{61}^l c_{62}^l + c_{11}^l \left(c_{62}^l\right)^2 + \left(c_{21}^l\right)^2 c_{66}^l - c_{11}^l c_{22}^l c_{66}^l} \tag{F.12}$$